Rochester Institute of Technology

RIT Digital Institutional Repository

7-2017

Effect of Aggregation on Squaraine Fullerene Bulk-Heterojunction Organic Photovoltaic Devices

Ishita Jalan
ij2405@rit.edu

R·I·T

Effect of Aggregation on Squaraine Fullerene Bulk-Heterojunction Organic Photovoltaic Devices

By

Ishita Jalan

B.S. Chemistry, University of Manchester, Manchester, UK, 2013

A Thesis submitted in partial fulfillment of the requirements
for the Degree of Master of Science in Chemistry in the
School of Chemistry and Material Science
College of Science
Rochester Institute of Technology
Rochester, New York

July 2017

Signature of the Author: _____

Ishita Jalan

Accepted by: _____

Michael Coleman

Director, M.S. Degree Program

SCHOOL OF CHEMISTRY AND MATERIALS SCIENCE

COLLEGE OF SCIENCE

ROCHESTER INSTITUTE OF TECHNOLOGY

ROCHESTER, NEW YORK

<u>CERTIFICATE OF APPROVAL</u>

M.S. DEGREE THESIS

The M.S. Degree Thesis of Ishita Jalan has

been examined and approved by the thesis

Committee as satisfactory for the thesis required for

the M.S. degree in Chemistry.

_____
Dr. Christopher Collison, *Thesis Advisor*

_____
Dr. Jeremy Cody

_____
Dr. Nathan Eddingsaas

_____
Dr. Jiandi Wan

_____
Date

ACKNOWLEDGMENTS

I would like to thank my advisor Dr. Christopher Collison for his continuous guidance, support and financial assistance throughout my master's study and research. I have grown and learnt a lot under your guidance and you have been very patient with me. Your enthusiasm inspired me and made me fall in love with what I studied at RIT.

I would also like to thank Dr. Jeremy Cody, Dr. Eddingsaas and Dr. Wan for being my committee members and always having an open door for me to discuss my research. Your generosity with the time and effort you provided toward the completion of my master's thesis, is something I greatly appreciate and cherish. Thanks to my research group members: Chenyu Zheng, Patrick Cost, Dan Saviola, Kenny Batiste, Yaxin Zhang and Jean Li for all their encouragement and help during my time at RIT. Lastly, I would like to thank my family and friends for their tremendous support and spiritual guidance. Your endless love, care and encouragement gave me the strength to complete my degree.

ABSTRACT

Organic photovoltaics (OPV) offer great promise as a low-cost renewable energy source, the relative low efficiency still challenges its commercialization potential. Small conjugated molecules like Squaraine (SQ) molecules show promising advancement in organic photovoltaics (OPV). Advantages of SQ over other materials is that it has a high extinction coefficient ($>10^5$), decent photo-stability, good synthetic reproducibility, and tunable molecular structure. With small chemical modifications, the squaraines can have substantial impact on photophysical properties and aggregation pattern, and thus on operational OPV efficiency. The squaraine molecule that will be studied in this work is a symmetric aniline-based squaraine with n-hexyl chain on the molecular arm with di hydroxyl substituents on the aniline, this will be referred to $DHSQ(OH)_2$. In this work, the assignment of the monomer and aggregate peak is discussed. It is known that crystallinity is important for efficient charge transport and exciton diffusion in the BHJ, this thesis focuses on thermal and solvent vapor annealing the as-cast films to reduce the amorphous regions. It is observed that crystallinity is improved but often at the expense of larger crystal size. Therefore, to achieve optimal OPV efficiency, this tradeoff is controlled to improve the crystallinity while maintaining a small, highly mixed BHJ morphology.

LIST OF ABBREVIATIONS

η_{OPV} ……………..Efficiency of the device
η_A ………………..Efficiency of absorption
η_{ED} ………………Efficiency of exciton diffusion
η_{CS} ………………Efficiency of charge separation
η_{CT} ………………Efficiency of charge transfer
η_{CC} ………………Efficiency of charge collection
BHJ……………..Bulk Heterojunction
D-A material……Donor – Acceptor material
DCM……………Dichloromethane
DHSQ(OH)$_2$…….Symmetric aniline-based squaraine with n-hexyl chain on the molecular arm with di hydroxyl substituents on the aniline
FF……………….Fill Factor
FWHM………….Full Width Half Max
HOMO………….Highest occupied molecular orbital
ICT……………...Intermolecular Charge Transfer
IPA………………Isopropyl Alcohol
ITO………………Indium Tin Oxide
J_m………………...The current at the point where the curve is at its maximum power output
J_{SC}……………….Short Circuit Current
J−V curve……….Current-voltage curve
LUMO…………..Lowest unoccupied molecular orbital
NIR………………Near infrared
OPV……………...Organic Photovoltaic
P3HT…………….Poly(3-hexylthiophene-2,5-diyl)
PCBM……………Pheny-C61-butyric acid methyl ester
PCE………………Power Conversion Efficiency
PEDOT:PSS……...Poly(3,4-ethylenedioxythiophene) polystyrene sulfonate
$P_{incident}$…………….Power of the incident light
PMMA……………Poly-(methyl methacrylate)
SQ………………..Squaraine
SVA……………...Solvent Vapor Annealing
TA………………..Thermal Annealing
TEM……………...Transmission Electron Microscopy
V_m………………...The voltage at the point where the curve is at its maximum power output
V_{OC}………………..Open Circuit Voltage
Wt%........................Weight Percent
XRD………………X-ray Diffraction

Table of Contents

List of Figures

List of Tables

Chapter 1 : Introduction

1.1 Organic Photovoltaic

As fossil fuels are only temporary and will someday deplete, scientific research for inexpensive sustainable energy sources, such as solar energy is encouraged. Renewable sources of energy represent about 10% of global energy consumption, out of which about 2% represents solar energy[1]. Solar energy has the potential to become the main source of energy in future as it is reliable, free, clean and infinitely renewable[2].

Organic photovoltaic (OPV) devices are made from polymers and small molecules instead of using silicon[3]. The advantages of these devices are that they are cheap, easy to make, can be processed on flexible substrates and are very tunable. However, this technology is fairly new and not yet commercialized as the commercial value of the OPV cell depends on its efficiency, which is low. To be able to improve the efficiencies of these OPV devices, it is important to understand how they work.

1.1.1 Architecture of an organic photovoltaic device

The general structure used for organic solar cells is based on a sandwich structure (Figure 1.1a)[4]. The substrate used is glass, which is covered with a conducting electrode (anode), which in this case is indium tin oxide (ITO). On the glass layer, a buffer layer is spin coated, in this case PEDOT:PSS. The buffer layer improves the surface of the ITO layer and helps with hole extraction as it will not transport the electrons due to its energy levels (Figure 1.1b)[5]. The active site is made up of a mixture of an electron acceptor material and an electron donor material, coated using a spin cast technique. Then, the top metal cathode having a lower work-

function metal (as compared to ITO), such as aluminum, is evaporated onto the substrate[6].
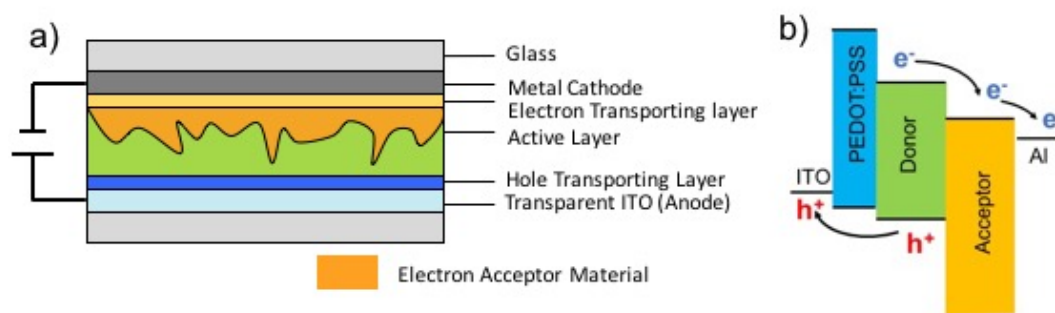
Figure 1.1: a) General structure of the organic solar cell, b) A schematic illustration of an organic solar cell energy levels

A blend of electron donor and acceptor makes up the active layer. Poly (3-hexylthiophene-2,5 diyl) (P3HT)[7, 8] is a polymer that is commonly used as an electron donor material. But these semiconducting polymers are difficult to synthesize and purify[9] compared to small molecules such as squaraines (SQ)[10-14]. The most successful electron acceptor material used is [6,6]-phenyl-C61-butyric acid methyl ester (PC$_{61}$BM or PCBM)[15, 16]. Due to PCBM being strongly electron-deficient, it has the extraordinary ability to be "stabilized" with the uptake of an electron. As it is soluble in most organic solvents, it makes it a very good acceptor material in solution processed OPV[17].

1.1.2 Mechanism of photon to electron conversion in OPV

There are five fundamental steps that can describe the method of converting light into electricity by an OPV: (1) Absorption; (2) exciton diffusion; (3) exciton dissociation; (4) charge separation and (5) charge collection[18, 19].

The Absorption process occurs when an active layer material absorbs a photon from the sun, and forms an excited state. This excited state is an exciton (excited state

electron bound to the hole) (Figure 1.2). This means that an electron from the highest

occupied molecular orbital (HOMO) of the donor gets excited into the lowest

unoccupied molecular orbital (LUMO) of the donor, shown on the right of Figure 1.2.
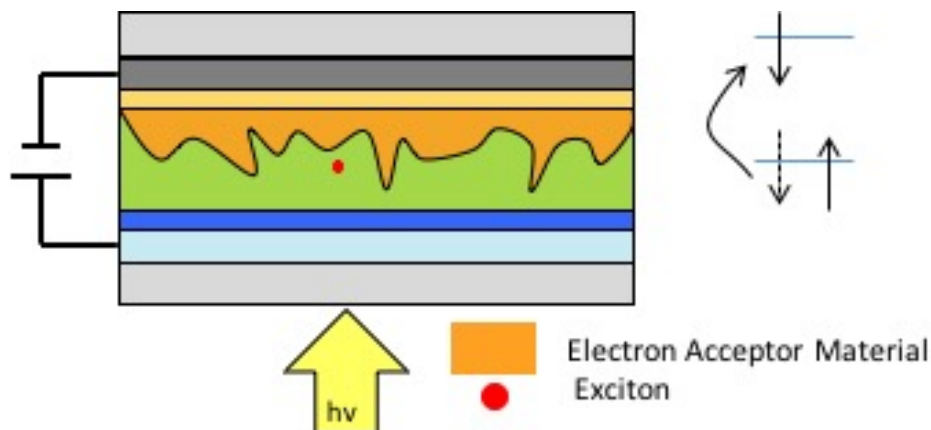
Figure 1.2: Absorption

For the electron-hole separation to occur, the exciton diffuses to the bulk

heterojunction (BHJ) interface between the donor and acceptor (Figure 1.3).
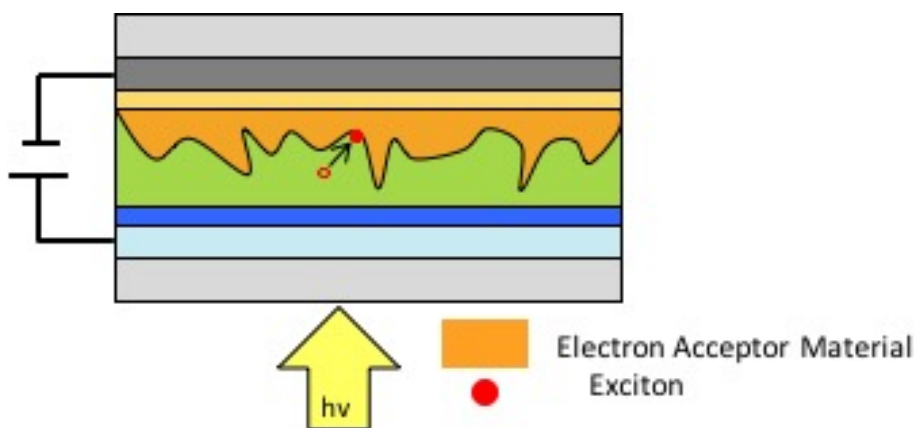
Figure 1.3: Exciton diffusion

Figure 1.4 shows what occurs when the exciton reaches the interface between

the donor/acceptor. At that interface, due to the LUMO energy level of the acceptor

being lower than the LUMO energy of the donor, the electron of the donor molecule

relaxes over to the LUMO of the acceptor molecule.
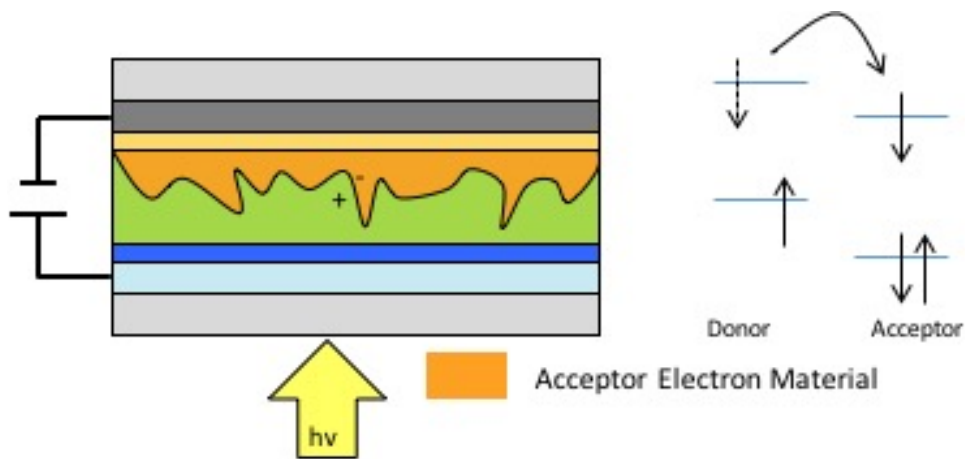
Figure 1.4: Charge separation

Finally, the charges diffuse to the electrodes as result of a concentration gradient and are ultimately collected there (charge collection) (Figure 1.5).
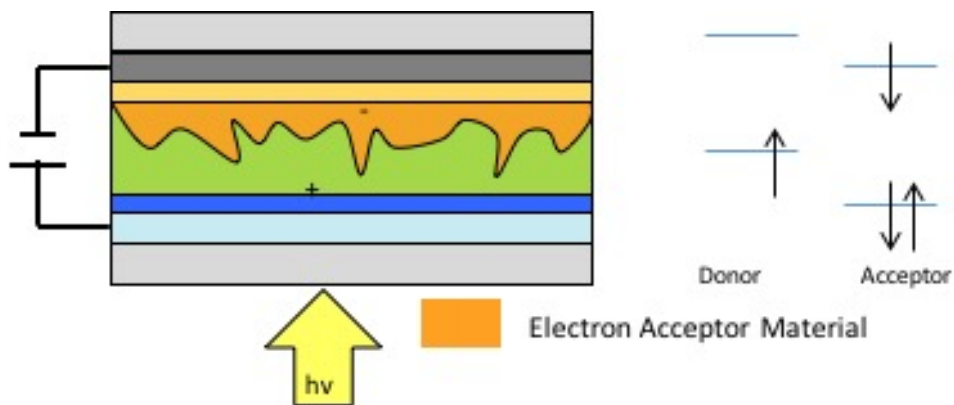
Figure 1.5: Charge Collection

As described above, these processes occur in the active layer. It is very important to be able to control and understand the morphology of the active layer to improve the efficiency of the OPV devices. As the active layer is created by spin coating of a solution containing both the materials in the active layer molecules, it is a heterogeneous blend and can contain a variety of micro and nanostructures, phases and domain size. These depend on the solution components used, the concentration, the spin speed, the environment in which the films were coated and the treatment

4

given to the film after it has been coated, like thermal annealing (TA) or solvent vapor annealing (SVA). All of these factors will contribute to the efficiency of the device.

1.1.3 Efficiency of OPV devices

The efficiencies of these organic photovoltaic devices can be predicted by Equation 1.1[20]:

$$\eta_{OPV} = \eta_A \eta_{ED} \eta_{CS} \eta_{CT} \eta_{CC}$$

Equation 1.1

where η_{OPV} is the efficiency of the device, η_A is the efficiency of absorption, η_{ED} is the efficiency of exciton diffusion, η_{CS} is the efficiency of charge separation, η_{CT} is the efficiency of charge transfer and η_{CC} is the efficiency of charge collection. It can be seen that each efficiency is related to each of the steps of the mechanism as stated above.

The absorption efficiency, η_A, is an intrinsic property of the materials used in the active layer. It is determined by the extinction coefficient and the range of the absorption spectrum. The Beer–Lambert law (Equation 1.2) relates the absorption of light to the extinction coefficient of the material through which the light is traveling. In the Equation 1.2, A is the absorption of light, ε is the extinction coefficient of the material, c is the concentration of the material and l is the path length.

$$A = \varepsilon c l$$

Equation 1.2

Therefore, to optimize the absorption efficiency the material should absorb as much sun light as it can. Hence, the material would need to have a high extinction coefficient as well as a broad absorbance band in the near infrared (NIR) region. As

seen in the spectrum of photon flux of the solar radiation (Figure 1.6[21]), there are more photons in the near IR region of the solar spectrum, and this is why the near-infrared (NIR) absorption is valuable. Photons absorbed ultimately are converted to electrons which leads to a flow of current.
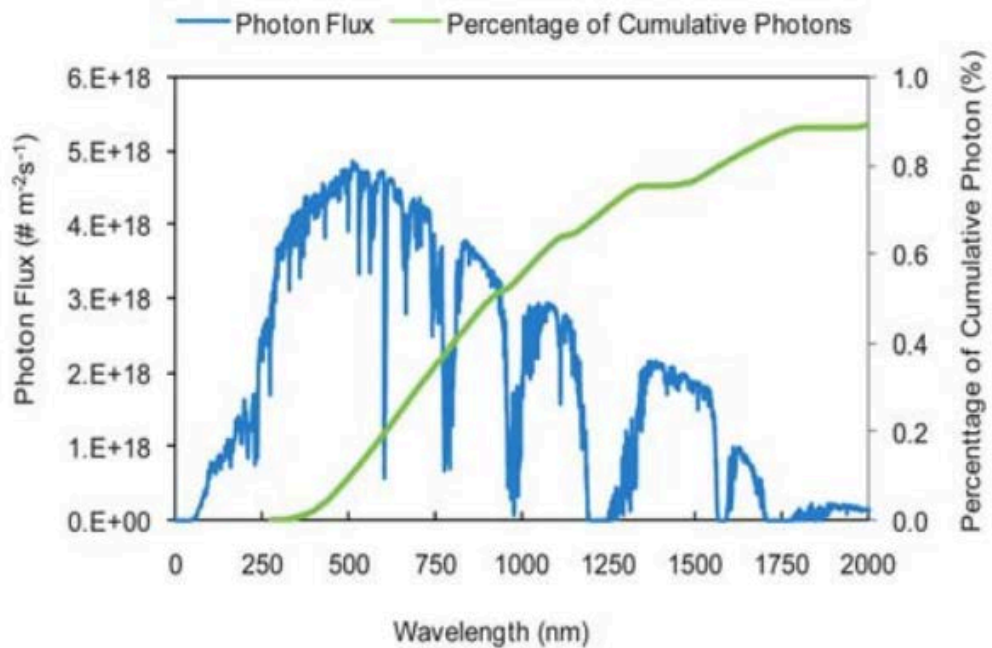
Figure 1.6: Photon flux of the solar radiation as a function of wavelength (blue) and the percentage of the cumulative photons (green)[21]

The exciton diffusion efficiency, η_{ED}, is correlated to the diffusion length and the lifetime of the excited state. It is related to the distance the exciton must travel to reach the interface of the donor and the acceptor during the lifetime of the excited state. As the exciton is a neutral species, it is not affected by the electric field created by the dipole dipole interaction of the materials. The diffusion is random, which is why the morphology of the active layer is important. The material must be interdigitated at the nanoscale to be able to collect all of the excitons that are generated in the active layer. The charge separation efficiency, η_{CS}, is the most important step in the mechanism. This is the conversion of the photon to electron[22].

6

This step is driven by the difference in energy between the LUMO of the donor and the LUMO of the acceptor material. For this process to take place it is beneficial to have a large interface area between the donor and acceptor domains and an optimal LUMO-LUMO energy offset. The charge transfer efficiency, η_{CT}, is related to the efficiency for dissociation of a bound electron and hole pair across the interface. At this step, the bound electron and hole pair dissociate from the charge transfer complex state to form free charges. This means that the electron and hole need to overcome the coulombic binding energy to dissociate into free charges. The charge collection efficiency, η_{CC}, is related to how efficiently the free charges migrate to the electrode. Recombination at the donor/acceptor interface will reduce charge collection efficiency.

A Current-voltage curve is a standard characterization measure for an OPV device. A sample J-V curve is provided in Figure 1.7.
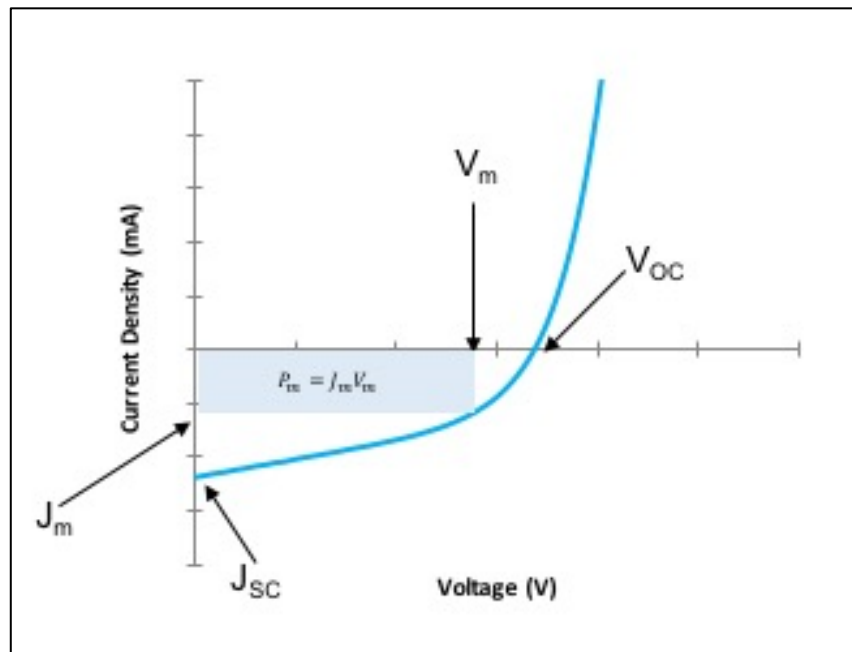
Figure 1.7: Current against voltage curve

The key values of interest are the short circuit current, J_{SC}, the open circuit voltage, V_{OC}, series resistance, shunt resistance and the FF, which tells us how well

the device is made. The power conversion efficiency, PCE(η) of the device is described mathematically in terms of the these key values (Equation 1.3)[23]:

$$PCE\ (\eta) = \frac{V_{OC}J_{SC}FF}{P_{incident}}$$

<div align="center">**Equation 1.3**</div>

where the $P_{incident}$ is the power of the incident light. The short circuit current, J_{SC}, is a measure of the maximum number of electrons generated in the device. There are several factors that can result in a changed maximum generation rate of charge carriers: - 1) a change in the absorption (η_A), which may change due to a change in morphology or crystallinity of the active layer, or a change in layer thickness. 2) a change in exciton diffusion efficiency (η_{ED}), this is due to changes in the thickness, changes in the morphology or crystallinity of the active layer or changes in the phase separation and domain sizes. It is important to note that these changes do not depend on the voltage, so therefore will result in a vertical shift of the J-V curve[24].

The open circuit voltage, V_{OC}, is related to the gap between the HOMO of the donor and the LUMO of the acceptor. This is a very important parameter. Factors that can affect the V_{OC} are[24]:- 1) Change in the generation rate, as a higher generation rate means higher charge carrier density which will lead to higher V_{OC}. 2) Change in the gap between the HOMO of the donor and the LUMO of the acceptor (E_g^{DA}), this can be due to different donor (acceptor) materials or can also be due to changes in morphology or crystallinity of the active layer which leads to changes in the polarization energies. 3) Changes in the recombination rate, as at a given generation rate, a higher recombination rate due to impurities and defects will decrease the amount of charge carrier which leads to decrease V_{OC}. 4) Shunt resistance due to non-continuous layers and high surface roughness caused by crystalline materials will lead

to loss in V_{OC}[24]. The fill factor, (FF), measures how well the device has been made, it takes into account the microstructure of the device by measuring the squareness of the J-V curve[25]. From the curve FF can be measured by the Equation 1.4[23]:

$$FF = \frac{J_m V_m}{J_{sc} V_{OC}}$$

where J_m is the current at the point where the curve is at its maximum power output and V_m is the voltage at the point where the curve is at its maximum power output, as seen in Figure 1.7. Therefore, to improve the efficiency of these devices, the J_{SC}, V_{OC} and the FF need to be increased as the efficiency is directly related to the J_{SC}, V_{OC}, and the FF as seen in Equation 1.3.

The FF is also affected by the series and the shunt resistances of the devices and by the recombination of charges. The series resistance is caused by movement of current through the active layer, interfaces, junction of the solar cell. The main impact of series resistance is to reduce the FF, although excessively high values may also reduce the J_{SC} as the series resistance alters the slope of the J-V curve near the V_{OC}. The shunt resistance is usually due to manufacturing defects rather than poor solar cell design. It arises because of leakage of current across the junction[25]. The shunt resistance alters the slope of the J-V curve near the J_{SC}. For an ideal cell, the series resistance should be 0 and the shunt resistance should go to infinity[26] as $slope = \frac{I}{V} = \frac{1}{R}$, therefore at V_{OC} I/V needs to be high for R to be low. Other factors that can result in changes in the FF are[24]:- 1) Changes in the carrier charge mobilities, as high charge mobilities will increase the chances for charge collection. Charge mobility can change due to different morphology or crystallinity of the active layer. An imbalance of charge mobilities can also cause a lower FF. 2) If the active layer thickness is

9

increased, a higher rate of recombination losses would result; which leads to lower FF. 3) An increase in the recombination will decrease the FF. 4) As the FF does depend on absorption intensities, it is affected by the change in overall absorption which can be seen by the changes in the J_{SC}[24].
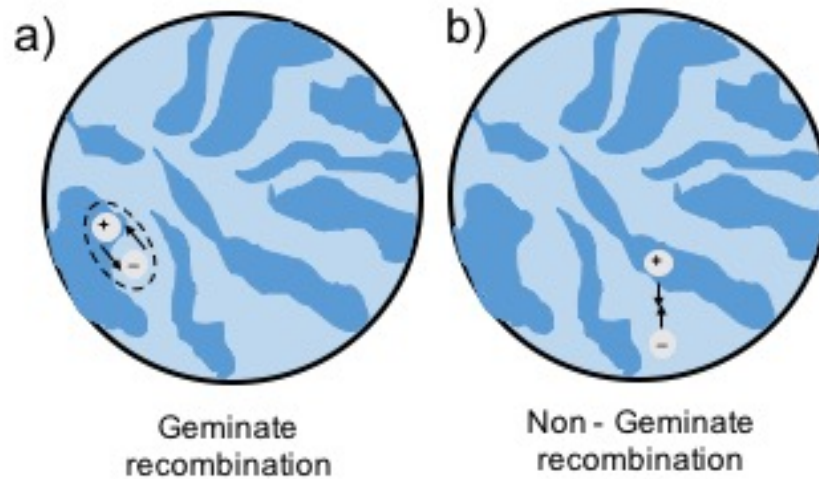
Figure 1.8: Illustrations of (a) geminate pair dissociation and (b) non-geminate recombination mechanisms in BHJ- OPVs

Recombination results in the loss of photogeterated charge carriers. Reducing recombination is critical for increasing V_{OC} and FF as mentioned above and therefore increasing the efficiency of the solar cell. There are two types of recombination mechanisms (as shown in Figure 1.8[26]) :- 1) Geminate recombination, which is recombination of non-separated charge carriers at the interface, but just after exciton dissociation[26, 27]. 2) Non geminate recombination, which is a bimolecular mechanism and is the recombination of dissociated charge carriers which are generated from different exictons[26, 28]. Understanding both these mechanisms is important and the relative contributions are dependent on the system being studied. It is important to note that both these mechanisms have very similar effects on the J-V curve[26].

1.2 Photophysical properties of organic photoactive materials

1.2.1 Jablonski diagram
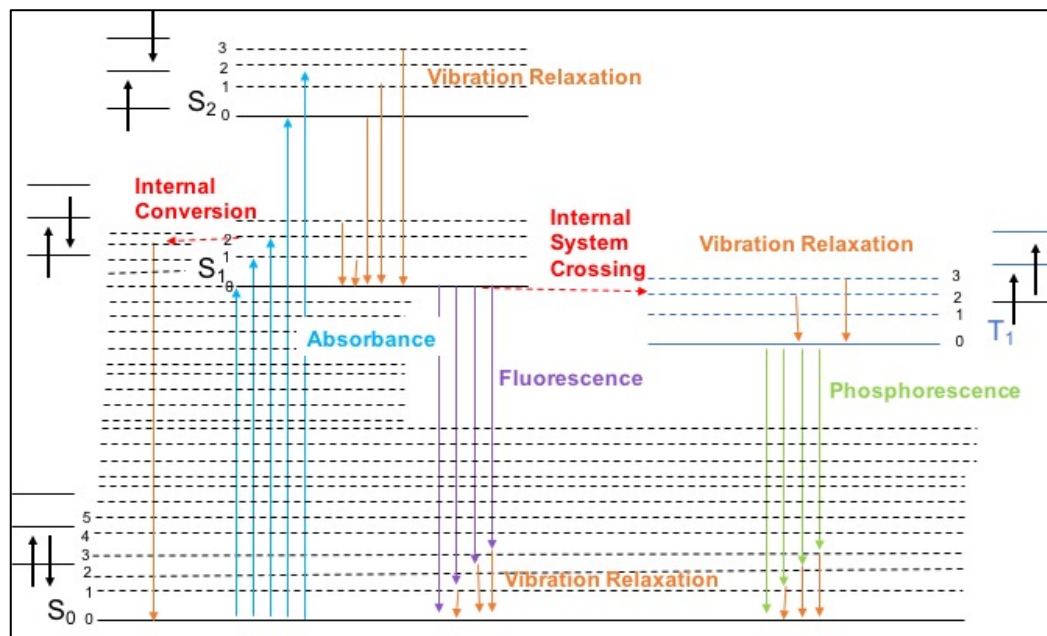
Figure 1.9: A Jablonski diagram to illustrate the photophysics of organic molecules

The Jablonski diagram is an energy level diagram, arranged with energy on the vertical axis. The Jablonski diagram shows all the possible electronic transitions in an organic molecule, when the molecule interacts with light (Figure 1.9). The horizontal line denotes the energy level or the eigenstates for an electron in a molecule. The bold horizontal lines represent the ground state (S_0), the first excited state (S_1), second excited state (S_{2s}) and the first triplet state (T_1). The dashed horizontal lines between the electron states are the vibronic energy levels (shown on the diagram as 0, 1, 2, 3...). These vibrational energy levels have higher energy than the corresponding electronic state as these vibrations sit on top of the corresponding electronic distribution related to a set of bonds for the molecule in that electronic state. Each vibrational level can be divided into enormous numbers of rotational sub-energy-levels. In the Jablonski diagram the excited states are arranged by their multiplicity,

singlet states on the left (S_1, S_2…) and triplet states on the right (T_1, T_2…). The ground state (S_0) has a multiplicity of 1 as all the orbitals contain paired electrons. The paired electrons have opposite spins; therefore, the overall spin is 0. The excited singlet states (S_1, S_2…) also have a multiplicity of 1, as when the electron is excited, it does not involve a change in the electron spin, and therefore the overall spin is 0. The excited triplet states (T_1, T_2…) are indicated to have an energy lower than that of the excited singlet state, this is because of the spin correlation. The excited triplet state has a multiplicity of 3. When an electron is excited to the triplet state, it involves a change in the electron spin, therefore the overall spin is 1.

1) Absorbance

Absorbance is the first transition in the Jablonski diagram, which is denoted by the blue arrows in Figure 1.9. Absorption occurs when an electron interacts with a photon, resulting in a transition of an electron from the ground state to a higher excited state. Only certain wavelength of photons that have energies that match the difference in the energy gap between the two eigenstates can be absorbed. Fermi's Golden Rule says that the probability of each transition is proportional to the coupling between the eigenstates[4, 29]. Absorption is a really fast process, it occurs at an average time scale 10^{-15}s[24]

2) Vibrational relaxation and Internal conversion

Once an electron is excited to a vibrational level of an excited state (ie. v=1, S_1) the electron can relax down to its vibrationless excited state (v=0, S_1). This is shown by the orange arrows in Figure 1.9, and is known as vibrational relaxation. Vibrational relaxation is a non-radiative process, as the vibrational excitation energy is removed by collisions to adjacent molecules or in the form of heat. This process is a fast (often in the 10^{-14}-10^{-11}s[24]) and therefore occurs right after absorbance.

12

Another non-radiative process that can occur, if vibrational energy levels strongly overlap electronic energy levels, is an electron can transition from a vibrational level (ie v=2, S_1) to another 'hot' vibrational level in a lower electronic state (ie. v=24, S_0). This is known as internal conversion, and is denoted by the red dotted arrow in Figure 1.9. After the electron is transferred to the hot vibrational level of the electronic ground state, the electron will then decay back down to the vibrationless energy of the ground state. Internal conversion is a really fast process; it occurs at the same time scale as vibrational relaxation.

3) Fluorescence

Fluorescence gives us a way to monitor the excited states of an organic molecule, so it is an important property. After an electron has relaxed to its vibrationless energy level of the first excited state (v=0, S_1), the electron can decay down to the ground state (S_0) by emitting a photon. This is known as fluorescence and it is a radiative process, it is denoted by the purple arrows in Figure 1.9. As seen in the Figure 1.9, this is the reverse process to absorbance. In this process, the photon that is emitted has less energy than the photon that is absorbed this is due to the fact that energy is lost during vibrational relaxation. Fluorescence is a slow process as it is on the order of 10^{-9} to 10^{-7}s[24].

4) Intersystem crossing and phosphorescence

Another pathway a molecule can take from the first singlet state is called intersystem crossing. In this process, the electron can transfer from the first singlet state to the first triplet excited state. Intersystem crossing does involve the changes in the electron spin multiplicity. This transition is indicated by a horizontal dashed red

arrow in Figure 1.9. This is the slowest transition on the Jablonski diagram, it is on the order of 10^{-8} to 10^{-3}s[24]. Intersystem crossing is a non-radiative transition. Intersystem crossing leads to an interesting pathway back down to the ground electronic state which is called phosphorescence. Phosphorescence is a radiative transition from the first excited triplet state to the singlet ground state. It is denoted by the green arrows in Figure 1.9. This process is much slower than fluorescence due to the change in the electron spin multiplicity, it is on the order of 10^{-4} to 10^{-1}s[24].

1.2.2 Photophysical properties of material in OPV

These photophysical properties are very important in understanding how these materials work in an OPV device. As discussed in section 1.1, there are 5 important steps for the power conversion in an OPV device. The overall efficiency of the device is based on the efficiency of all the individual steps. In this study, our goal is to draw connections between the morphology of the active layer and how it can affect the photophysical properties and the device performance to help us better understand squaraines for solar cell applications.

As seen we already know absorbance is very important, as it is the first step and it tells us how efficient squaraines are interacting with light. The more photons absorbed by SQ, the more excited states will be generated. For the material to absorb a lot of photons, SQ needs to have a high molar absorptivity and needs to absorb over a wide range of wavelengths. The other thing that can affect the absorption and the efficiency is the thickness of the active layer.

Another key property is the fluorescence lifetime. The fluorescence lifetime is associated with the kinetics of the excited state of the molecule. This is the lifetime of an electron staying in the excited state before it relaxes back down to the ground state

through fluorescence or other pathways. For an ideal material for OPV, the longer the excited state lifetime, the further the distance the exciton can travel through the active layer to the interface. This is an important property to keep in mind when thinking about BHJ OPV. If the excited state lifetime is small, the exciton won't get to the interface to be separated in to free charges.

The exciton diffusion length (L_D), is another parameter that is important. This is known as the distance the exciton can travel before the exciton relaxes back down to the ground state. This is a key parameter when thinking about the morphology of the active layer; if the diffusion length is small, then the exciton will not be able to reach the donor/acceptor interface. This distance is dependent on the exciton lifetime and the morphology. If there are large pure domains, the distance the exciton needs to travel to reach the interface will be large; therefore, the exciton may not reach the interface. Another consideration to remember is that if the domain is crystalline the exciton can travel further than if the domains are amorphous in the active layer.

In conclusion, the properties for an ideal material for OPV are: high molar absorption coefficient, absorption over a wide range of wavelengths, long excited state lifetimes and the ability to crystallize. These photophysical properties can and will be different in the solid state compared to when these materials are in solution due to stronger bonding interactions. Also, these properties can also change when the material starts to crystallize. Using techniques like thermal and solvent vapor annealing, can cause the material to crystallize. Therefore, our goal in this work is to understand how crystallization in the active layer changes the morphology of our active layer and therefore how it would affect our device efficiency.

1.3 Materials

As most of these efficiencies are based on the materials used, it is important to choose materials that will optimize these properties, so that the efficiency of the device is improved. In these devices, the materials that will be used are Squaraines (SQ) and Poly(3-hexylthiophene-2,5-diyl) (P3HT) as the donor materials and Pheny-C61-butyric acid methyl ester (PCBM) as the acceptor material.

1.3.1 Poly(3-hexylthiophene-2,5-diyl)

Poly(3-hexylthiophene-2,5-diyl)[7, 8] (Figure 1.10) is currently used as a benchmark material in most OPV devices. As it is a semiconducting polymer, with a small band gap. It absorbs and emits light in the ultraviolet and visible region of the solar spectrum respectively. It is soluble in most organic solvents, which is important for the spin casting technique and solution processing in general.
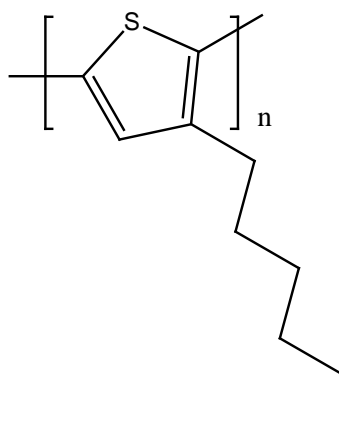
Figure 1.10: General structure of P3HT

1.3.2 Squaraines

Squaraines[10-14, 30] (Figure 1.11) are a new class of organic molecules. Squaraines comprise a unique aromatic four-membered carbon ring system, with two electron – rich side groups and an electron deficient center.

DHSQ(OH)$_2$: R= n-hexyl
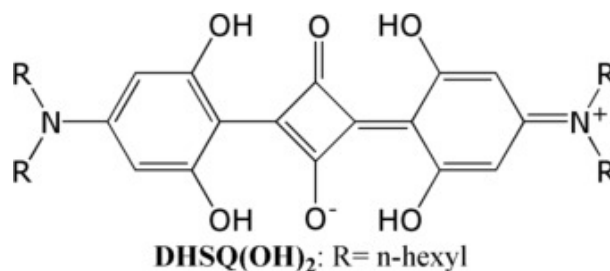
Figure 1.11: General structure of Squaraines

The electronic structure of squaraines is described as donor – acceptor – donor (D-A-D); the electron donor groups are the two-anilino groups on both sides and the electron acceptor is the central four – membered ring. Donor-acceptor type molecules are important, as this type of molecule has a lower energy band gaps (less than 1.5 eV)[30] so there is more overlap of the photon rich NIR region of the spectrum, which will improve the efficiency of OPV[31]. Squaraine dyes have high extinction coefficients (>10^5 Lmol^{-1}cm^{-1})[32], sharp absorption bands and fluorescence spectra in the red and near infrared region in solution but there are very broad and varied absorption spectra in the solid state[12].

Squaraines are chosen as materials for OPV devices because they possess: (1) the high extinction coefficients of these molecules in the near IR region of the solar spectrum[12]; NIR light cannot be absorbed by materials like P3HT[33]; (2) they are stable towards light and thermally stable[34]; (3) they have a conjugated π system, (4) as push – pull molecules, they have a lower energy band gap[35] as described in Figure 1.12.
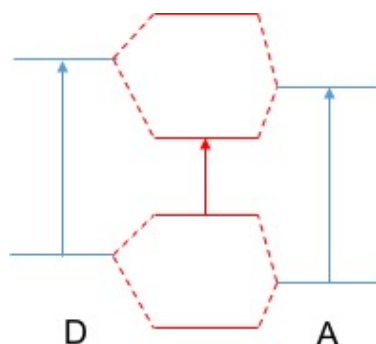
Figure 1.12: Illustration of the bonding in a D-A material

As seen in Figure 1.12, the horizontal lines represent the HOMO and the LUMO of the donor and acceptor molecules by themselves. The blue arrow represents the energy gap between the HOMO and LUMO of the donor and acceptor respectively. The red horizontal lines represent the molecular orbital of the now covalently bonded donor and acceptor molecules. The red arrow denotes the energy gap between the HOMO and LUMO of this bonded molecule. It can be seen that there is a lower energy gap for the D-A material compared to the donor and acceptor material respectively.

Furthermore, the packing of Squaraines in the solid state is typically a function of the solubilizing side groups. Therefore, the packing morphology can be readily changed by simply changing the side groups. As seen in Figure 1.13, by changing the side groups, there is a small effect on the V_{OC}, as there are changes to the HOMO of the donor molecules[36] (Squaraines molecule) in the OPV device.
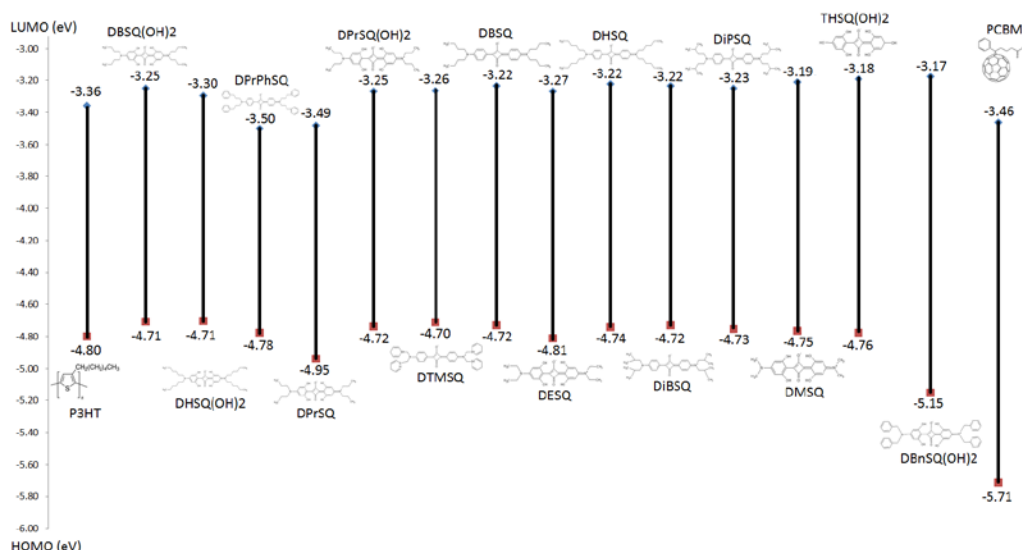
Figure 1.13: Cyclic Voltammetry Data in solution showing how changing the R groups impacting the HOMO and LUMO, collected by James Sinka (Collison Group Communication)[37]

Again, as you change R groups on the squaraines the photochemical properties do not change much in solution but in solid state their absorption spectra are dependent on the R group due to the different aggregation of these molecules. Aggregation is important to the OPV devices as we shall see how it broadens the absorption band and it will change the extinction coefficients.

The squaraine molecule that will be studied in this work is a symmetric aniline-based squaraine with n-hexyl chain on the molecular arm with di hydroxyl substituents on the aniline, this will be referred to DHSQ(OH)$_2$ (Figure 1.11)

1.4 Aggregate of squaraines

The solid state (thin films) absorption spectra of squaraines differ from the absorption spectra in solution. (Figure 1.14). As seen in Figure 1.14, the DHSQ(OH)$_2$ spectrum in solution (blue line) has a sharp and narrow absorption peak at 645 nm

with a shoulder at 600 nm, whereas in the solid state, the absorption spectrum is broadened giving rise to two peaks, one at 550 nm and the other at 650 nm. This is due to self-organization of the squaraine molecules due to the intermolecular forces between the molecules.
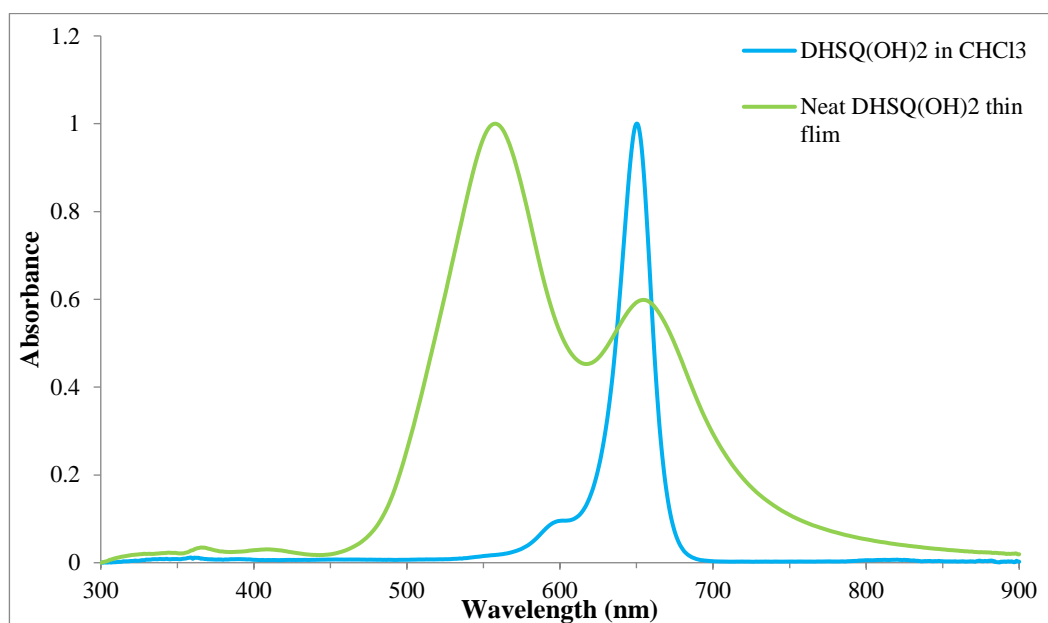
Figure 1.14: Normalized absorption spectra of DHSQ(OH)$_2$ squaraine in solution (no aggregation) (blue line) and in solid state (with aggregation) (green line)

Dyes can give rise to two different type of aggregation: - one which is blue shifted, compared to the monomer band of the solution spectra known as the H – aggregate and the other which is red shifted compared to the monomer band of the solution spectra known as the J – aggregate[3]. This can be explained by the molecular exciton coupling theory[38], which describes the coupling of the transition dipole moments when two monomer molecules are brought together.

1.4.1 Exciton theory

The H- aggregate arises due to monomer units with parallel transition dipoles (Figure 1.15[38]). In Figure 1.15, the ovals show the molecular arrangement and the double arrow is the transition dipole moment for the molecular electronic transition. The transition from the ground state to the excited state is only allowed when the sum of the dipoles is not zero. Therefore, for the out of phase diagram, corresponding to lower energy (S⁻), the dipole moment cancels out due to opposing monomer dipoles and this is a forbidden transition. Whereas for the in-phase diagram (S⁺), the transition dipole moments add up due to the aligning monomer dipoles and, therefore this is an allowed transition. Due to this only the higher transition (S⁺) is seen and corresponds to the H- aggregate, which is blue shifted from the monomer peak.

Similarly, the J- aggregate arises due to monomer units with head-to-tail transition dipoles (Figure 1.16).
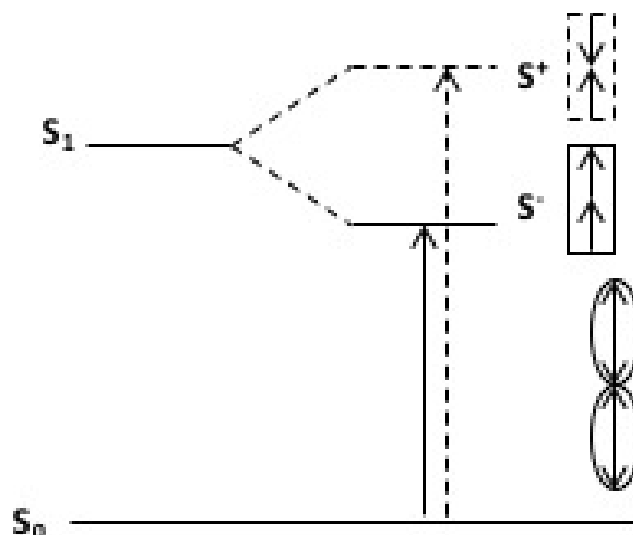
Figure 1.16: Energy diagram for squaraine molecules with head-to-tail transition dipoles[38]

In Figure 1.16[38], the ovals show the molecular arrangement and the double arrow is the transition dipole moment for the molecular electronic transition. The transition from the ground state to the excited state is only allowed when the sum of the dipoles is not zero. Therefore, for the in-phase diagram, corresponding to lower energy (S^-), the dipole moments add up, due to their alignment. This transition is allowed. Whereas, for the out of phase diagram, which corresponds to higher energy (S^+), the dipole moments cancel out due to opposed transition dipoles. This is a forbidden transition. Therefore, only the lower transition (S^-) is seen and corresponds to the J- aggregate, which is red shifted from the monomer peak.

Aggregation is important in squaraine OPV as changes the energy level and broadens the absorption spectra. It is also correlated with the morphology of the active layer which impacts the exciton diffusion, dissociation and charge mobility in the active layer, as it gives rise to crystallinity. These properties will impact the efficiency of the solar cell. When aggregates form, the active layer is packed in a

more ordered form, therefore helping to sweep the charges out, so increasing the charge mobility[39].

The morphology of these OPV devices can be made up of three phases: pure domains, mixed aggregated donor and acceptor domain and mixed amorphous regions. A mixture of all of the three phases is known to be favorable but it depends on the level of aggregation and domain size, which is due to phase separation and purity. Low domain purity can lead to an increase in geminate and non-geminate recombination[39]. If there is a complete homogeneous mixture of SQ and PCBM, this can provide good exciton quenching and charge generation, but this will also lead to a decrease in charge mobility, due to the active layer being amorphous and an associated increase in recombination which is bad for OPV. There is always a trade-off between the level of exciton diffusion and domain size; with large domain size, the exciton diffusion length would increase for the exciton to reach the interface. With too small a domain size the greater the charge dissociation, but the more tortuous the path between the donor/acceptor interface and electrode. So to achieve high efficiency OPV performance, understanding how to control phase separation and aggregation is key[40].

1.4.2 Annealing

Annealing is one of the methods used to control the morphology of the active layer. There are there two types of annealing: 1) thermal annealing (TA) and 2) solvent vapor annealing (SVA); both are effective methods for changing the morphology of the active layer. Thermal annealing relies on heating the substrate to a temperature greater than the glass transition temperature and approaching the melting

point of the material, allowing the molecules to move and orient themselves in a more favorable confirmation[35].

Amorphous SQ/PCBM mixed phase

SQ aggregate

SQ - molecule
PCBM - molecule

Substrate

Annealing

Substrate

PCBM cluster

Amorphous SQ/PCBM mixed phase

PCBM cluster
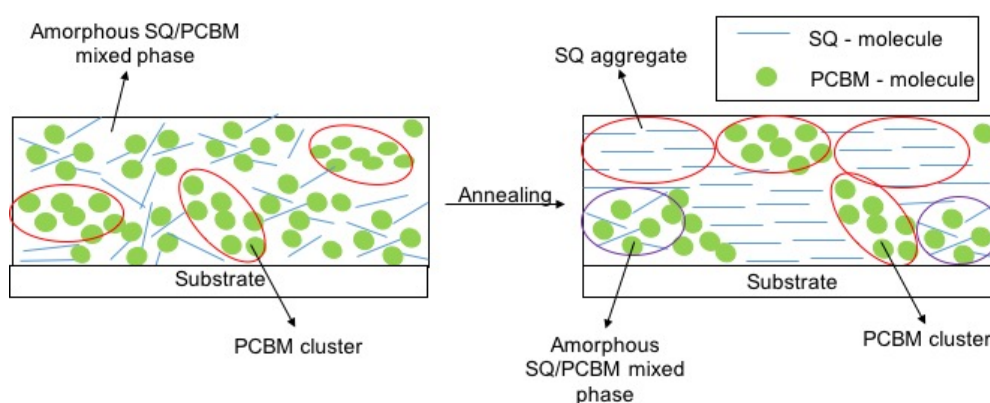
Figure 1.17: Effects of Annealing

As seen in Figure 1.17, the SQ molecules begin to aggregate, expelling isolated molecule of PCBM from the mixed phase and allowing the PCBM molecules to diffuse and combine into larger aggregates. The efficiency of the OPV device is increased as thermal annealing ultimately reduces recombination, increases phase separation and improves charge transport[4]. This is due to the formation of pure crystalline domains in the active layer. In addition, solvent vapor annealing uses solvent vapor, making both components able to diffuse through the active layer. The solvent vapor acts as a lubricant through which the active layer material can phase separate. Greater "fluidity" helps aggregation of the SQ and segregation of PCBM[35]. The choice of solvent is important when solvent annealing, as a solvent that evaporates at a slower rate will produce a larger degree of separation. Phase separation is also influenced by the difference in solubility between the SQ molecule and PCBM molecule in that solvent being used to anneal[4]. Solvent annealing has been shown to promote segregation of PCBM to the top of the device, therefore enhancing charge transport properties like thermal annealing[35].

24

As mentioned earlier, it is critical in understanding how to be able to control the trade-off between aggregation and phase separation in Squaraine – Fullerene bulk heterojunction organic photovoltaic devices. As ordering/packing of the molecules to form crystals or aggregates is expected to be beneficial. Too much phase separation is expected to be detrimental. Aggregation and phase separation tend to occur together and therefore if the annealing processed is not controlled then the phase separation cost outweighs the aggregation benefits. As we have seen a lot of factors can change the morphology of the active layer. Therefore, in this work we will be further understanding how different factors can be used to control the degree of aggregation and further optimizing the efficiency by understanding the effects of blend ratio of the donor and acceptor material in the active layer and effects of annealing.

Chapter 2 : Experimental Methods

2.1 Materials Preparations

Squaraines are synthesized by Dr. Jeremy Cody's research group at the School of Chemistry and Material Science at RIT. Phenyl-C_{61}-butyric acid methyl ester (PCBM) was purchased from Solenne b.v. and was used as received. The reagent solvents purchased from Sigma Aldrich, were used as received without any further purification. The Squaraines and PCBM materials were kept in a N_2-filled glove box with O_2 levels $\leq$ 20-40 ppm and H_2O levels $\leq$ 50 ppm.

All the solutions were prepared in pre-cleaned 20 mL scintillation vails, which were capped using a lid and parafilmed after the solvent was added to prevent any change in concentration of the solution due to evaporation of the solvent. The solutions were sonicated for 10 minutes in order to make sure the materials were fully dissolved.

To prepare films for absorbance, the solution was spin coated on a microscope slide which was used as the substrate. For device making, ITO coated slides were used as the substrate. The microscope slides were sonicated in Acetone for 30 minutes and then rinsed twice in hot deionized water; then sonicated in Isopropyl Alcohol (IPA) for 30 minutes and then rinsed in hot deionized water again before spin coating. The cleaning procedure for the ITO substrates, can be found under device fabrication below. The solution was spin coated using a Chemat spin coater (model KW-4A). The spin speed used was 1500 RPM for 18 seconds unless otherwise specified.

2.2 Spectroscopy

2.2.1 UV-Vis Measurements

Absorbance measurements were applied to neat squaraine and

Squaraine:PCBM blends in solution as well as in solid state films. All measurements

in solution were made using a 10 mm quartz cuvette. Measurements in thin film were

made using a film holder. All measurements were made at room temperature.

Absorbance measurements were made on a Shimadzu UV-2401 PC UV spectrometer.

The instrument parameters were set to a medium scan speed, 2 nm slit width and 0.5

nm sampling interval for all samples. The scan range was set to wavelengths from 300

nm to 900 nm for all the measurements. For the solution measurements, the

spectrometer was baselined with the pure chloroform, unless otherwise specified, to

account for scattering and absorption of solvent. For thin film measurements, the

spectrometer was baselined with a blank microscope slide to account for scattering

and absorption of substrates. Three measurements were taken for each film by

changing the film position in the light path to account for any heterogeneity in the

films. All measurements reported for absorbance intensity in this work are therefore

averaged across the three film measurements, and then across two films that have

been prepared from identical solution. This gives 6 measurements per reported

measurement in this thesis.

2.2.2 Transmission Electron Microscopy

Transmission Electron Microscopy (TEM) is a very useful surface technique,

in which a beam of electrons is transmitted through a thin sample. This beam of

electrons interacts with the sample as it passes through it, and forms an image which

is then magnified and focused on to a fluorescent screen so that the image can be recorded. This technique can be used to create a map of the film at a nanoscale level that provides contrast for presence of carbon, nitrogen, or Sulphur, respectively. Note that different densities scatter the electrons to different extents. By using this technique, we can study the composition and location of nanoscale domains within the bulk material.

The active layer materials for transmission electron microscopy (TEM) were spun cast on microscope slides. Films were floated-off in deionized water and picked up with copper TEM grids. The water was allowed to evaporate under ambient conditions. TEM experiments were performed using a JEOL JEM-2010 operating at 200 kV with a 210 LaB6 filament and an AMT image capture system. The average domain size was calculated by using ImageJ software.

2.3 Device Fabrication Standard Operation Procedure

Cleaning the substrate

Acetone in the bottle was changed every time a new batch of devices was made to make sure it is clean and there is nothing in there to contaminate the substrate. The bottle was filled with acetone about 1/4th of the bottle. An air gun (air pressure ~ 20) was used to remove particles from the substrates (9 slides) before putting it in acetone. Only tweezers were used once/after the substrate is in acetone. ITO substrates were cleaned via sonication in acetone for 30 minutes. At this point it is confirmed that the water is at the right level in the sonication bath. It was made sure that the bottle was placed in the spot where the vibrations were the most (indicated by lots of bubbles) and that water level was at the notch on the inside of the metal bath of the sonicator.

<u>Clean vials</u>

Four vials was obtained for active layer, chloroform, PEDOT:PSS and water. Each vial was washed with chloroform, which will remove any residues left in the bottom of the vial.

Each vial was rinsed 3 times with chloroform. Once rinsed, each vial was dried with the air gun and then put into the vacuum oven for 10 minutes at the temperature setting 6, to evaporate off any residual solvent. The vials were then taken out and cooled before being labelled.

<u>Further clean the substrate</u>

IPA (Isopropyl alcohol) in the bottle was changed every time a new batch of devices was made to make sure it is clean and there is nothing in there to contaminate the substrate. The bottle was filled with IPA about 1/4th of the bottle. The substrates were pulled out from the acetone bottle and were put into deionized water and then the air gun (air pressure ~ 20) was used to blow off any water residues from the substrates before putting it in IPA. The water was frequently changed while cleaning the substrates. The ITO substrates were further cleaned via sonication in IPA for 30 minutes. At this point it is confirmed the water was at the right level in the sonication bath. It was made sure the bottle is placed in the spot where the vibrations were the most and that water level is at the notch on the inside of the metal bath of the sonicator.

Preparing solutions

<u>Prepare the donor acceptor solution</u>

While the substrates were sonicating, the active layer solution is prepared. The appropriate masses of SQ and PCBM are weighed into the cleaned vials, and the

necessary amount of chloroform was added. The bottle was capped and sealed with

parafilm and sonicated for 10 minutes. Once finished sonication the solution was

moved in the glovebox for spin casting.

<u>Prepare the PEDOT:PSS</u>

The PEDOTPSS bottle is kept in the fridge. This solution must be kept cold,

to prevent the PEDOT and PSS forming crystal. A 5 mL syringe and a 0.45 μm

syringe filter were taken out and assembled. The PEDOT:PSS (was purchased from

Ossila) solution was diluted in deionized water at a ratio of 1:1. 1.5 mL of pre-

prepared solution was put into the syringe and 1.5 mL of deionized water was added

into the syringe. A total volume of PEDOT:PSS solution is 3 mL after diluting. The

solution was forced through the filter into the clean vial. This filtration process

removes the aggregates/crystals that have formed in the pre prepared PEDOT:PSS

solution. This solution is kept in the fridge until you are ready to spin coat the

substrates.

Taping the slides

The substrates were pulled out from the IPA bottle and put into in deionized

water and then the air gun (air pressure ~ 20) was used to blow off any water residue

from the substrates and placed onto a clean kimwipe. To determine which side has the

ITO, the multimeter was used in the audible setting (set it to the sound wave setting)

and tested for resistivity. Tape must be put on the films (Figure 2.1) to protect the ITO

contact for when the devices were being tested, as it can be removed to expose the

ITO contact. This was done by cutting tape on a glass slide and then placing it onto

the film using tweezers. The tape must be smoothed out to assure it is affixed to the

substrate, with no bubbles present. This was done to all the slides and then placed in

on a clean petri dish and then placed into the vacuum oven (150°C) for 30 minutes to remove any solvent residual.
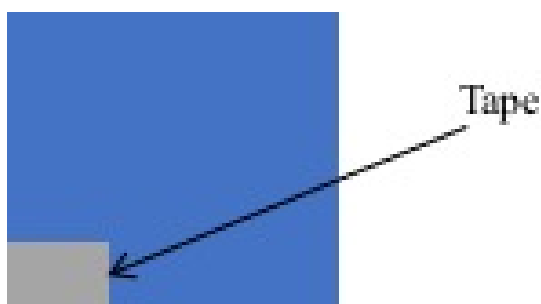
Figure 2.1: Taping the substrates

Spin Coating Process

Spin Coating PEDOT:PSS

The PEDOT:PSS was spin coated on the clean ITO at a spin speed of 5000 RPM for 50 seconds. It was then made sure the Vacuum pump is connected and working properly by testing it, with a non-prepared slide. This process work best when the PEDOT:PSS was cold and the ITO slide are warm. Therefore, the previously prepared PEDOT:PSS was taken out from the fridge and the slides from the oven. To spin coat the PEDOT:PSS, the slide was placed at the center and the vacuum was turned on, so that the slide doesn't move. Some PEDOT:PSS solution was sucked up into a pipette and spread it over the slide, and be careful not to touch the ITO. It was made sure there are no bubbles formed on the slide, and then the start button was pressed. The pipette tips were changed often so that the PEDOT:PSS doesn't aggregate. Once the spin coater had stopped, the slide was removed from the spin coater holding it from the tape so it doesn't destroy the layer of PEDOT:PSS. Then this process was repeated for all the other slides and once done transfer the films into the vacuum oven and the slides were baked for 15 minutes at the setting 7 at vacuum.

<u>Spin coating active layer</u>

Make sure everything that is needed was transferred into the glove box, make sure the active layer solution, your PEDOT:PSS coated films were in the entry port before entering the glove box. Before starting to spin coat, it is made sure that the spin coater vacuum pump was turned on. Using a test substrate to set the spin coater at 1500 RPM for 18 seconds. The slide was placed at the center of the spin coater and using a pipette with a set volume of 100 μL, suck some of the active layer solution into a pipette and drop it at the center of the of the slide and then the start button was pressed. Once the spin coater had stopped, remove the slide from the spin coater holding it from the tape. Then this process was repeated for all the other slides.

Preparing to evaporate the aluminum

<u>Moving materials into the second glove box</u>

Once finished place the slide into the petri dish. The latch was opened, and the tray was pulled out. Set the covered slides on the tray. The latch was closed and evacuate and wait for 15 minutes. Then Refill and then evacuate one more time, then immediately refill. Then remove the films from the antechamber.

<u>Clean device plastic holder</u>

Device holders were cleaned with IPA and labelled with the type of devices and the number them 1 – 8 and transferred into the glove box.

Evaporate the Aluminum

After all the films were loaded onto the mask, the aluminum stencil was screwed on and the sides were taped so that it doesn't move. The mask holder was screwed onto the evaporating instrument, on the lid. Two pieces of aluminum were

placed on the holder at the bottom and the lid of the evaporator was closed and then the start button was pressed. The power should be increased then decreased back to 8W and 1350 Hz.

<u>Deposition of aluminum</u>

For deposition to begin, the pressure in the aluminum chamber should be 10^{-6} ~10^{-7} torr. The starting temperature, pressure, current and voltage (should be unchanged 0.2A and 36V) from the right operational pad were recorded. The crystal life from the left operational pad were recorded.

Once done recording, press "start layer" button. The power level was increased from 0 to 30 in increments of 1 by rotating the knob in every 5 seconds. The pressure and deposition rate at each power level is recorded. Stay for 30 seconds at power level of 30, then resume incrementing power levels by 1, every 5 seconds till level 55. The maximum power level is 55. The system will automatically shut down once the thickness has reached 200 nm and pressure inside the chamber will return back to ambient level. After about 10 minutes and the right operational pad displays "pressure over". Open the chamber and take off the device holder. Take off the tape carefully and use tweezers transport device into its corresponding film holder one by one. When the transportation is finished, put everything where it originally belongs and take out the rubbish (tapes and gloves).

2.4 Solar Simulator

Current Density-Voltage (J-V) characteristics of a device is a basic method for photovoltaic devices. These measurements provide us with three parameters which help use evaluate the OPV devices: short-circuit current (J_{SC}), open-circuit voltage (V_{OC}) and the fill factor (FF).
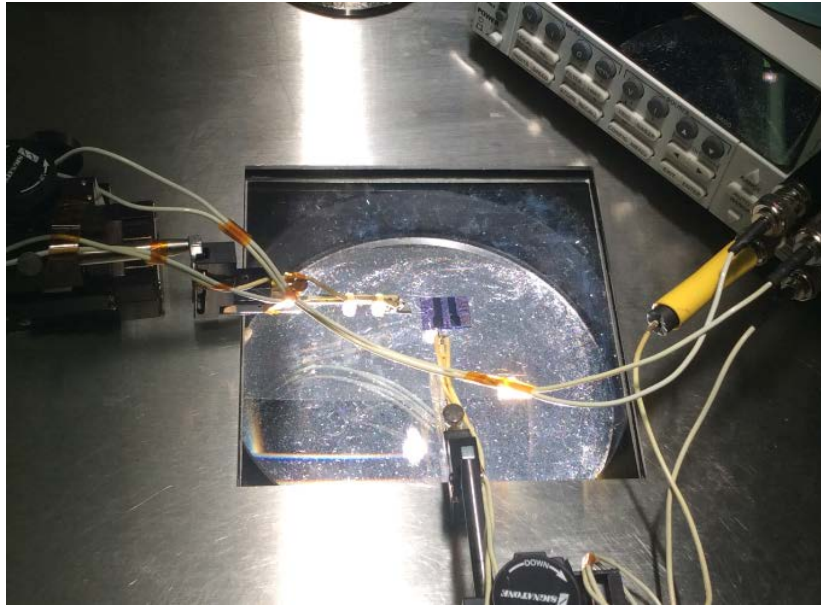
Figure 2.2: Solar Simulator testing apparatus

The J-V curve of the OPV devices is measured by using a Newport 91159 Full Spectrum solar simulation, under 1 sun, 100 mW cm^{-2}. The solar simulator uses a xenon lamp, which is calibrated with a round robin InGaAs photovoltaic cell fabricated at NASA. The solar simulator is calibrated every 3 weeks. The devices were tested immediately after evaporation of the aluminum contact, so the devices don't degrade due to material degradation as they devices were not encapsulated. The devices were measured by using a 4 – point probe with a Keithley 2400 source meter. The data was collected using an internally developed LabView program. The devices were placed in the same location on the testing surface every time to reduce errors. Figure 2.2 shows the set-up of the solar simulator used during testing.

Chapter 3 : Squaraine in PMMA solid solution

3.1 Introduction

From Figure 1.14 in the introduction, we know that in thin films there is a broadening of the spectrum due to aggregation. Within the active layer in OPV devices, the aggregation can be controlled by changing the blend ratio of $DHSQ(OH)_2$:PCBM[41]. When the blend ratio is changed, there is a change in the spectrum (Figure 3.1). In Figure 3.1, the peak at 320 nm is the absorbance of $PC_{61}BM$, which was chosen because it does not overlap with the squaraines absorbance, whereas $PC_{71}BM$ does. The $DHSQ(OH)_2$ in Chloroform solution (grey), shows the monomer peak at ~652 nm. The spectra of the neat $DHSQ(OH)_2$ film (green), blend ratios 1:1 (light blue), 1:2 (red), 1:3 (orange) and 1:5 (purple), all show two absorbance maxima, a high energy peak at ~563 nm and a low energy peak at ~666 nm. Note that the low energy peak is seen to red shifts as the concentration of PCBM is increased (Figure 3.1b). In the next chapter, we will talk about how blend ratio affects device efficiency.
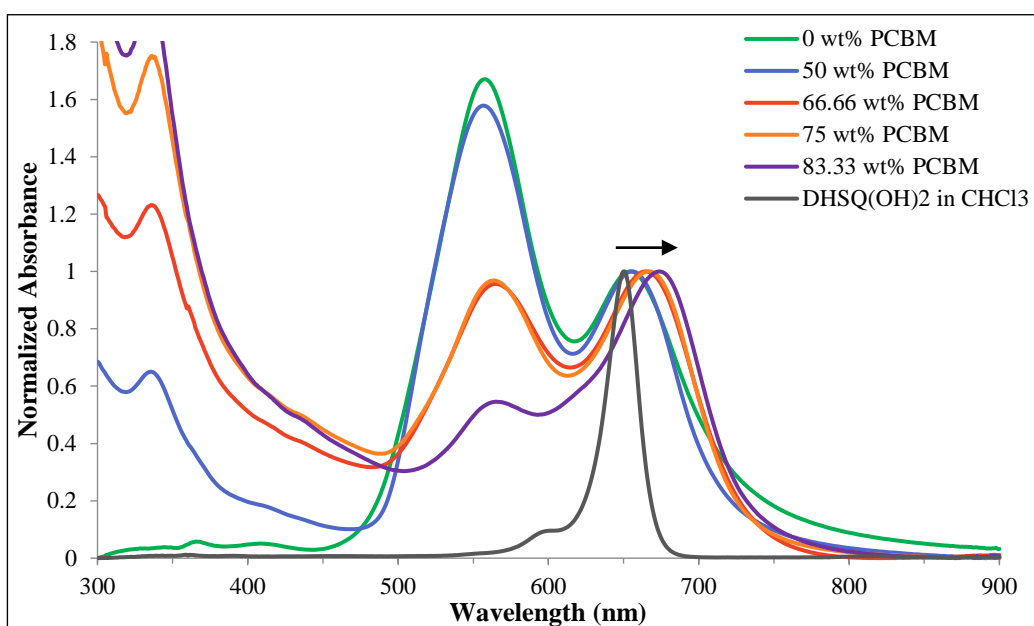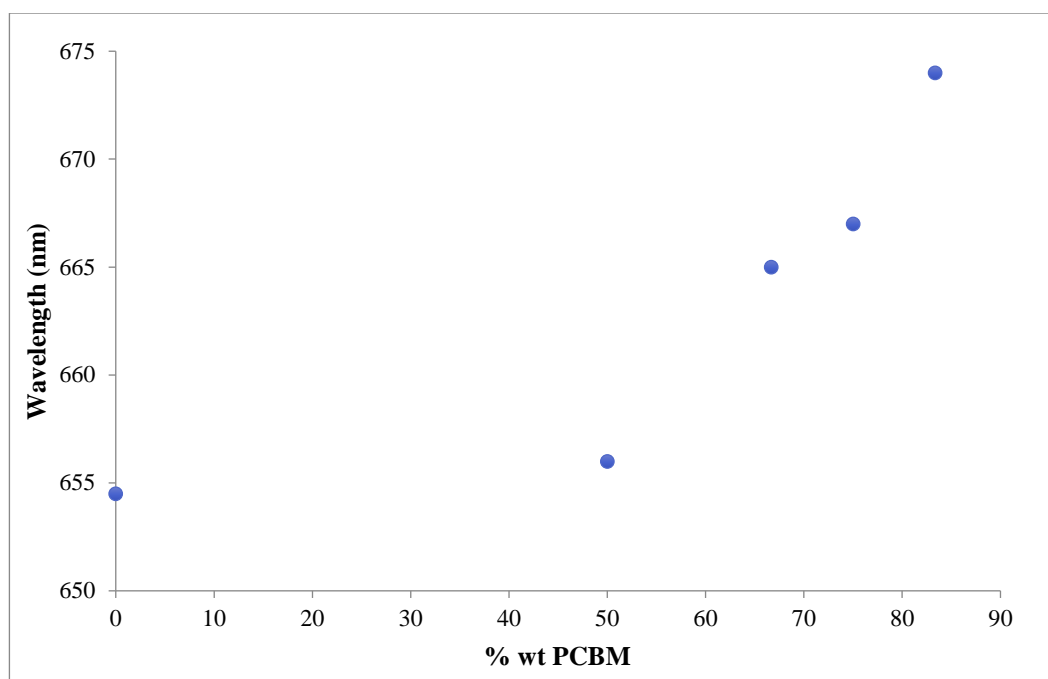
Figure 3.1: a) The change in thin film absorption spectra normalized to the low energy peak of DHSQ(OH)$_2$:PC$_{61}$BM blend films as a prepared by spin coating chloroform solutions. The black arrow marks the red shifting of this peak as the amount of PC$_{61}$BM is increased (top). b) The wavelength of the low energy peak as a function of the wt% of PCBM (bottom).

Due to this shift, there is uncertainty as to how to assign the low energy peak as it could be the J – aggregate[41], since it is red shifted with respect to the monomer in solution. It could alternatively be the monomer mixed with the intermolecular charge transfer (ICT) peak[14, 42]. The ICT is when an electron is transferred from the donor of one SQ molecule to the acceptor of its neighboring SQ molecule[14, 42]. This chapter attempts to confirm and explain these assignments by using poly-(methyl methacrylate) (PMMA) as an inert media to make solid solutions for our SQs. It is hypothesized that the low energy peak is the monomer peak mixed with the intermolecular charge transfer as opposed to being the J- aggregate peak. J-aggregates demonstrate significant fluorescence[3] but we see no such fluorescence from these film so we reject this possibility.
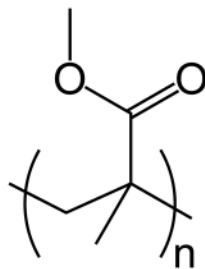
Figure 3.2: Chemical structure of PMMA polymer

PMMA (Figure 3.2) is a transparent thermoplastic polymer. The main purpose of using PMMA is that it allows us to use 10^5 to 10^6 times higher SQ concentration than in solution. When we spin cast neat SQ films, the chloroform evaporates and the SQ molecules are forced closer to each other and completely aggregate. Therefore, by adding PMMA, it can lock the SQ molecules in intermediate positions between solution and the neat solid phase. This means the SQ molecules cannot self-aggregate as they are frozen in the glass. Therefore, at low concentration of SQ, we can obtain SQ monomers in PMMA solid solution, and as we vary the SQ/PMMA ratio, it allows us to further study how the populations change from predominantly monomer at low concentration to a majority of aggregates at high concentration of SQs. This study will also help understand the assignment of the absorbance peak as well as it can give us information on the intermolecular distances in "monomer" compared to "aggregate" samples by looking at how the absorbance spectrum changes as we vary SQ/PMMA ratio. The advantages of using PMMA is that, 1) it is a transparent polymer so it does not absorb in the UV-Vis spectrum and therefore it will not interfere with absorption spectra of SQ; 2) PMMA can be dissolved easily in chloroform with the SQ; and 3) PMMA is assumed not to interact with or quench the SQ molecules; 4) films with low SQ concentration are annealed at the melting point of PMMA polymer, the polymer will 'soften' and will allow the SQ to aggregate.

37

Therefore, annealing study will give us the opportunity to study the monomer to aggregate population change by understanding how the absorption spectra change.

3.2 Experimental

Stock solutions of poly-(methyl methacrylate) (PMMA) and DHSQ(OH)$_2$ in chloroform were made in pre-cleaned vials. The concentration of PMMA stock was 40 mg/ml and the concentration of DHSQ(OH)$_2$ was 2 mg/ml. Once chloroform was added, the PMMA stock was parafilmed and heated at 40°C for 20 minutes to fully dissolve the polymer. Certain amounts of DHSQ(OH)$_2$ and PMMA stock were added to pre-cleaned vials, to make different concentrations. The concentration of DHSQ(OH)$_2$ in solid solution refers to the weight ratio of DHSQ(OH)$_2$/PMMA. The concentration of PMMA in chloroform was fixed at 40 mg/mL, while the concentration of SQ was varied for different weight ratio (Table 3.1). The films were spin coated using a spin speed of 3000 rpm for 45 seconds. The films were kept in plastic film holders. An annealing treatment was applied to the SQ-PMMA films. The annealing was conducted at 155°C (5°C below the melting point of PMMA).

A Shimadzu UV-2401 spectrophotometer was used for absorption characterization. A medium scan speed, 0.5 nm increments and a 2 nm slit width were applied when taking the measurements. Absorbance of the slides was then recorded from a wavelength of 300 nm to 900 nm. A blank glass slide was used to baseline the spectrum to account for scattering and absorption of substrates. Three measurements were taken for each film by changing the film position in the light path to account for any heterogeneity in the films.

Table 3.1: Concentration of PMMA and DHSQ(OH)$_2$ in solid state films

Mass of PMMA (mg)	Mass of SQ (mg)	%wt SQ
20	1.0	4.76%
20	1.5	6.98%
20	3.0	13.04%
20	4.0	16.67%
20	5.0	20.00%
20	5.5	21.57%
20	6.0	23.08%
20	7.0	25.93%
20	8.0	28.57%
20	9.0	31.03%
20	10.0	33.33%

3.3 Results and Discussion

3.3.1 SQ in PMMA solid solution
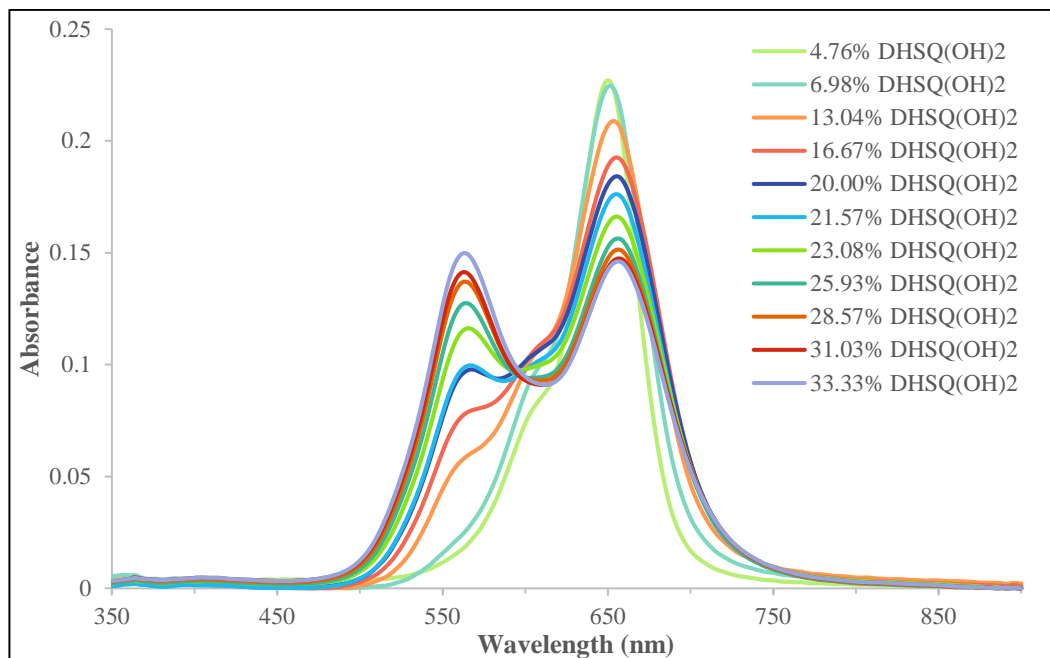
Figure 3.3: Absorbance as a function of wavelength as the %wt of DHSQ(OH)₂ is
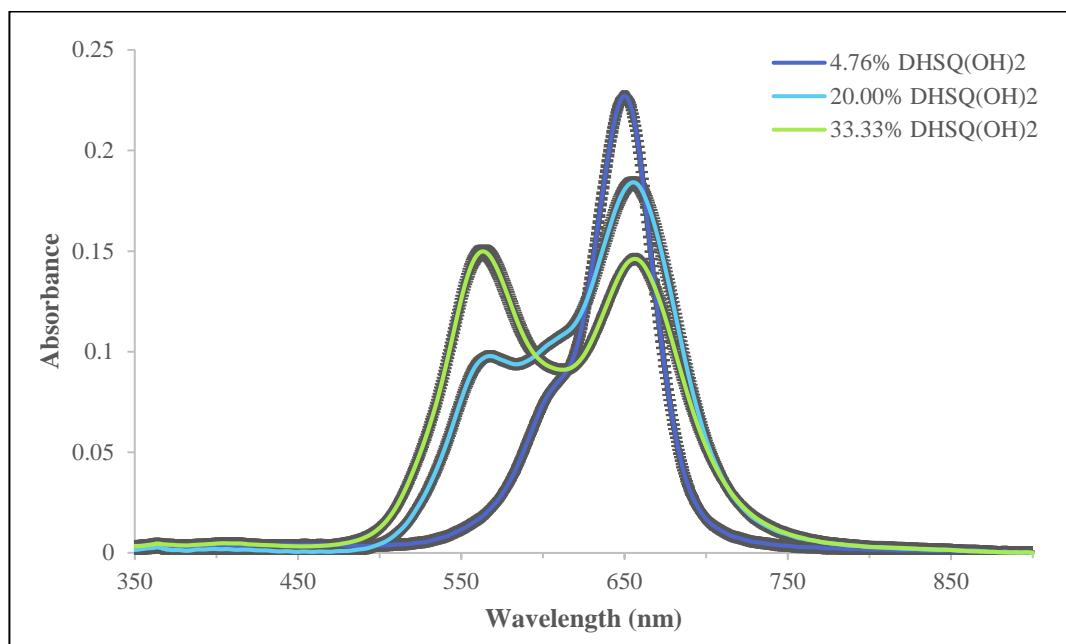
increased in PMMA

Figure 3.4: Absorbance as a function of wavelength as the %wt of DHSQ(OH)₂ is

increased in PMMA. Showing the standard deviation along the spectrum. The standard
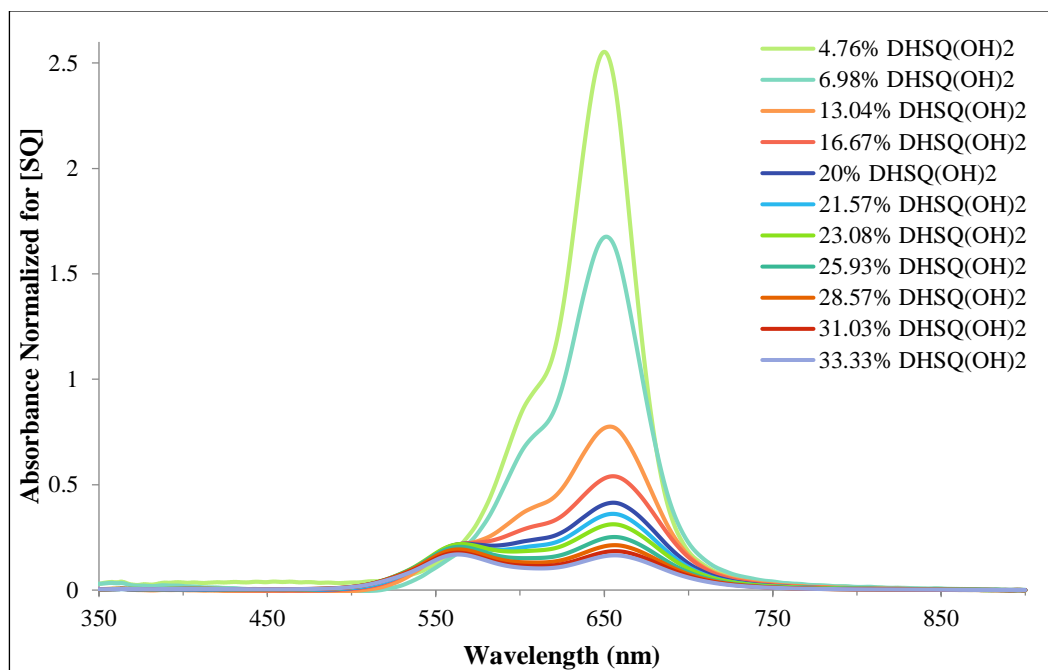
Figure 3.5: Spectra normalized for concentration of SQ in the PMMA film, assuming film thickness is the same for each film because PMMA weight percent in spin casting solution is held constant.

To investigate if the low energy peak is the monomer and intermolecular charge transfer peak, DHSQ(OH)$_2$ was co-dissolved with an inert polymer PMMA in chloroform at different wt% of SQ. It is assumed that the SQ molecules will orientate themselves randomly so long as the spin coating process is fast and the phase separation is slow. As the concentration of SQ is increased there is a change in the spectrum from a single hump spectrum with a peak at 645 nm and a slight shoulder at 600 nm at 4.76 wt% of DHSQ(OH)$_2$ into the double hump spectrum with peaks at 651 nm and a peak at 563 nm at 33.33 wt% of DHSQ(OH)2 as seen in Figure 3.3. Note that there is also a slight red shift in the low energy peak which can be better seen in the normalized absorption data (Figure 3.6). The lower energy peak is either the monomer or the ICT state but not both. There can be two peaks that overlap, however, that gives the appearance of a single peak.

41
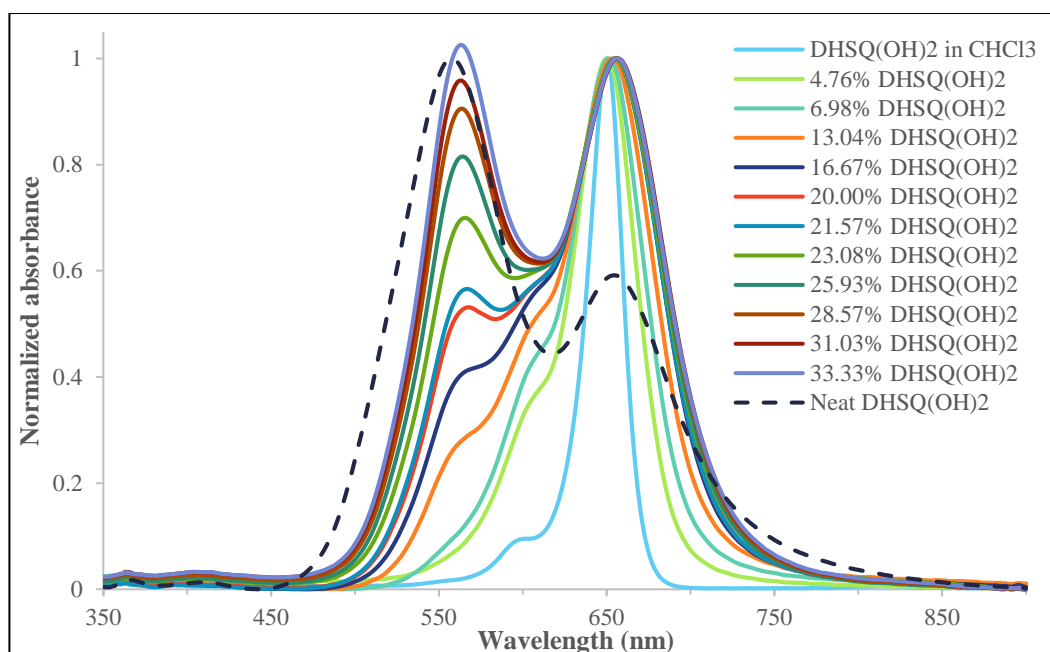
Figure 3.6: Normalized absorption spectra of DHSQ(OH)$_2$ in PMMA solid solution (normalized to the low energy peak) with comparison to DHSQ(OH)$_2$ in chloroform solution and neat thin film spectra

Normalized absorption spectra of DHSQ(OH)$_2$ in PMMA solid solution are shown in Figure 3.6 along with spectra of DHSQ(OH)$_2$ in chloroform solution and as a neat thin film, for comparison. As seen in Figure 3.6, at low concentration of SQ (4.76% DHSQ(OH)$_2$) the low energy peak is exactly where the monomer peak is in solution at a wavelength of 650 nm. As the concentration is increased, it gives rise to the higher energy peak at the wavelength of 563 nm, compared to the H aggregate peak at the wavelength of 557 nm in the neat DHSQ(OH)$_2$ spectra. At SQ concentrations of 4.76%, 6.98%, 13.04% and 16.67% there seems to be a slight shoulder at 600 nm, which becomes hidden by the larger blue shifted feature as the concentration is increased. There is a slight red shift in the low energy peak, as you increase the concentration of DHSQ(OH)$_2$ (Figure 3.7). In Figure 3.7 shows the red shift in the wavelength of the low energy peak as the concentration of SQ is increased. Although in Figure 3.1, the low energy peak red shifts when SQ

42

concentration decreases (PCBM % increases), which is opposite to the shift of the lower energy peak seen in PMMA study, as we see a blue shift as SQ concentration is decreased. This is thought to be due to the different dielectric constant of the fullerene environment which causes the lower energy peak in blended films to significant red shift compared to the monomer in chloroform solution[14]. As seen in Figure 3.3, as the concentration of SQ is increased there is a decrease in peak height of the low energy peak, which may indicate a formation of the aggregate peak. This decrease in absorbance intensity may help explain the red shifting seen in the low energy peak in Figure 3.7.
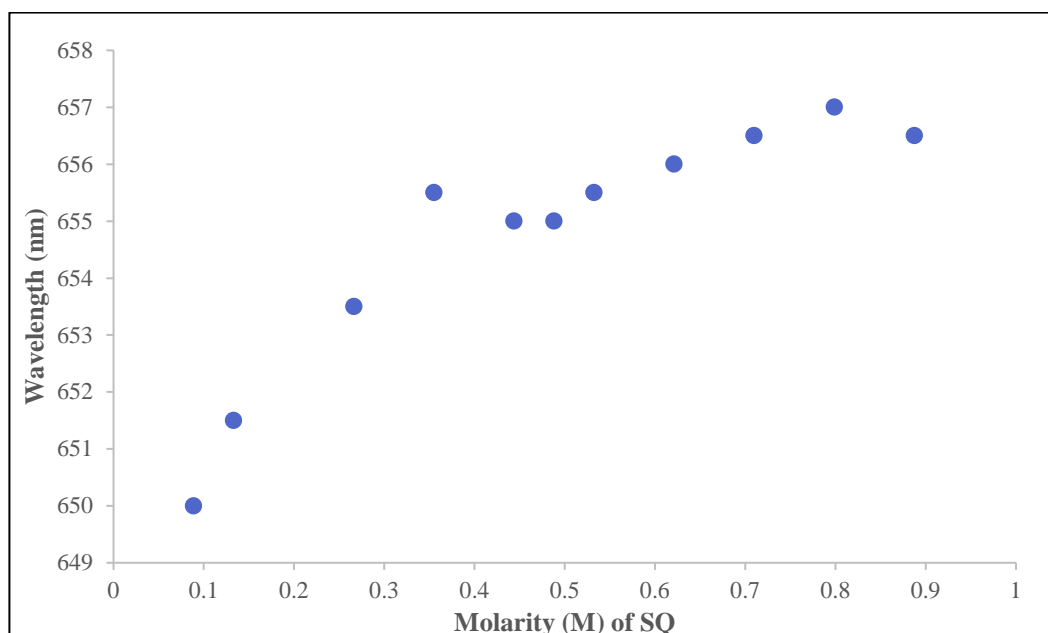
Figure 3.7: Shows the shift in the wavelength of the low energy peak as the concentration increases

The intermolecular distance calculation is based on the concentration of SQ at each %wt of SQ. To estimate this the volume (V) of the SQ molecule in solid solution needs to be known along with the Avogadro's number (N_A) and the Molarity (M) of the SQ in the thin film; given by Equation 3.1

$$l = \sqrt[3]{v} = \sqrt[3]{\frac{V}{N_A M V}} = \sqrt[3]{\frac{1}{N_A M}}$$

<div align="center">Equation 3.1</div>

The Concentration of SQ can be calculated by Equation 3.2, but there are two assumptions; (1) the density of the film is the density of pure PMMA and (2) the volume does not change when SQ is added.

$$M = \frac{mol}{V} = \frac{\%wt \times m/MW}{(1 - \%wt)m/D} = \frac{\%wt \times D}{(1 - \%wt) \times MW}$$

<div align="center">Equation 3.2</div>

where M is the concentration of SQ in the thin film solution, mol is the number of moles of SQ, %wt is the % weight of SQ compared to PMMA, MW is the molecular weight of SQ, m is the mass of the thin film and D is the density of PMMA. As mentioned above, this method used the assumption that the density of the film depends on PMMA and therefore constant. Therefore, at low concentrations of SQ (%wt < 15%), the errors are estimated to be less than 5%. But at high concentrations of SQ (%wt >50%), the errors are estimated to be large <50%.

At low concentration of SQ, there is a high absorbance of the low energy peak and the intermolecular distance are larger, but at high concentration of SQ, there is high absorbance of the high energy peak and the intermolecular distance decreases as seen in Figure 3.8. The estimated distance between molecules is 2.65 nm at 4.76% SQ by weight and 1.23 nm at 33.33% SQ by weight, with corresponding molarities of 0.09 mol/L and 0.89 mol/L. This would make sense as when SQ molecules aggregate the molecules are packed in a more ordered form, therefore the molecules are packed closer together. Therefore, this means that at low concentration of SQ, we are seeing

SQ monomers and as the concentration is increased the SQ molecules are
aggregating.
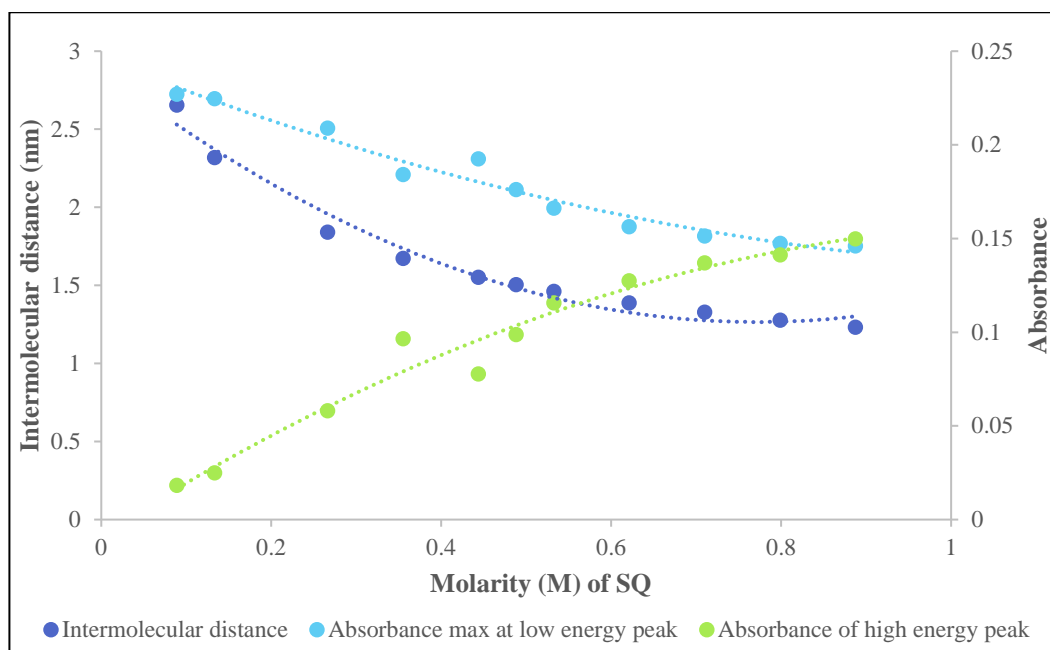
**Figure 3.8: Absorbance of the low energy peak (light blue), high energy peak (green)
and intermolecular distance (dark blue) as a function of Molarity**

3.3.2 Annealing SQ-PMMA solid solution
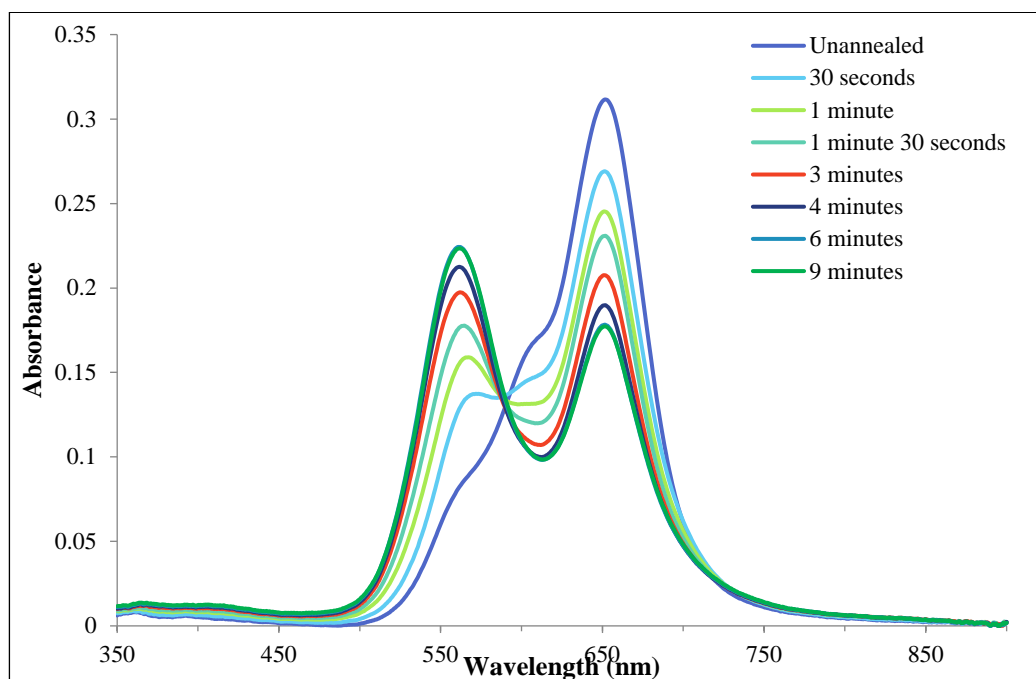
Figure 3.9: Absorption spectra of DHSQ(OH)$_2$ in PMMA solid solution (13.04% by weight) with a range of annealing times

SQ:PMMA blended films were annealed at 155°C (just below the melting point of PMMA) for a range of annealing times for the 13.04 wt% of SQ film (Figure 3.9). This was done to monitor the aggregate formation process. As seen from Figure 3.9 at 30 seconds (light blue) the absorbance peak at 650 nm decreased and there was an increase in absorbance at 570 nm with a decrease in shoulder height at ~600 nm. After 1 min (light green) the peak at 650 nm continues to decrease and the shoulder at 600 nm disappears. There is an increase in absorbance at 550 nm. After 3 minutes (red) of annealing there was an increase in the peak at 550 nm (high energy peak) and a decrease in the low energy peak at 650 nm. After 4 minutes (navy) of annealing the low energy peak continues to decrease and the high energy peak continues to increase. At 6 minutes (blue, this spectrum is buried under the 9 minutes spectrum) there was a further increase in the absorbance peak for the high energy peak and a decreasing of the low energy peak. Further annealing this film to 9 minutes (green),

46

there was little to no change to the spectrum compared to the spectrum at 6 minutes, indicating that there is very little impact on the phase separation after 6 minutes of annealing. The change in the relative peak height can be seen in Figure 3.10 as a function of annealing time. From Figure 3.10, it can be seen that as annealing time is increased, the relative peak height for the low energy peak decreases at the same time as there is an increase in the relative peak height of the high energy peak. This result is consistent with SQ molecules are going from the monomer (low energy peak) directly in to more ordered H aggregates.
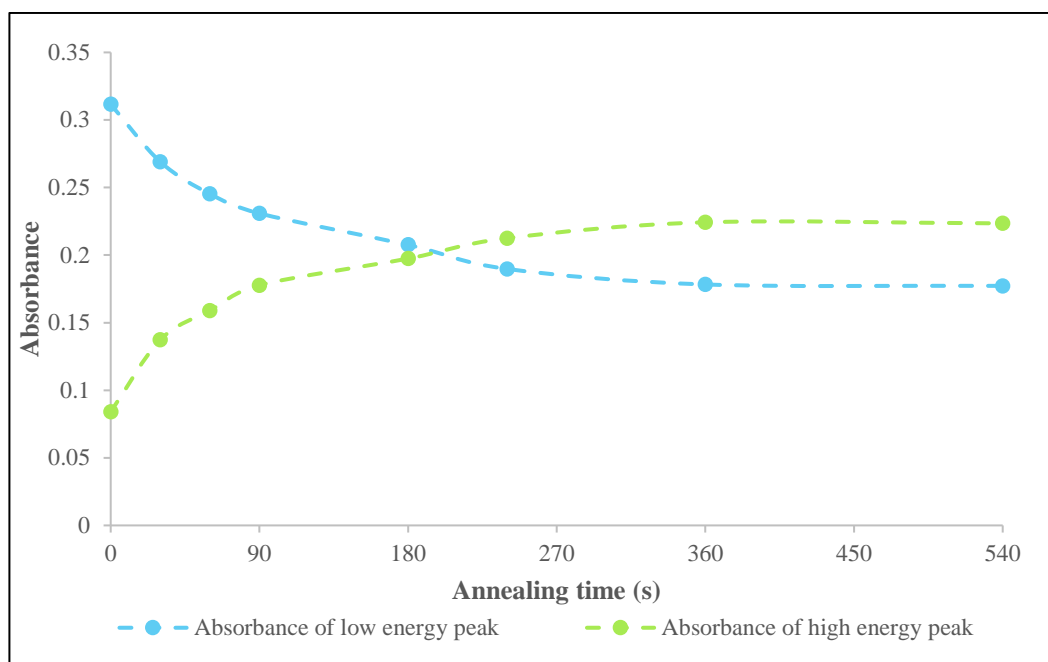
Figure 3.10: Absorbance of the low energy peak (light blue), high energy peak (green) and as a function of annealing time at 155°C

There is one isobestic point seen at 596 nm, as the spectra changed. This indicates the two species are stoichiometrically related[13]. Figure 3.11 shows the shift in the wavelength of the low energy peak (light blue) and high energy peak (green) as annealing time is increased. It can be seen there the low energy peak doesn't really shift as annealing time is increased. Therefore, in this case it is a transformation of the

47

monomer to the aggregate. This will also support the assignment that the peak at ~650 nm is the monomer peak mixed with the intermolecular charge transfer peak.
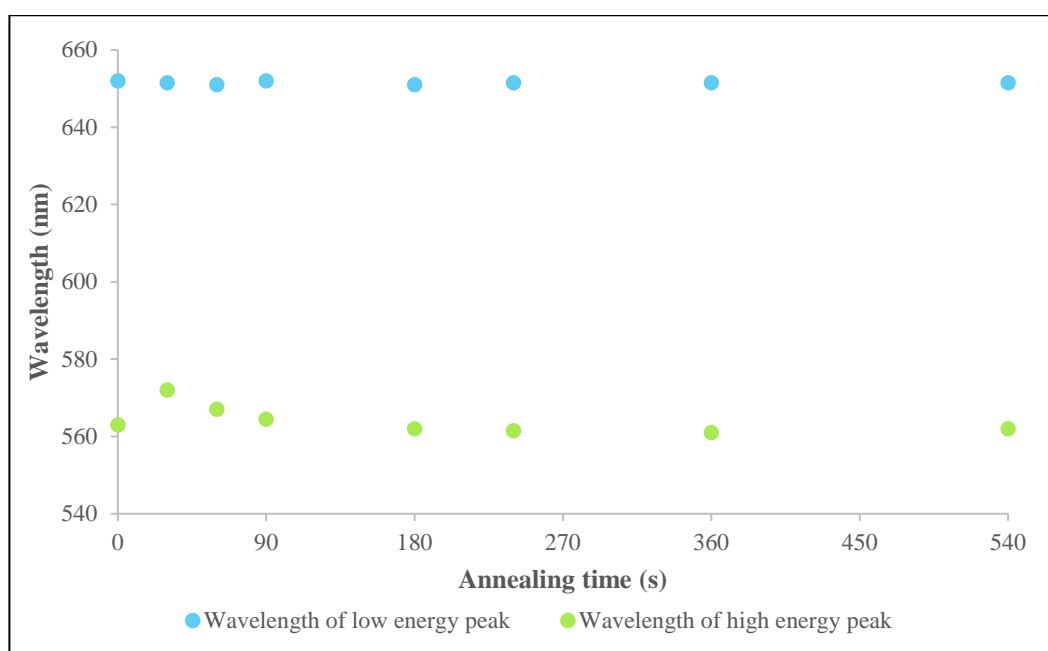
Figure 3.11: Shows the shift in the wavelength of the low energy peak (light blue) and high energy peak (green) as a function of annealing time

3.4 Conclusion

From the PMMA – SQ study, we have studied the transformation of SQ monomer at low concentration of SQ to the SQ molecule aggregate at high concentrations through absorption spectra. We have successfully been able to use PMMA to 'freeze' the SQ molecule in the monomer form at low concentration. From the annealing study, we have monitored the transition of SQ from monomer to aggregate.

In PMMA solid state study, we assume that at low concentration of SQ, there are only monomer present in the as-cast PMMA films. We have little phase separation without annealing. Whereas as the concentration of SQ is increased, the molecules are forced closer together, but all the molecules are expected to pack randomly in the as

cast films. From Figure 3.7, we can see there is a red shift in the low energy peak as the concentration is increased.

As the SQ aggregates the intermolecular distance reduces from is 2.65 nm at 4.76% SQ by weight to 1.87 nm at 33.33% SQ by weight. This indicates that as the concertation of SQ is increased the SQ molecules are brought closer together and the result is an increase of the high energy aggregate peak. In Figure 3.8, we can see that as the concentration of SQ is increased, the intermolecular distance between two molecules and the absorbance intensity of the low energy peak is decreased and the absorbance intensity of the high energy peak is increased.

When these films are annealed, we have seen how the spectrum changes from monomer to aggregate. With annealing, there would be more phase separation. We might expect "crystal – like" nanoparticles to form. Annealing should show the conversion of either 1) monomer to aggregate at low concentration of SQ (Figure 3.12a), or 2) conversion of random "agglomerates" into crystal – like aggregates (Figure 3.12b). There is one isobestic point seen at 596 nm (Figure 3.9), as the spectra changed. This indicates the decrease of one species to the other species. As well, from Figure 3.11, it can be seen that the low energy peak doesn't really shift as annealing time is increased. Therefore, in this case it is a transformation of the monomer to the aggregate. This will also support the assignment that the peak at 650 nm is the monomer peak mixed with the intermolecular charge transfer peak.

Figure 3.12: Illustration of morphology showing the conversion of a) monomer to aggregate and b) random "agglomerates" into crystal – like aggregates upon annealing

We assign the peak at 650 nm to be the absorption from a monomer species. We assign the peak at 560 nm and 660 nm to be from the aggregate, which includes a lower energy ICT (2nd hump) contribution (Figure 3.13[14]). Our data supports there being two species in solid solution; monomer and aggregate. We can control the population of these two species by changing annealing conditions.

Figure 3.13: Diagram of the coupling of the ICT state with the H aggregate state and of DHSQ(OH)₂ aggregates 'double hump' absorption spectra shape

This data supports our hypothesis of out assignment that there is an ICT peak absorbance intensity increases and causes the peak to red shift as the H – aggregate peak is formed. Note that when the films are blends with PCBM (Figure 3.1), the low

energy peak blue shifts as more aggregates are formed. This is due to the different dielectric constant of the fullerene environment, which causes the monomer peak to be red shifted compared to the monomer peak in solution[14]. We have seen in Figure 3.1, that spectrum changes based on the blend ratio of the blended SQ film. In the next chapter, we will investigate and how these spectral changes affect the efficiency of our devices.

Chapter 4 : Blend Ratio Studies of DHSQ(OH)$_2$:PCBM Devices

4.1 Introduction

With our understanding of how to assign the squaraine aggregates, we now turn our attention to blended films using PCBM instead of PMMA. In this section, we are going to understand how the spectrum changes based on the blend ratio of the blended SQ film and how it affects the efficiency of our devices. Within the active layer in OPV devices, the aggregation can be controlled by changing the blend ratio of DHSQ(OH)$_2$:PCBM[41]. Crystallinity can also be changed for these active layers; crystallinity is linked to aggregation, as a more ordered packing of aggregate give rise to crystallinity (Figure 3.12b). Crystallinity is tied to the efficiency of the OPV device. As crystallinity increases, there will be an increase in the charge mobility. In this study, we are going to be looking at DHSQ(OH)$_2$; this SQ can aggregate in the H-aggregate motif, as it results in an absorption spectrum that is blue shifted compared to the DHSQ(OH)$_2$ spectra in chloroform solution (Figure 1.14). As seen in chapter 3, PMMA was used to disrupt the aggregation of SQ molecules. Therefore, in this chapter we will be using PCBM instead of PMMA to disrupt the aggregation of SQ molecules. It is important to note that when too much PCBM is added, there may be an island of SQ molecules formed that does not allow the charges to flow out, which results in them recombining.

To optimize the efficiency of SQ devices, there needs to be an increase in the number of photons absorbed, and since the photon flux is higher in the NIR region (Figure 1.6[21]), there will therefore be a larger absorbance when dyes are designed to

absorb here. If the number of photons absorbed by the material are increased, the number of resulting excited states that are converted into dissociated charges are increased, which then subsequently increases the short circuit current (J_{SC}). We know that when DHSQ(OH)$_2$ aggregates, the absorbance spectrum blue shifts from that of the monomer, therefore if we have more aggregates in our active layer, the PCE of our deceives should decrease as we are losing the NIR absorption. The J_{SC} is proportional to the integrated area underneath the photon flux (Figure 1.6) assuming an external quantum efficiency of 100% across the absorption spectrum[43]. Therefore, the J_{SC} can be predicted by the product of the absorbance spectrum and the photon flux to calculate the number of photons that are absorbed to generate current.
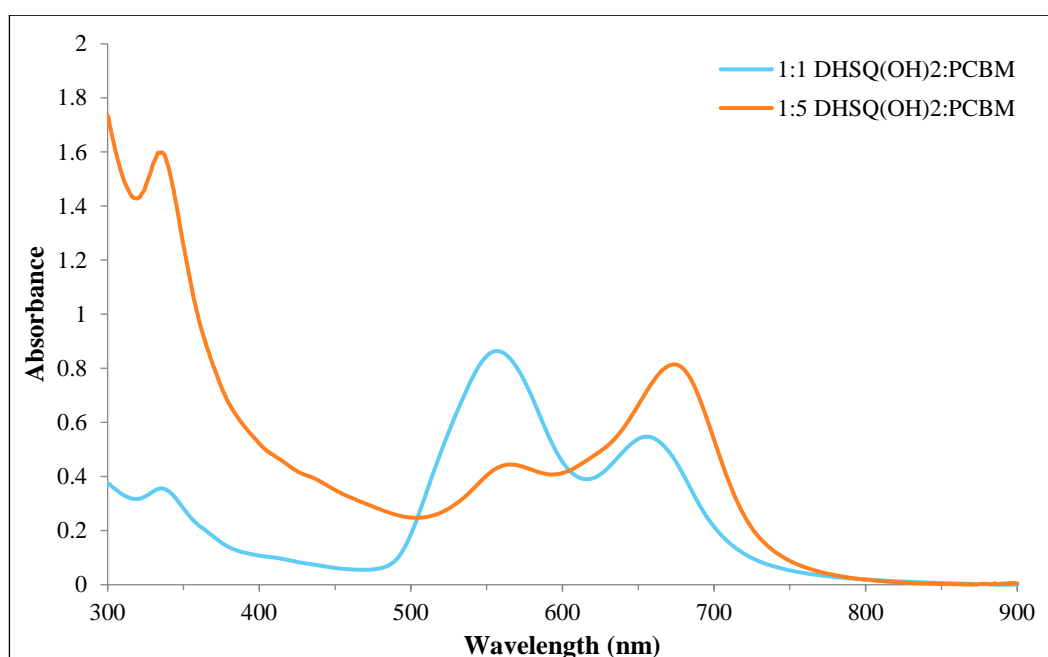
Figure 4.1: Absorbance spectra from spin-coated films of blends of DHSQ(OH)$_2$:PC$_{61}$BM in various mixing ratios as noted on the graph

As seen in Figure 4.1, by changing the blend ratio there is a change in the spectrum. It can be seen that as the concentration of PCBM is increased, there is a higher absorption in the NIR region of the spectrum. Therefore, the theoretical J_{SC} for the spectrum with the blue shifted aggregate (blue) is 14.704 mAcm^{-2} and the

theoretical J_{SC} for the spectrum with monomer (orange) is 15.097 mAcm^{-2} (look at appendix for calculations). It can be seen that although there is a broadening of the spectrum with the blue shifted H- aggregate, the J_{SC} does increase when there is more monomer compared to H-aggregate. Note that the absorbance due to PCBM is also take into account.

The absorption is also affected by the active layer thickness (Equation 4.1). In Equation 4.1, A is the absorbance, α is the absorption extinction coefficient of the material in thin films and d is the thickness of the active layer.

$$A = \alpha \times d$$

<div align="center">**Equation 4.1**</div>

Phase separation in the BHJ is another factor that will affect the PCE of our devices. As we disrupt the aggregation of SQ molecules, it will reduce phase separation in the active layer and therefore affect the charge collection and mobility of charges[39]. Therefore, in this chapter we will understand disruption of aggregation of SQ molecule affect device efficiency. We hypothesize that a disruption of aggregation of SQ molecule would improve device efficiency as there is an increase in absorption in the NIR region.

4.2 Experimental

UV-Vis absorbance

For UV-Vis absorbance measurements, thin film samples were prepared by spin casting the active layer (800 rpm for 18 seconds) from blended SQ chloroform solutions (the same as for device preparation) onto glass substrates cut from microscope slides. A Shimadzu UV-2401 spectrophotometer was used for absorption

characterization. Settings of medium scan speed, 0.5 nm increments and a 2 nm slit width were applied when taking the measurements. Absorbance of these samples was then recorded from a wavelength of 300 nm to 900 nm. A blank glass slide was used to baseline the spectrum to account for scattering and absorption of substrates. Three measurements were taken for each film by changing the film position in the light path to account for any heterogeneity in the films.

Device Fabrication

Eight pieces of precut Indium-tin-oxide (ITO) coated glass were used. The substrates were cleaned using acetone and IPA under sonication conditions. A corner of each substrate was taped to protect the ITO - anode. They were left in the vacuum oven (150°C) for an hour prior to spin-coating with a 1:1 ratio of PEDOT: PSS to deionized water, at a spin speed of 5000 rpm for 40 seconds. They were then left in the vacuum oven for 15 minutes. They were then transferred into a nitrogen-filled glove box system. The active solar cell layer was spin-coated (800 rpm for 18 seconds for 1:1, 1:2 and 1:3; 400rpm for 18 seconds for 1:5) from chloroform solutions containing 8 mg/mL $DHSQ(OH)_2$ for blend ratios 1:1, 1:2 and 1:3 or 4 mg/mL $DHSQ(OH)_2$ for the blend ratio 1:5. The precise masses used are shown in Table 4.1. They were then transferred directly into high vacuum and aluminum electrodes were thermally evaporated through a shadow mask giving four solar cells on each substrate, with an area of approximately ~29 mm^2 for every sample.

Table 4.1: Active layer masses and concentrations

Ratio (SQ: PCBM)	Mass of SQ (mg)	Mass of PCBM (mg)	Total Vol of Chloroform (mL)	Conc of SQ (mg/mL)	Spin speed used (rpm)
1:2	5.8	11.6	0.7	8	800
1:3	4	12	0.5	8	800
1:5	2.8	13.9	0.7	4	400

J-V measurement

The J-V measurements were performed using a Newport solar simulator with a power density of 100 mW cm^{-2} (1-sun illumination). The OPV devices were tested immediately after fabrication by a four-point probe method. The out bias was scanned from -2 Volts to 2 Volts with a 0.4 Volts increment. The current density of the OPV devices (under 1-sun illumination) was measured, and the J-V curve was obtained by measuring the current signal as a function of the voltage bias. The short-circuit current (J_{SC}), open-circuit voltage (V_{OC}) and fill factor (FF) were calculated by inserting the data into a calculating spreadsheet.

4.3 Results and Discussion

4.3.1 UV-Vis Absorbance
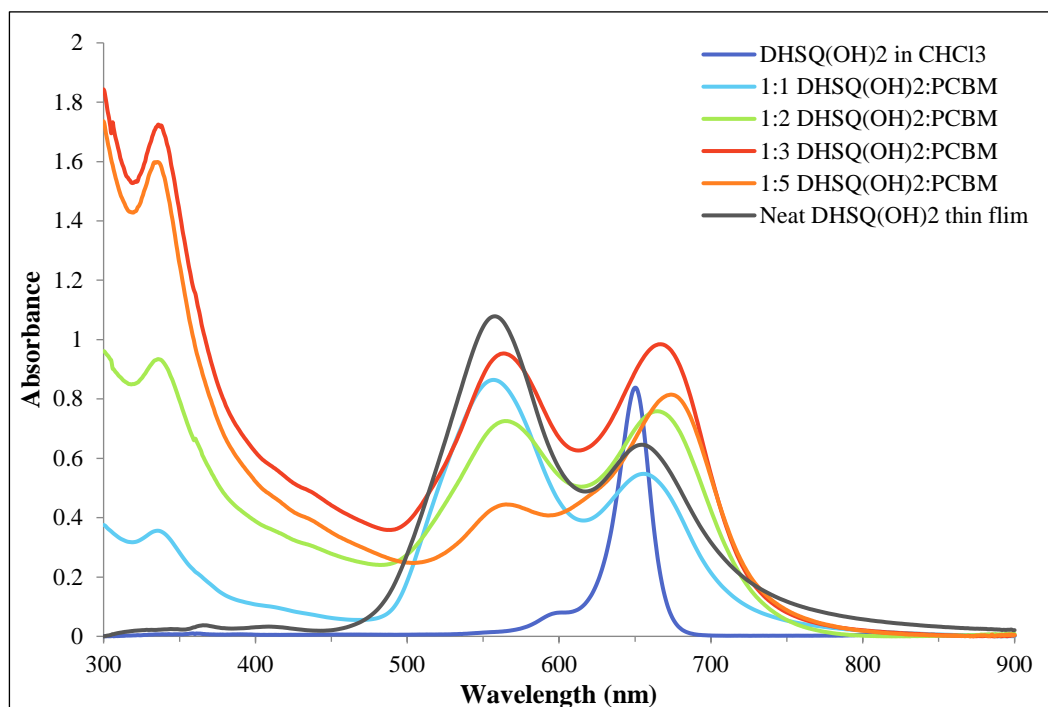
Figure 4.2: Absorbance spectra from spin-coated films of blends of DHSQ(OH)$_2$:PC$_{61}$BM in various mixing ratios as noted on the graph

Absorbance was measured for films that were spin-coated on glass from the same chloroform solution as used for solar cell preparation. All UV-Vis absorption spectra are plotted in Figure 4.2. Figure 4.2 shows the absorbance of DHSQ(OH)$_2$: PCBM blend ratio films as a function of wavelength. The peak at 320 nm in the blend ratio films is the absorbance of PC$_{61}$BM, which was chosen because as seen (Figure 4.3), the overlap is minimized, when compared to other fullerenes such as PC$_{71}$BM.
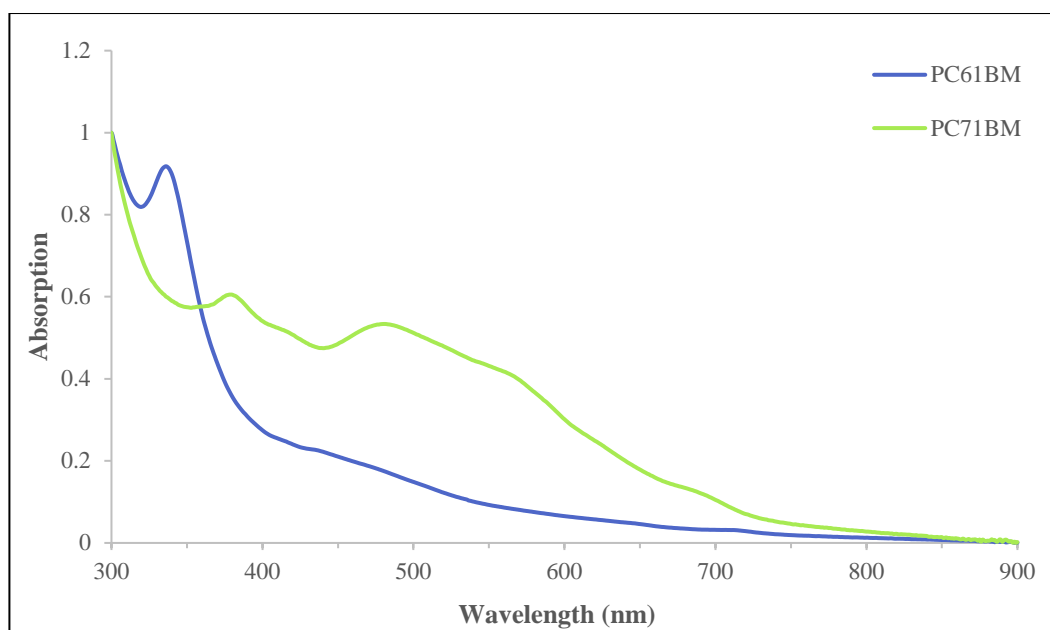
Figure 4.3: Absorbance spectra of spin-coated films of PC$_{61}$BM and PC$_{71}$BM

The neat DHSQ(OH)$_2$ in CHCl$_3$ solution (blue) is provided in addition to the film data and shows only one peak at 646 nm, assigned as the monomer peak. The blend ratio films compared to the neat films have very different spectra. It is seen that PCBM causes a big change in the spectra due to the notion that aggregation is disrupted. The blend ratios studied are 1:1 (light blue), 1:2 (light green), 1:3 (red) and 1:5 (orange), and in general, all these spectra show two absorbance maxima, resembling an H- aggregate peak (560 nm) and a monomer peak mixed with the intermolecular charge transfer peak (660 nm). Note that the low energy peak red shifts as the concentration of PCBM is increased (Figure 4.4). As said in chapter 3 this is due to the mixing of the ICT peak with the monomer peak.
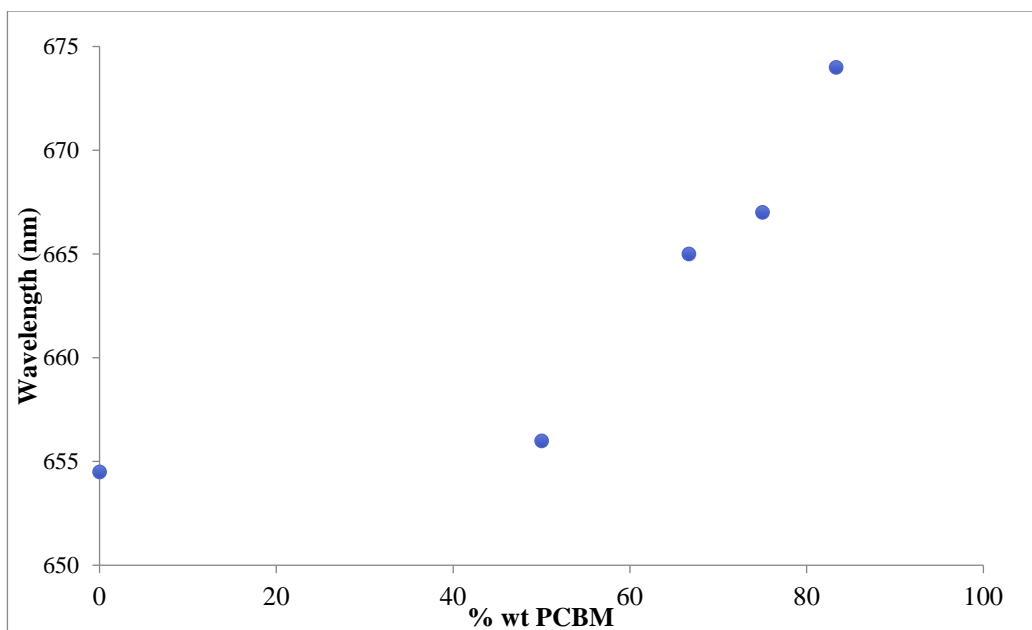
Figure 4.4: The wavelength of the low energy peak as a function of the wt% of PCBM

In Figure 4.2, the neat DHSQ(OH)$_2$ (grey) two maxima are observed, with an

H – aggregate peak at 556 nm, blue shifted from the monomer peak in solution (blue).

The low energy peak at 656 nm, which is slightly red shifted from the monomer peak,

is assigned to the intermolecular charge transfer peak which couples to the H-

aggregate peak in the thin films[14]. When introducing PCBM, (Figure 4.2) the blend

ratio 1:1 (light blue) shows a slight decrease in the intensity of the absorbance spectra;

there are still two maxima with the H- aggregate peak at 556 nm peak, and a second

peak at 656 nm, which may have both monomer and ICT contribution. For the 1:2

blend ratio (light green), both the peaks are further red shifted compared to the 1:1

blend ratio. There is a significant relative increase in the absorbance of the low energy

peak at 659 nm compared to the high energy peak. This trend of reduced relative

contribution of the H-aggregate and increased relative contribution of the lower

energy peak continues in the DHSQ(OH)$_2$ in films, through blend ratios 1:3 (red) and

to a large extent, in 1:5 (orange). This might be explained by a disruption of any

ordered packing structure and squaraine aggregation as PCBM is added. In addition,

as more PCBM is added the low energy peak red shifts, from 675 nm in the 1:1 blend to 659 nm in the 1:2 blend, to 660 nm in the 1:3 blend and finally 669 nm in 1:5 blend, which is consistent with an interpretation that PCBM increases a more significant contribution of monomer peak over that of the ICT peak. This similar trend of the absorption spectra was also seen by Bruck *et al.*, but it is important to keep in mind that our assignments are different; Bruck *et al.* assign the low energy peak to a red shifted J-aggregate[41]. We assign this peak to the ICT hump from the aggregate mixed with the monomer peak[14].
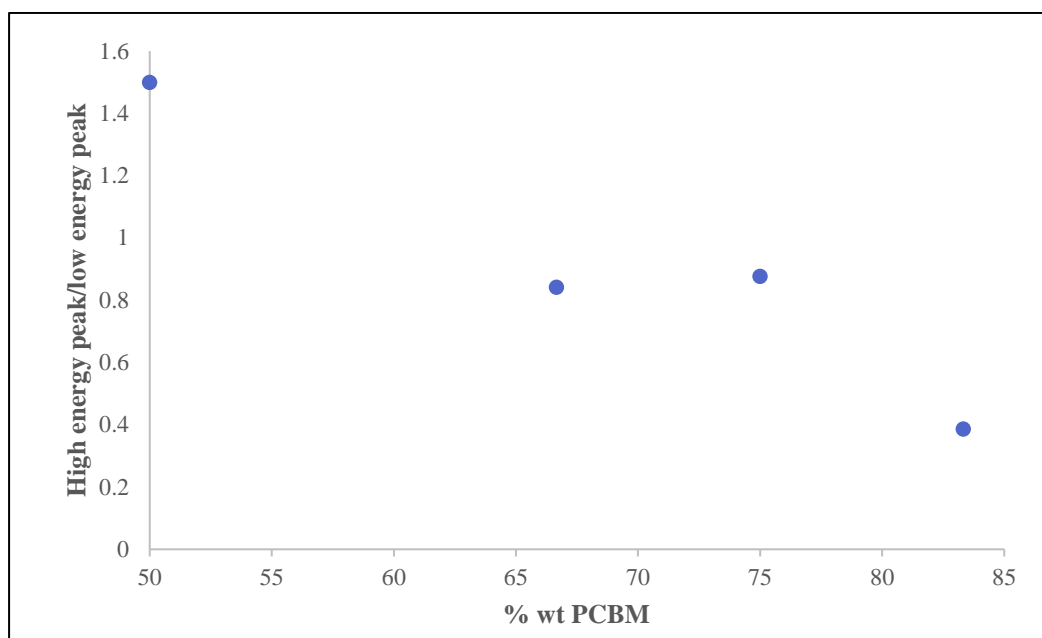
Figure 4.5: The Ratio of the high energy peak to low energy peak against wt% of PCBM

The ratio of high energy peak to low energy peak is dependent on the mixing ratio of DHSQ(OH)$_2$:PCBM (Figure 4.5). As seen from Figure 4.5, with more PCBM the ratio between the high energy peak/low energy peak decreases, therefore meaning with more PCBM, the monomer becomes more distinct, while the H- peak is reduced, as seen in blend ratio 1:5. The theoretical J_{SC} can be calculated by the product of the absorbance spectra and the photon flux (see appendix for calculations). From Table 4.2, it can be seen that the theoretical J_{SC} does increase from 1:1 blend to 1:3 blend

and then decreases. But it is important to remember that for the 1:5 blend, the concentration of SQ was decreased due to the solubility of PCBM in chloroform, therefore this would decrease the absorption intensity which would lead to a decrease in the J_{SC}. When there is an increase in the J_{SC} we should expect an increase in the PCE of the devices. Therefore, when we add PCBM, we might expect an increase in PCE, at least when the concentration of SQ remains constant.

Table 4.2: Shows the theoretical J_{SC} based on absorbance data

Blend ratio	Theoretical J_{SC} (mAcm^{-2})
1:1	14.704
1:2	16.320
1:3	19.579
1:5	15.097

4.3.2 Device Data

Figure 4.6 shows the J-V curve measurements of DHSQ(OH)$_2$:PCBM blend ratio OPV devices. This shape of the J-V curve demonstrates a successful device (with the best efficiency of 0.86% for blend ratio 1:3 for as-cast devices). It should be noted that these devices are un-optimized (as there is no electron transporting layer, and we use PC$_{61}$BM rather than PC$_{71}$BM). It can be seen that the shunt resistance is low, therefore there is some leakage at the junction of the electrodes, which will have a negative impact on the V_{OC} and the FF[24]. More detailed device parameters are listed in Table 4.3 below.
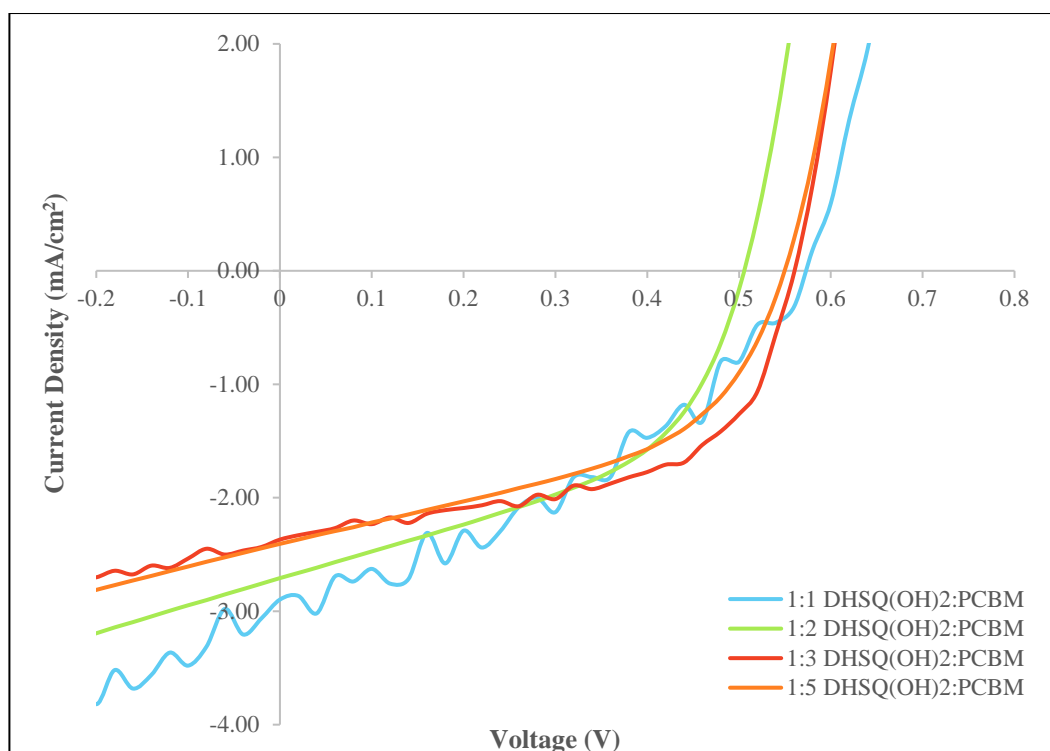
Figure 4.6: Summarized J-V curve measurement for DHSQ(OH)$_2$:PCBM blend ratio study devices

The solar cells had the layer arrangement of

ITO/PEDOT:PSS/DHSQ(OH)$_2$:PC$_{61}$BM/Al.

Table 4.3: Shows the Device data for the different blend ratios. Values and error for PCE, V$_{OC}$, J$_{SC}$ and FF reported here are averages and standard deviation obtained by testing a group of 10 identical films between 2 different batches for each of the systems studied (each film has 4 deceives).

DHSQ(OH)$_2$: PCBM	J$_{SC}$ (mAcm^{-2})	V$_{OC}$ (V)	FF	PCE
1:1	2.94 ± 0.30	0.58 ± 0.01	43.35% ± 4.92%	0.72% ± 0.09%
1:2	2.71 ± 0.15	0.53 ± 0.06	46.32% ± 2.62%	0.66% ± 0.10%
1:3	2.46 ± 0.20	0.57 ± 0.03	61.98% ± 6.60%	0.86% ± 0.13%
1:5	2.39 ± 0.14	0.57 ± 0.04	47.50% ± 3.83%	0.64% ± 0.09%

Table 4.3 shows the device data for the different $DHSQ(OH)_2:PC_{61}BM$ blend ratio devices. The device with blend ratio 1:1 has an average efficiency of 0.72%. For devices with blend ratio 1:2, the efficiency decreases to 0.66%. This drop in efficiency is consistent with a decrease in J_{SC} that decreased significantly from 2.94 mA cm^{-2} to 2.71 mA cm^{-2}. From Table 4.2, it is expected for the J_{SC} to increase as the PCBM concentration is increased. But we see a decrease in the J_{SC} as the PCBM concentration is increased, which was not expected. There is also a slight decrease in V_{OC}, from 0.58 V to 0.53 V. For devices with the blend ratio of 1:3, the V_{OC} recovered back to 0.57 V but there was a drop in the J_{SC} by 0.25 mA cm^{-2}. There was a significant increase in the FF from 46.32% to 61.98%, which resulted in a considerable increase in the average efficiency by 0.20% (from 0.66% to 0.86%). The blend ratio of 1:3 resulted in the highest average efficiency, this data was reproducible between batches. The efficiency of the blend ratio 1:5 devices dropped to 0.64%, with a decrease in both J_{SC} and FF. This could result from using a lower concentration and a lower spin speed when fabricating these devices.

Table 4.4: Device results from Bruck *et al.* Paper[41].

$DHSQ(OH)_2$: PCBM	J_{SC} (mAcm^{-2})	V_{OC} (V)	FF	PCE
1:1	0.46	0.48	32%	0.08%
1:2	2.01	0.79	36%	0.57%
1:3	3.24	0.82	32%	0.84%
1:5	3.74	0.83	30%	0.92%
1:7	2.96	0.72	28%	0.60%

As seen from the Table 4.3 the highest average PCE, 0.86% at a blend ratio of 1:3, was different to the results from the Bruck *et al.* (Table 4.4). A Comparison of the trends found in J_{SC}, V_{OC}, FF and PCE between our data (blue) and Bruck *et al.* (green) are shown in Figure 4.7. Looking at the J_{SC} trend for our data is opposite to the J_{SC} trends to Bruck *et al.* data. The comparison of trends for V_{OC}, FF and PCE between Bruck *et al.* and our data were similar but fill factors are much higher for our data. We cannot explain the discrepancy beyond stating that the processing conditions were different when fabricating the devices.
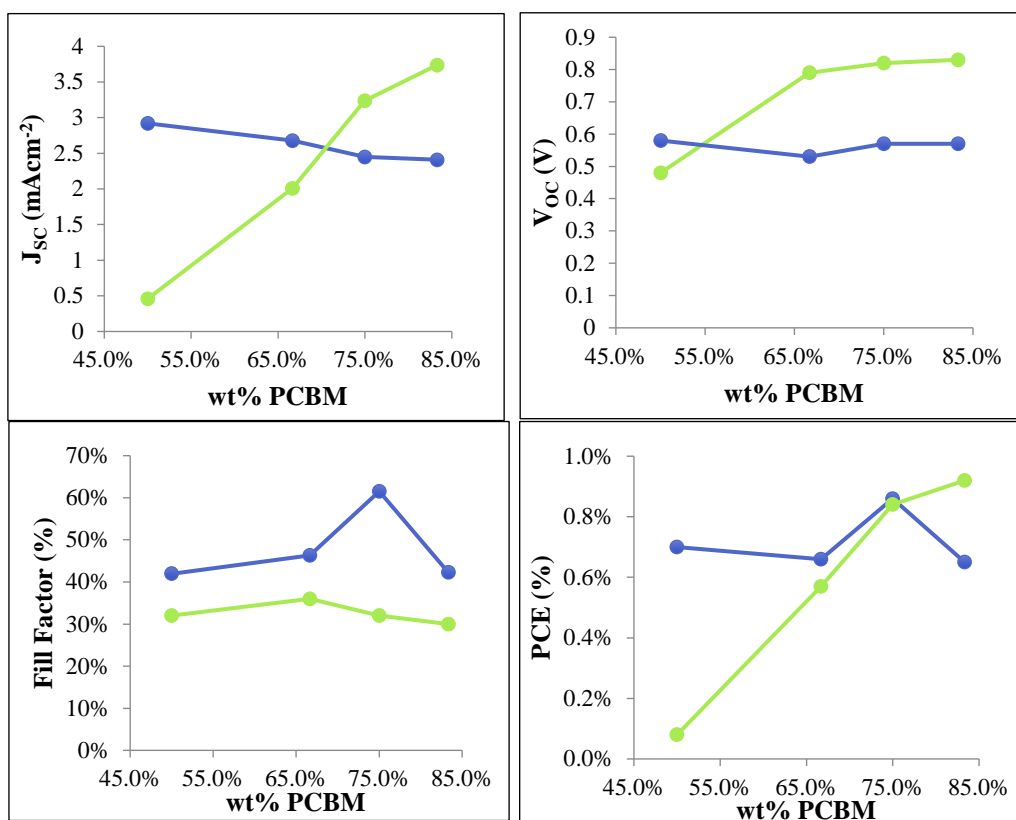
Figure 4.7: Comparison of the trends found in J_{SC}, V_{OC}, FF and PCE between our data (blue) and Bruck *et al.* (green)

Comparing the device results from the Table 4.4 to results in Table 4.3 (Figure 4.7) devices, we do need to keep in mind that the devices in the by Bruck *et al.*, were prepared in chlorobenzene rather than in chloroform, due to strong dewetting[44]. Chlorobenzene has a higher boiling point, therefore Bruck *et al.* annealed the devices

at 50°C in order to evaporate all the solvent. In our results, it can be seen that blend ratio 1:1 devices, which have more H- character, have a higher V_{OC} and J_{SC}. In the Bruck *et al.* result, the 1:5 blend has the highest V_{OC} and J_{SC}, having more monomer, but Bruck *et al.* assign the low energy peak as the J-type aggregate[41]. Bruck *et al.* explain this trend by saying J-type aggregates exhibit a lower lying HOMO level relative to the H-type aggregates which would mean 1:5 blend would have the highest V_{OC}. As the V_{OC} is related to the energy gap between the HOMO of the donor and the LUMO of the acceptor, by decreasing the energy of the HOMO there is an increase in the V_{OC}. On the contrary, in our device results we see that the blend ratio 1:1 has the highest V_{OC} and J_{SC} and we consider there to be more H- aggregate character for the 1:1 blend when compared to the 1:5 blend.

The J_{SC} is related to the generation and collection of the photo-generated carriers. The J_{SC} should increase as PCBM concentration increases as seen by the theoretical calculation (Table 4.2). When there is an increase in intensity of the red shifted low energy peak, more solar photons should be absorbed, thus improving the J_{SC}. When the concentration of the solution is much lower, there is of course trade-off for the efficiency. The trend for J_{SC} in our results is opposite to what was expected.

The trend in J_{SC} could also be due to several reasons. A possible reason could be due to chloroform being used. As I did notice that the films were not uniform. This could be caused due to dewetting that is forming traps in the in the active layer. Therefore, these traps would lead to higher rate of recombination, resulting and a decrease in the J_{SC}. Figure 4.8[14] shows the x-ray diffraction (XRD) pattern for DHSQ(OH)$_2$:PCBM films at different blend ratios and in pristine films. The main diffraction peaks for various blend ratios are located at $2\theta = 5.1$, which corresponds to the (001) plane in the single crystal structure of SQ. As seen in Figure 4.8, as the

concentration of PCBM is increased the peak at $2\boldsymbol{\theta} = 5.1$ decrease. This decrease can be interpreted as a disruption in the crystallinity of the SQ. As 1:1 blend ratio has more crystalline domains (Figure 4.8), than the 1:5 blend ratio and that, as a result, the charges can reach the electrodes more easily. Also, it's an easier way for the charges to get out of the active layer when there is a higher degree of phase separation. In the 1:5 blend ratio, with a lower concentration of SQ, there could be islands formed and therefore the hole would be trapped leading to higher chance of charge recombination[45], this can be tested by looking at TEM images of the active layer (TEM data will be presented in a later chapter). Another reason could be that as the PCBM concentration is increased there is less aggregation of SQ (Figure 4.8), and therefore smaller amorphous domains as there is low concentration of SQ, which will lead to low charge mobility and higher rates of recombination, which will result to lower efficiency. Hole mobility study can be performed to understand the how the mobility is affected with changes to the blend ratios.
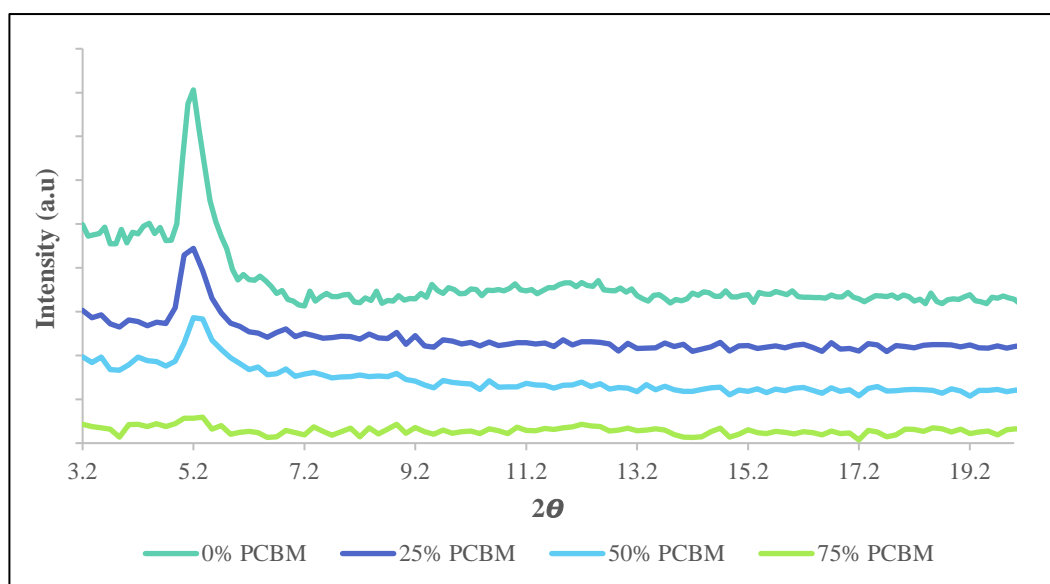
Figure 4.8: X-ray diffraction data recorded for DHSQ(OH)₂:PCBM films at different blend ratios and in pristine films. The main diffraction peaks for various blend ratios

The predicted J_{SC} was modelled in excel by the absorbance data and the

photon flux to calculate the number of photons that would be absorbed to generate

current. As predicted, the calculated J_{SC} goes up based upon the actual absorbance

data of the films made in the same batch of devices that were tested. It is important to

note that when modelling the calculated J_{SC}, it is assumed that the external quantum

efficiency is 100% across the absorption spectrum[43]. This model does not take into

consideration the mobility of charges, extend of crystallinity and recombination

losses. The actual measured J_{SC} goes down as the blend ratio of PCBM is increased.

This indicates that either reduced exciton diffusion[46] to the interface, reduces charge

transfer[47] at the interface, or there is greater charge recombination as blend ratio of

PCBM is increased. As seen from Figure 4.8, there is a disruption of crystallinity at

lower relative concentration of SQ. This would reduce charge mobility in addition to

a reduction in exciton diffusion rate and increased charge recombination rate in the

active layer. At low concentration of SQ, we would assume there would be little

phase separation. Therefore, there would be a more tortuous pathway for charges to

reach the electrodes. This would increase the rate of charge recombination.

Table 4.5: Shows the ratio of J_{SC} for the predicted J_{SC} based on absorbance data

compared with the actual J_{SC}

Blend ratio	Actual J_{SC} as function of ratio (x/1:1)	Predicted J_{SC} as a ratio (x/1:1)
1:1	1 ± 0.14	1
1:2	0.92 ± 0.12	1.11
1:3	0.84 ± 0.13	1.33
1:5	0.81 ± 0.12	1.03

In general, the V_{OC} relates to the HOMO of the SQ and the LUMO of the PCBM. In fact, the H- type aggregates are expected to have a lower V_{OC} because the HOMO energy level of the $DHSQ(OH)_2$ is higher due to aggregation (Figure 1.12).

4.4 Conclusion

We expected that efficiency of our devices would increase upon adding PCBM because as the PCBM concentration is increased, we would expect to see a higher absorption of the SQ monomer peak in the NIR. This would result in more photons absorbed with our increased absorbance/photon flux convolution. By looking at the absorbance data from Figure 4.2, we see that the PCBM is able to disrupt the aggregation completely for $DHSQ(OH)_2$. Therefore, by calculating the theoretical J_{SC} (Table 4.2), it is expected the blend ratio 1:3 would result in the highest PCE. Although it is important to note that this model does not take into account the contribution of the ordered packing.

It is also seen that the blend ratio 1:3 gave a higher efficiency in devices when compared to the blend ratio 1:5, where we saw a disruption of the aggregation. This can be seen as a result of the notable increase in FF from 1:2 to 1:3. The V_{OC} was found to remain the same when the blend ratios were changed, however there was a decrease in the J_{SC}. This decrease in the J_{SC}, is likely to be due to there being a loss of crystallinity as concentration of PCBM is increased (Figure 4.8[14]). At low concentration of SQ, the active layer is made up of smaller amorphous domains which will lead to low charge mobility and higher rates of recombination leading to less charges reaching the electrode resulting in decrease in J_{SC}.

When comparing data by Bruck *et al.* (Table 4.4), we need to keep in mind the different processing conditions that will affect the results. As they use of different

concentrations of squaraines, different spin speeds in the process of spin coating the active layer and the use of different solvents for the active layer. Chlorobenzene has a higher boiling point, which would lead to a larger time for the solvent to evaporate off. Whereas, using chloroform could cause de-wetting in our film, which could lead to the charge not being collected due to trap formed in the active layer. In conclusion, it is seen that the optimal device performance is achieved by maintaining high fullerene content to maximize mixing during the spin casting, as well as disruption of aggregation of the SQ molecules which will result in higher absorption in the NIR region. However, there is a trade-off between absorbance and domain size which need to be better understood.

The next step would be optimizing the concentration and spin speeds to get optimum thickness for devices, as this would help optimize the efficiency of the devices. Also, it is critical to use other techniques like AFM and TEM to understand the morphology in these films and see how it relates back to the H-type aggregate. More importantly it is important to look at the domain sizes and how we can use different annealing techniques to understand if annealing can help control the domain size and crystallinity of the active layer optimize our SQ:PCBM OPV devices.

As seen in this chapter that the PCBM completely disrupts the aggregation of the SQ, so it would be interesting to look at a ternary blend study with two different SQ. Assuming that disruption of aggregation actually leads to a higher efficiency, we might consider maintain a fixed blend ratio while varying the concentration of two different squaraines. The idea is that when we mix different squaraines the aggregation is disrupted independent of the concentration of PCBM. It is also assumed that when there is a mixture of squaraines, they may not crystallize. However, there would still be a pure squaraine phase which would phase separate

from the pure PCBM phase. There may also be an increase in the absorbance leading to an increase in the number of excited states that are converted into dissociated charges. Which then subsequently enhance short circuit current (J_{SC}). This will enhance the efficiency of the OPV devices.

Chapter 5 : Thermal Annealing Study

5.1 Introduction

In the previous chapter we have seen that the blend ratio 1:3 DHSQ(OH)$_2$:PCBM is the optimum blend ratio, as it has given us the highest device efficiency (0.86%). In this chapter, I am going to further optimize our devices by thermal annealing to further understand how annealing changes the morphology of our devices.

There are two different ways we can anneal our devices, 1) thermal annealing and 2) solvent vapor annealing. In this chapter, we will be focusing on how thermal annealing changes the active layer and how it affects our device efficiency. Thermal annealing relies on heating the substrate to a temperature greater than the glass transition temperature and close to the melting point of the SQ under study, allowing the material to move and orient to a more favorable conformation[35]. The main effect of annealing is the redistribution of fullerene[4] and the SQ molecules in the active layer (Figure 5.1).
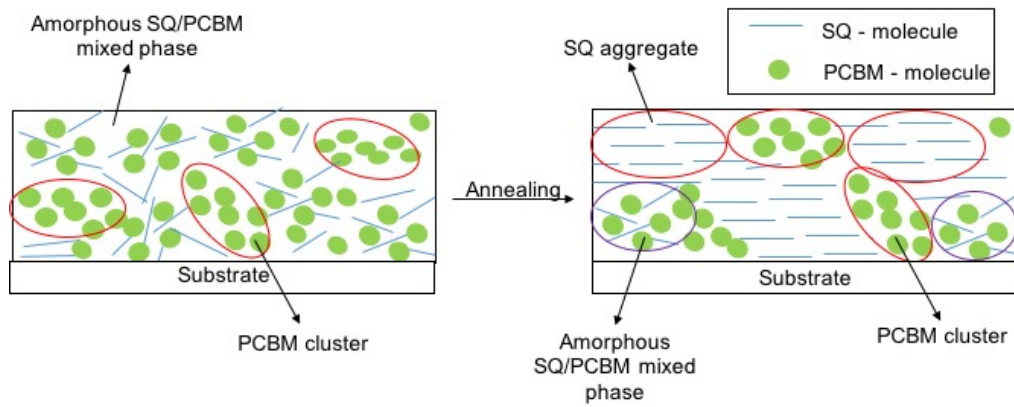
Figure 5.1: Effects of Annealing

As seen in Figure 5.1, the SQ molecules begin to aggregate, expelling isolated molecules of PCBM from the mixed phase, allowing the PCBM molecules to diffuse and combine into larger aggregates[4]. Annealing increases crystalline domain size. Increased crystal size means there are fewer heterojunctions where non-geminate recombination can occur. In addition, non-geminate recombination is also less likely because there are fewer traps caused by random SQ's in the PCBM. Therefore, an increase in phase separation means any recombination is less likely, which is expected to lead to an increase in the V_{OC} and FF[24]. Therefore efficiency of the OPV device is expected to increase with thermal annealing; there would increase crystallinity[4, 48](Figure 5.2[14]) and phase separation[4, 14], resulting a reduction in recombination. Thermal annealing, which leads to greater molecular alignment[4], will also result in improved charge transport[4] by increasing π-π stacking of the squaraine (aggregation of squaraine) for hole transport, and PCBM aggregation to provide a pathway for electron transport[48].
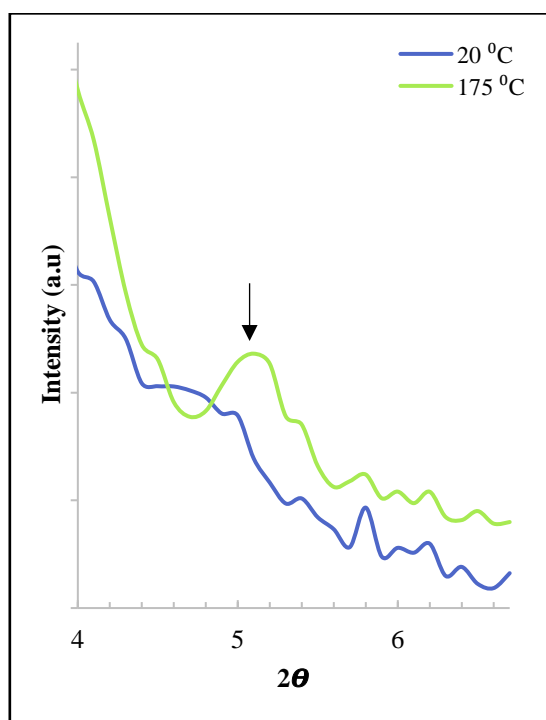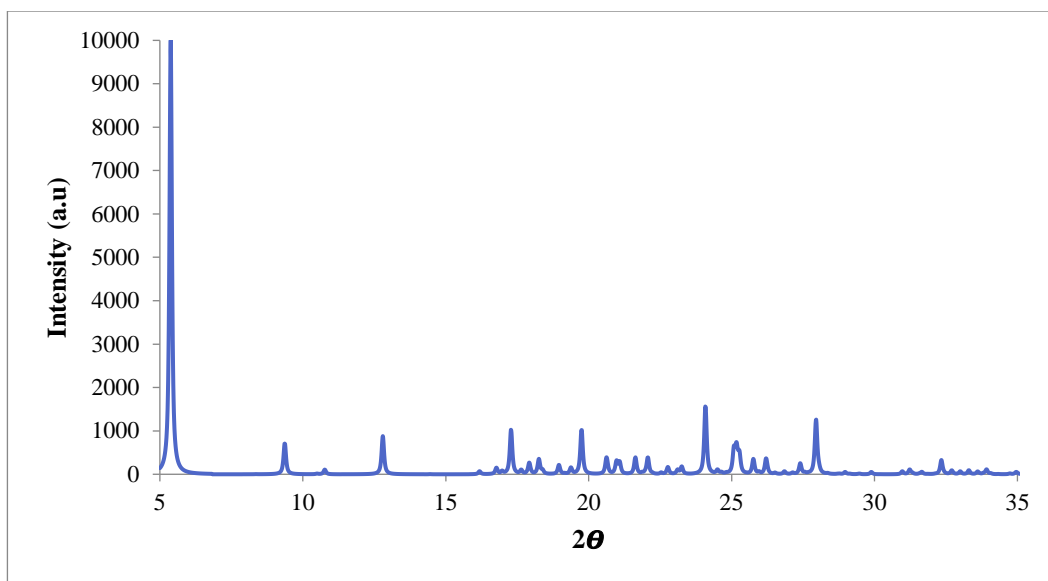
Figure 5.2: X-ray powder diffraction pattern of DHSQ(OH)$_2$ (Top) and diffraction patterns for DHSQ(OH)$_2$: PCBM films of weight ratio 25%:75% before (blue) and after (green) annealing at 175°C for 3 minutes (Bottom). The arrow is pointing to the main diffraction peak is located at 2Θ = 5.1, which corresponds to the (001) plane in the single crystal structure of the SQ molecule[14]

Figure 5.2 shows the X ray powder diffraction pattern of DHSQ(OH)$_2$ and the diffraction pattern for DHSQ(OH)$_2$:75% PCBM before and after thermal annealing at

175°C for 3 minutes. The main diffraction peak is located at 2Θ = 5.1, which corresponds to the (001) plane in the single crystal of the SQ. Before annealing (blue), there is a slight peak at 2Θ = 5.1. After annealing (green) there is an increase in the relative intensity of the crystal peak[14]. This increase in the intensity of the peak at 2Θ = 5.1 confirms that annealing increases the crystallinity in the active layer.

5.2 Experimental

UV-Vis absorbance

For UV-Vis absorbance measurements thin film samples were prepared by spin casting the active layer (1500 rpm for 18 seconds) from the blended SQ:PCBM chloroform solutions (the same as for device preparation) onto glass substrates cut from microscope slides. A Shimadzu UV-2401 spectrophotometer was used for absorption characterization. Settings of medium scan speed, 0.5 nm increments and a 2 nm slit width were applied when taking the measurements. Absorbance data from of these sample was then recorded from a wavelength of 300 nm to 900 nm. A blank glass slide was used to baseline the spectrum to account for scattering and absorption of substrates. Three measurements were taken for each film by changing the film position in the light path to account for any heterogeneity in the films.

Transmission electron microscopy (TEM)

TEM measurements of the SQ:PCBM films were obtained using a JEOL JEM-2010 operating at 200 kV with a 210 LaB6 filament and an AMT image capture system. The average domain size was quantified using ImageJ software. The measured $DHSQ(OH)_2:PC_{61}BM$ blend films were prepared using the same method as described in the UV-Vis section. Three films were prepared for each blend ratio; un-

annealed, annealed at 175 °C respectively. Films were prepared by dipping spin-cast films into water, which separated the films from the substrate. The films were then placed onto copper TEM grids covered with an amorphous carbon film. The water was allowed to evaporate under ambient conditions.

Device Fabrication

Eight precut Indium-tin-oxide (ITO) coated glass substrates were used. The substrates were cleaned using acetone and IPA under sonication conditions. A strip at the top of each substrate was taped to protect the ITO – anode from deposition of the active layer. The substrates were left in the vacuum oven (150°C) for an hour prior to spin-coating with 1:1 ratio of PEDOT:PSS: deionized water at a spin speed of 5000 rpm for 40 seconds before being left in the vacuum oven again for an hour. The substrates were then transferred into a nitrogen-filled glove box system where the active solar cell layer was spin-coated (1500 rpm for 18 seconds) from chloroform solutions. The solution of fixed concentration of $DHSQ(OH)_2$ to 4 mg/ml and varying concentration of PCBM corresponding to the blend ratio. One half of the substrates were thermally annealed at 175°C for 3 minutes and then transferred directly into high vacuum. Then the aluminum electrode was thermally evaporated through a shadow mask giving four solar cells with an area of approximately ~29 mm^2 for every sample.

J-V measurement

The J-V measurements were performed using a Newport solar simulator with a power density of 100 mW cm^{-2} (1-sun illumination). The OPV devices were tested immediately after fabrication by a four-point probe method. The out bias was scanned from -2 Volts to 2 Volts with a 0.4 Volt increment. The current density of the OPV

devices (under 1-sun illumination) was measured, and the J-V curve was obtained by measuring the current signal as a function of the voltage bias. The short-circuit current (J_{SC}), open-circuit voltage (V_{OC}) and fill factor (FF) were calculated by inserting the data into a calculating spreadsheet.

5.3 Results and Discussion

5.3.1 Absorbance
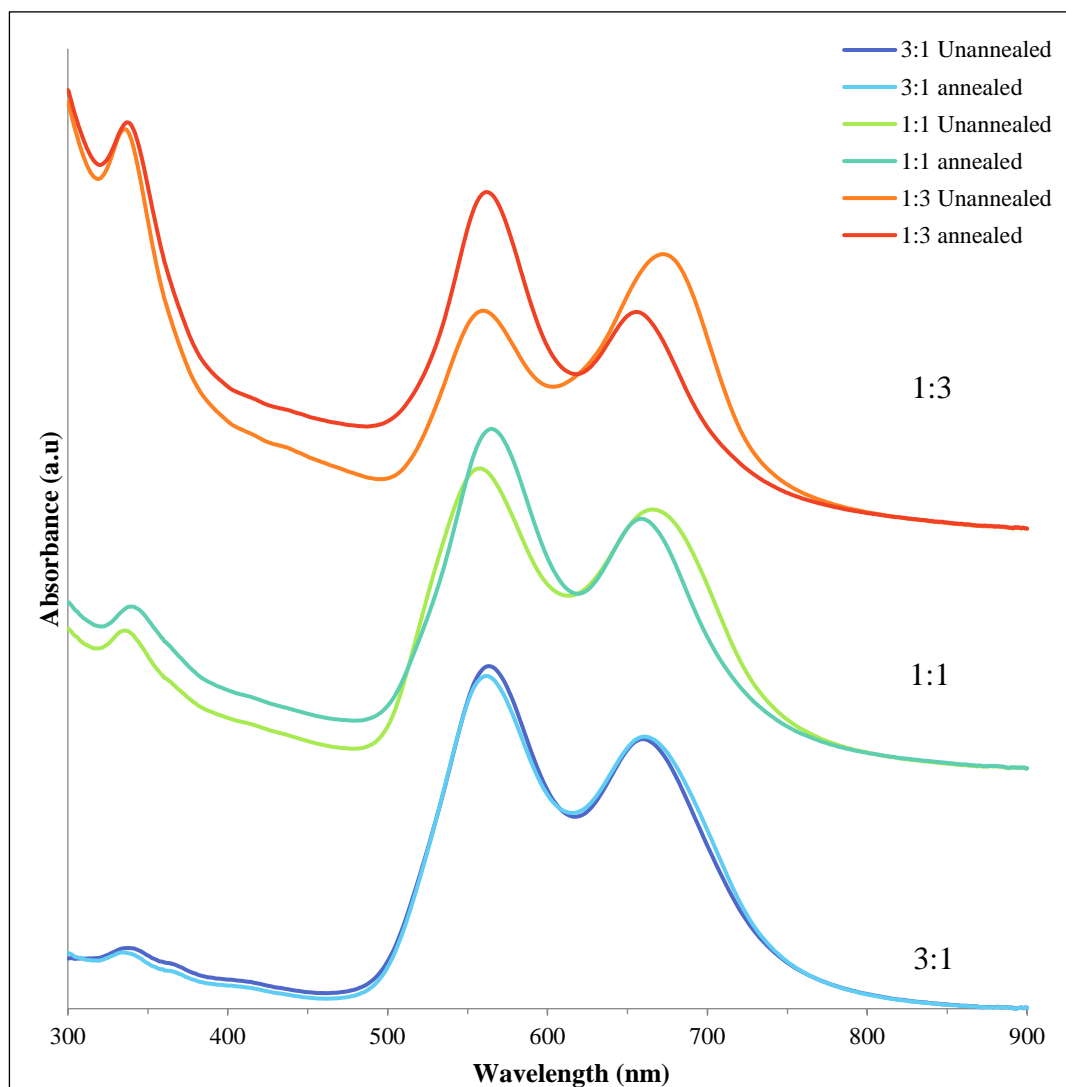
Figure 5.3: Absorbance spectra from spin-coated films of blends of DHSQ(OH)$_2$:PC$_{61}$BM in various mixing ratios as well as annealed at 175°C for 3 minutes as noted on the graph

The films were spin-coated on glass from the same chloroform solution as used for solar cell preparations. All UV-Vis absorption spectra are plotted in Figure 5.3. Figure 5.3 shows the absorbance of DHSQ(OH)$_2$:PCBM with and without annealing at varying blend ratios as a function of wavelength. The peak at 320 nm in

the blend ratio films is the absorbance of $PC_{61}BM$, which was chosen because it does not overlap with the squaraine absorbance, as opposed to $PC_{71}BM$, which does. The unannealed blend ratio films are compared to the annealed films to see how the aggregation (Section 1.4) changes as the films are thermally annealed at 175°C for 3 minutes. As we have seen in chapter 4, PCBM at higher concentrations can disrupt the aggregation of SQ. The blend ratios studied are 3:1 (dark blue for unannealed and light blue annealed), 1:1 (light green for unannealed and green for annealed), and 1:3 (orange for unannealed and red for annealed). All these spectra for these samples show two absorbance maxima, high energy aggregate peak (560 nm) and monomer peak mixed with the intermolecular charge transfer peak (660 nm). The 660 nm peak shifts when there is more monomer present. As said in chapter 3, this is due to the mixing of the ICT peak with the monomer peak. Therefore, this low energy peak shift is seen when there is a higher concentration of PCBM present as the PCBM will disrupt the aggregation of the SQ molecules.

When comparing the annealed and unannealed spectra for each blend (Figure 5.3), it can be seen for the blend ratio 3:1 that the annealed absorbance (light blue) doesn't change too much from the unannealed absorbance (dark blue). This is expected as there is a higher concentration of SQ compared to PCBM and therefore when the films were spin coated, they were completely aggregated, as there must be a higher concentration of PCBM required to significantly disrupt the aggregation of SQ (chapter 4). Comparing the unannealed with the annealed film for 1:1, there is a slight change in the spectra, it is mostly the intensity of the peaks that change, the high energy peak increases from 0.375 to 0.424 and the low energy peak decreases from 0.324 to 0.322 (Figure 5.4). It can be seen that for both spectra there is a higher population of the aggregate species, but for the unannealed (light green) it can be seen

that the low energy monomer peak is slightly broader when compared to the annealed (green), this is seen by the calculation of FWHM (Table 5.1). FromTable 5.1, it can be seen that the unannealed higher energy peak is slightly boarder compared to the annealed peak.

Table 5.1: The parameters for Gaussian fitting of normalized absorbance of SQ: PCBM blended films

SQ:PCBM Blends	High Energy Peak			Low energy peak		
	Peak Position (nm)	Peak height	FWHM (eV)	Peak position (nm)	Peak height	FWHM (eV)
3:1 unannealed	562.3	0.948	0.294	664.5	0.718	0.241
3:1 annealed	562.0	0.917	0.289	664.3	0.728	0.234
1:1 unannealed	557.7	0.964	0.297	666.6	0.815	0.255
1:1 annealed	564.3	0.904	0.280	663.0	0.636	0.225
1:3 unannealed	563.0	0.697	0.305	669.3	0.922	0.220
1:3 annealed	561.8	0.840	0.277	660.0	0.530	0.211

The low energy peak blue shifts (Figure 5.4) when it is annealed, possible due to an increase in population of H – aggregate. Note that other annealing absorption studies show that at the blend ratio 1:1, annealed at 110°C the film is completely aggregated after 1 minute of annealing (see appendix), therefore it is assumed that after annealing at 175°C for 3 mins this film should be completely aggregated.

The biggest change in the spectrum is for the blend ratio 1:3. From chapter 4, we know that this blend ratio is optimum for devices. From Figure 5.3, it can be seen that for the unannealed (orange) sample, there is a higher population for the monomer peak, with the monomer peak at 672 nm with an intensity of 0.323 and the aggregate

peak at 560 with an intensity of 0.272. When the films are annealed (red), it can be seen that the population of aggregate rapidly increases compared to monomers, with the monomer peak 655 with an intensity of 0.271 and the aggregate peak at 562 nm with an absorption intensity of 0.421 (Figure 5.4). It can be seen from Figure 5.3, the low energy peak is red shifted in the unannealed spectrum (orange) as compare to the annealed spectrum (red) for this blend.
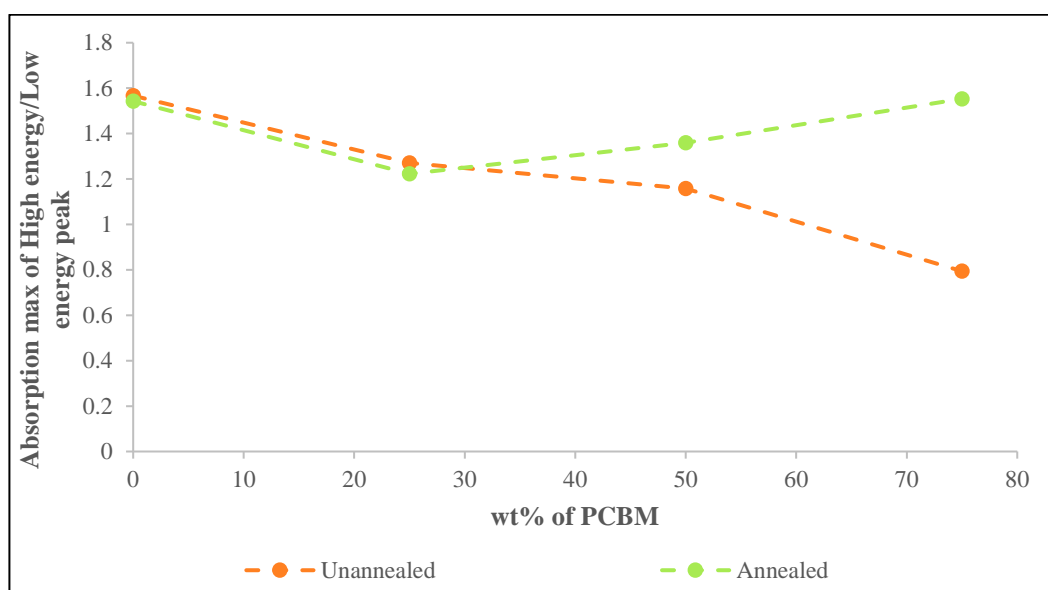
Figure 5.4: Shows the absorption max of high energy peak/low energy peak as a function of wt% of PCBM before (orange) and after (green) annealing

We know that with an increase in aggregation there is an increase in crystallinity[14, 49]. However, the device results need to be correlated to the absorbance to understand how annealing influences the efficiency of our devices.

5.3.2 Device Data

The solar cell had the layer arrangement of

$ITO/PEDOT:PSS/DHSQ(OH)_2:PC_{61}BM/Al$.

Table 5.2 : Shows the Device data for the different blend ratios with and without annealing. Values and error for PCE, V_{OC}, J_{SC} and FF reported here are averages and standard deviation obtained by testing a group of 16 devices for each point between batches

DHSQ(OH)$_2$: PCBM	Thermal treatment	Device Parameters			
		J_{SC} (mAcm^{-2})	V_{OC} (V)	FF	PCE
3:1	none	1.84 ± 0.41	0.23 ± 0.10	26.22% ± 1.51%	0.11% ± 0.07%
	175 °C	0.20 ± 0.06	0.02 ± 0.10	6.96% ± 10.69%	0.00% ± 0.00%[a]
1:1	none	4.15 ± 0.15	0.53 ± 0.05	39.15% ± 3.15%	0.86% ± 0.12%
	175 °C	0.54 ± 0.04	0.15 ± 0.08	26.03% ± 1.59%	0.02% ± 0.01%[a]
1:3	none	4.69 ± 0.30	0.52 ± 0.06	40.33% ± 5.95%	0.98% ± 0.19%
	175 °C	1.08 ± 0.33	0.18 ± 0.09	26.39% ± 1.35%	0.06% ± 0.05%[a]

a the devices showed diode behavior and the parameters can hardly be obtained

Table 5.2 shows the device parameters of DHSQ(OH)$_2$:PCBM OPV devices under different blend ratios and with/without annealing at 175°C for 3 minutes. It is important to note that these devices are not completely optimized and this efficiency would be improved by the use of an electron transport layer between the active layer and the aluminum, using PC$_{71}$BM rather than PC$_{61}$BM and by using MoO$_3$ as the buffer layer between ITO and the active layer.

The un-annealed devices have the highest average efficiency of 0.98% at a blend ratio 1:3, this is in agreement with the study done in chapter 4. It can be seen from this study that there is an increase in all the parameters from the 3:1 blend ratio to the 1:3 blend ratio and therefore the PCE increases too. For the devices annealed at

175°C, the efficiency dropped to 0% in all cases and these devices showed a diode-like behavior.

For the unannealed devices, the increase in all the device parameters is attributed to the increase in heterojunction interface, as the donor and acceptor phase are well mixed at high concentration of PCBM and therefore, there is a higher mobility of electron[50]. As seen from the absorbance (Figure 5.3), there is more absorbance in the near IR region of the spectrum as the content of PCBM is increased (25% PCBM to 75% PCBM), so therefore the J_{SC} would be expected to increase as more photons would be absorbed. There is a vast increase in V_{OC} from 0.23 V at 25% of PCBM to 0.53 V at 50% PCBM. This V_{OC} is related to the HOMO of the donor and the LUMO of the acceptor offset at the interface of the acceptor and donor molecule. Therefore, this increase in the V_{OC} can imply that there is a decrease in the HOMO energy level of the SQ donor molecule. As seen from Figure 5.3 and from chapter 4, as the PCBM content is increased there is in an increase in the population of monomer at 50% PCBM compared to the population of monomer at 25% PCBM. There is no change in the V_{OC} from 50% PCBM to 75% PCBM suggesting that there is no change in the energetics at SQ and PCBM interface. The Fill factor, tells us about the morphology of the active layer. The FF increased from 26.22% at 25% of PCBM to 40.33% at 75% of PCBM. This is a significant increase which could be due to the increase in the interface between the SQ and PCMB, as the phases are well mixed therefore the mobility are balanced[50], so the charges can be collected without rcombining[39].

For the annealed devices, it was expected that the increase in aggregation and crystallinity would result in an increase of efficiency in our devices. Thus, there would have better charge mobility for the efficient charge separation and charge

collection. This would help to reduce charge recombination losses and therefore increase the PCE. But in this study, annealing at 175°C had a detrimental effect on the PCE. A possible reason could be due to the separation of the well mixed phases of SQ and PCBM into large pure domains due to annealing. These domains become larger than the exciton diffusion length, so the exciton doesn't reach the interface to be able to dissociate into free charges[14]. Therefore, to help explain these results we need to look at the TEM images to understand how the morphology changes with annealing.

5.3.3 Transmission Electron Microscopy
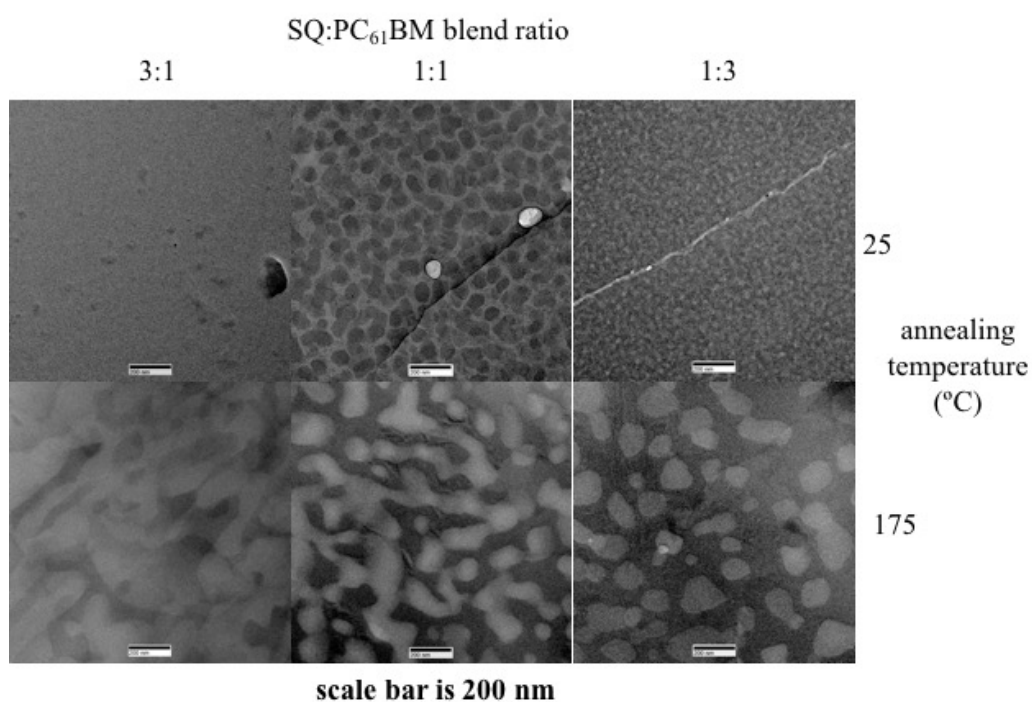
Figure 5.5: Shows TEM images of spin-cast DHSQ(OH)₂:PCBM films without treatment (top) and annealed at 175 °C (bottom) for 3 minutes. The blend ratios that are studied are: 25 wt%, 50 wt% and 75 wt% of PC₆₁BM (left to right). The scale bar at the

To study the phase separation in our active layer, transmission electron microscopy (TEM) was used (Figure 5.5[14]). Figure 5.5 shows the TEM images DHSQ(OH)$_2$:PCBM films without annealing and with annealing at 175°C for 3 minutes, for blend ratio 3:1, 1:1 and 1:3 DHSQ(OH)$_2$:PCBM. For the unannealed film at blend ratio of 3:1 DHSQ(OH)$_2$:PCBM, this mixture seems to be a homogenous film as pure phase domains of SQ and PCBM cannot be differentiated. For the blend ratio 1:1 DHSQ(OH)$_2$:PCBM, the pure phase domain can be seen, with an estimated size 50 - 100 nm but are larger domains compared to pure domain in the unannealed blend ratio 1:3 DHSQ(OH)$_2$:PCBM with an estimated size of 25 – 50 nm. The 1:3 DHSQ(OH)$_2$:PCBM, has much smaller and finer phases formed. This is in agreement with our absorbance spectra (Figure 5.3), as the content of PCBM is increased there is a decrease in SQ aggregation compared to monomer but there is still some population of aggregate. Therefore, as seen from TEM data there are crystalline domains formed but they are smaller in size, which means the heterojunction interface increases. Annealing the films at 175°C for 3 minutes, causes the domains to increase in size dramatically for all the blend ratios. Due to the larger domain size, which could be larger than the exciton diffusion length, it is very likely that device efficiency drops are explained by the exciton will not reaching the interface. Another reason large domains are bad is because there is more chance for recombination.

5.4 Conclusion

In this chapter, it is reconfirmed that the blend ratio 1:3 for DHSQ(OH)$_2$:PCBM blend is the optimum blend ratio for DHSQ(OH)$_2$ with the PCE

of 0.98% which is in agreement with the results in chapter 4. To interpret these results, we need to look at the equation for OPV efficiency (Equation 5.1) which was introduced in chapter 1:

$$\eta_{OPV} = \eta_{Abs}\eta_{ED}\eta_{CS}\eta_{CT}\eta_{CC}$$

<div align="center">**Equation 5.1**</div>

From Figure 5.3, it can see that as the PCBM content is increased there is a change in the spectra from blend ratio 3:1 to 1:3. There is an increase in the near IR absorbance for the blend 1:3, therefore there is an increase in the η_{Abs} term of the equation at blend ratio 1:3 for the unannealed films. Looking at that unannealed absorbance data for the blends 3:1 and 1:1, the SQ molecules are mainly aggregated, we note that the charge mobility should be about the same. Therefore η_{CT} term is expected to be similar for blend 3:1 and 1:1 but would be lower for 1:3, as the active layer is more amorphous as there is more monomer form. We speculate that the η_{CC} will be different for all 3 blends as, if we look at the TEM images (Figure 5.5), we can see that there may be a high rate of recombination for blend 3:1 as this film seems to be homogenous and the pure phase domains of SQ and PCBM cannot be differentiated. Therefore, the efficiency of charge collection would be assumed to be very low. Whereas for 1:1 and 1:3, the term η_{CC} would be assumed to about the same because there are pure phase domains formed in the unannealed TEM images and there would be a low rate of recombination. The η_{ED} term and η_{CS} term, are based on the interfacial area between the pure donor domain and pure acceptor domain in the active layer. From the TEM images it can be seen that the η_{ED} term and η_{CS} term would be different for all 3 unannealed films. Blend ratio 1:3 gives the optimum efficiency as there is an increase for all these parameters. η_{Abs} increases as there is more absorbance in the near IR as there are more monomers that absorb. η_{ED} and η_{CS}

will be more efficient as the TEM images show that there are smaller and finer phases. Therefore, there is a larger interfacial area. η_{CT} however, may be less efficient compared to blend ratio 1:1 and 3:1, as the active layer is regarded to be mainly amorphous. The η_{CC} term takes recombination into account. Therefore, looking at the TEM images, it can be see that as there are smaller and finer domains, I assume a lower rate of recombination and more efficient charge collection. As most of these parameters show an increase, therefore the overall efficiency would increase.

Now lets us look at the device efficiency for unannealed. Which showed an increase in the J_{SC} from blend ratio 3:1 to 1:3, as there is more absorbance in the near IR region of the spectra as PCBM content is increased (25% PCBM to 75% PCBM). The increase in the V_{OC} can imply that there is a decrease in the HOMO energy level of the SQ donor molecule, as seen from Figure 5.3 and from chapter 4, that as the PCBM content is increased there is in an increase in the population of monomer at 50% PCBM compared to the population of monomer at 25% PCBM. There is no change in the V_{OC} from 50% PCBM to 75% PCBM suggesting that there is no change in the energetics at SQ and PCBM interface. The FF increased from 26.22% at 25% of PCBM to 40.33% at 75% of PCBM. This is a significant increase which could be due to the increase in the interface between the SQ and PCMB, as the phases are well mixed therefore the mobility may be balanced[50], so the charges can be collected without rcombining[39].

The efficiency of the device for annealing was expected to improve the morphology of the active layer and therefore improve the efficiency of our devices. The main reasons the PCE was expected to increase, was that annealing increases aggregation of SQ molecules and hence induces more ordered packing which leads to an increase in the extent of crystallinity[14, 48], as seen from Figure 5.2. But in this

study, it is seen that annealing at 175°C for 3 minutes is detrimental for devices. Although from the absorbance spectra (Figure 5.3) it is seen that there is a conversion from monomer to aggregate, meaning there is an increase in the extent of crystallinity in our active layer. The main reason that annealing is detrimental in this study is due to the fact that after annealing it is seen that there is a dramatic increase in domain size for all the blend ratios (Figure 5.5). Therefore, if the domain size exceeds the exciton diffusion length (typically < 10 nm), the exciton generated in the middle of the pure donor or acceptor domain will not be able to reach the interface, and thus will not be converted to free carriers. Also, the larger the domain size, the smaller the interfacial area, and this is where the exciton dissociation takes place. This means that interfacial area is critical for the photo induced charge generation in our devices.

As seen from this study, the morphology of ore device is directly impacts the efficiency of our devices. The optimum morphology in our device would be well mixed, small domains of the donor and acceptor phases, so that the charges can be collected more efficiently[39]. To achieve this through annealing we can see that choosing the annealing temperature is critical when thermally annealing our devices. Crystallinity is important for charge mobility but the degree of phase separation needs to be controlled as well.

Chapter 6 : Controlling Phase Separation with Thermal Annealing

6.1 Introduction

As seen in the chapter 5, annealing at 175°C induced a drastic change in the phase separation. The main reason considered to have been for a drop in PCE was that the pure domains of SQ and PCBM were larger than the exciton diffusion lengths. Therefore, to avoid this, we hypothesize that the temperature to anneal these devices is critical. In this chapter, we will also explore how crystallinity can be maximized while phase separation is controlled through selection of a lower annealing temperature.
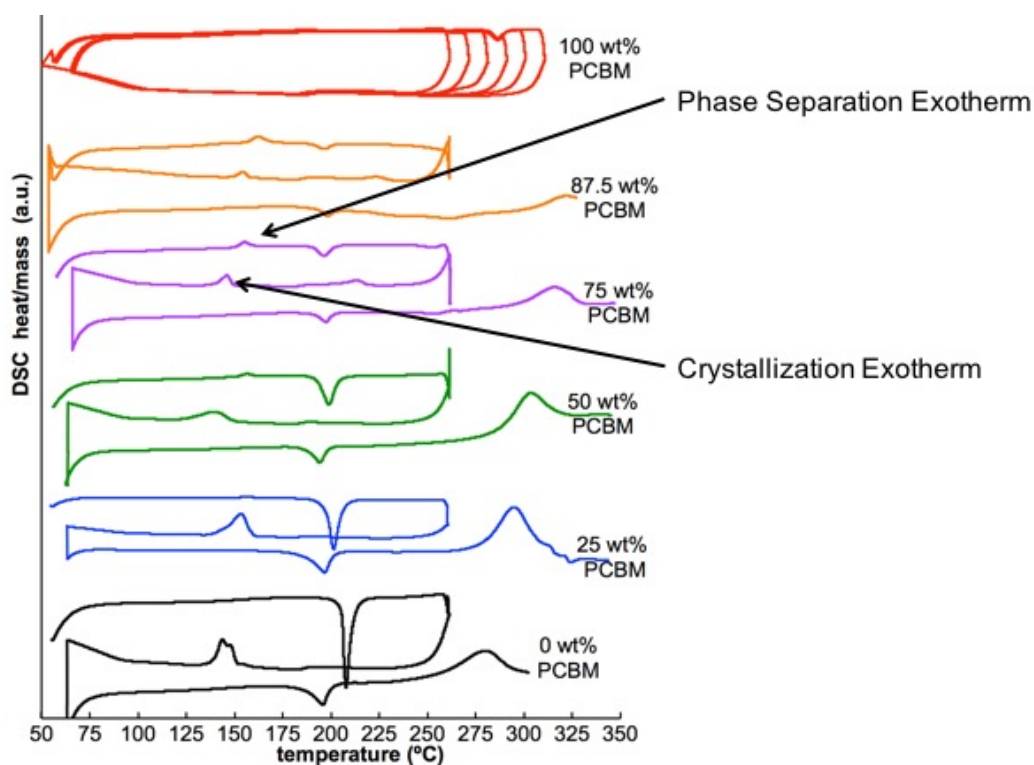
Figure 6.1: Differential Scanning Calorimetry of DHSQ(OH)$_2$:PC$_{61}$BM Blends data[14]

It is the temperature we choose to anneal our devices which is critical, as we want the temperature to be higher enough to ensure the material crystallizes but low enough so the material doesn't completely phase separate into large domains. Differential scanning calorimetry data (Figure 6.1[14]) helps us to choose the temperature. There are three steps to these measurements, 1) the samples were heated to up to 260°C, 2) cooled back down to 75 °C and 3) heated up to 350 °C. If we look at the 75 wt% PCBM blends (purple line) in Figure 6.1, as this is the optimum blend ratio for devices seen from chapter 4, we start with amorphous solid. It can be seen that in step one there is an exotherm at ~155 °C and an endotherm at ~194 °C. The endotherm is associated with the melting point of SQ and the exotherm is associated with the phase separation. This exotherm is not seen in step three when the sample is again heated as the material has completely phase separated in step one. When the sample is cooled (step two) there is an exotherm at ~135°C which corresponds to the crystallization exotherm of $DHSQ(OH)_2$. Therefore, we can hypothesize that by annealing our device at a temperature below this phase separation exotherm and above the crystallization exotherm, crystallization can be encouraged with little or no phase separation. We propose that by enhancing the crystallinity (Figure 6.2), the resulting PCE of our devices would improve, as there would be a better balance in charge mobility.
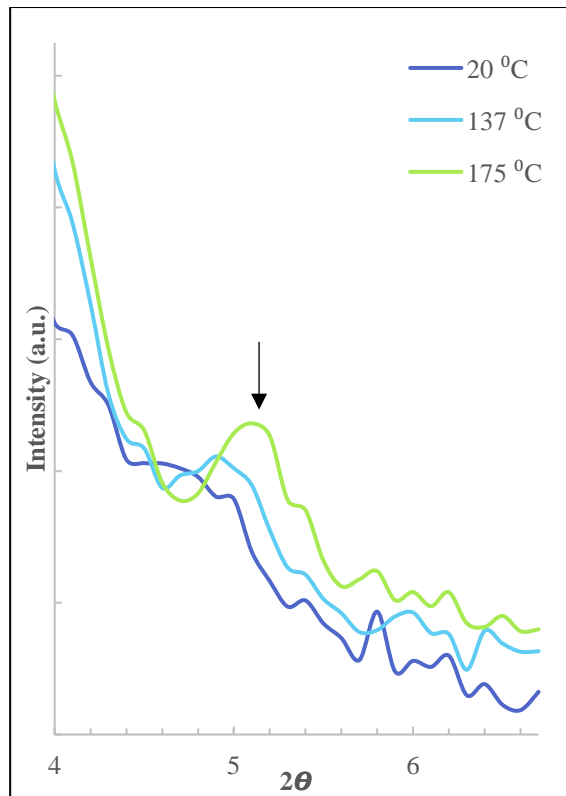
Figure 6.2: X-ray diffraction patterns for DHSQ(OH)$_2$:PCBM films of weight ratio 25%:75% before (dark blue) and after annealing at 137°C (blue) and 175°C (green). The arrow point to the main diffraction peak is located at 2Θ = 5.1, which corresponds to the (001) plane in the single crystal structure of SQ molecule[14]

Figure 6.2 shows the X ray diffraction data for DHSQ(OH)$_2$:PCBM with a weight ratio of 25%:75% before and after thermal annealing at 137°C and 175°C. The main diffraction peak is located at 2Θ = 5.1, which corresponds to the (001) plane in the single crystal. Before annealing (dark blue), there is a slight peak at 2Θ = 5.1. After annealing at 137°C (blue) and 175°C (green) there is an increase in the relative intensity of the crystal peak[14]. Signal to noise is low. This data is consistent with the hypothesis that annealing increases the crystallinity in the active layer.

6.2 Experimental

<u>UV-Vis absorbance</u>

For UV-Vis absorbance measurements thin film samples were prepared by spin casting the active layer (1500 rpm for 18 seconds) from blended SQ:PCBM chloroform solutions (the same as for device preparation) onto glass substrates cut from microscope slides. A Shimadzu UV-2401 spectrophotometer was used for absorption characterization. Setting of medium scan speed, 0.5 nm increments and 2 nm slit width were applied when taking the measurements. Absorbance data from these samples were then recorded from a wavelength of 300 nm to 900 nm. A blank glass slide was used to baseline the spectrum to account for scattering and absorption of substrates. Three measurements were taken for each film by changing the film position in the light path to account for any heterogeneity in the films.

<u>Transmission electron microscopy (TEM)</u>

TEM measurements of the SQ:PCBM films were obtained using a JEOL JEM-2010 operating at 200 kV with a 210 LaB6 filament and an AMT image capture system. The average domain size was quantified using ImageJ software. The measured $DHSQ(OH)_2:PC_{61}BM$ blend films were prepared using the same method as described in the UV-Vis section. Three films were prepared for each blend ratio; un-annealed, annealed at 137°C and 175 °C respectively. Films were prepared by dipping spin-cast films into water, which separated the films from the substrate. The films were then placed them onto copper TEM grids covered with an amorphous carbon film. The water was allowed to evaporate under ambient conditions.

Device Fabrication

Eight precut Indium-tin-oxide (ITO) coated glass were used. The substrates were cleaned using acetone and IPA under sonication conditions. A strip at the top of each substrate was taped to protect the ITO – anode from deposition of the active layer. The substrates were left in the vacuum oven (150°C) for an hour prior to spin-coated with 1:1 ratio of PEDOT:PSS: deionized water at a spin speed of 5000 rpm for 40 seconds before being left in the vacuum oven for an hour. The substrates were then transferred into a nitrogen-filled glove box system where the active solar cell layer was spin-coated (1500 rpm for 18 seconds) from chloroform solutions. The solution of fixed concentration of $DHSQ(OH)_2$ to 4 mg/ml and varying concentration of PCBM corresponding to the blend ratio. One half of the substrates were thermally annealed at 137°C and 175°C for 30 secs and then transferred directly into high vacuum. Then the aluminum electrode was thermally evaporated through a shadow mask giving four solar cells with an area of approximately ~29 mm^2 for every sample.

J-V measurement

The J-V measurements were performed using a Newport solar simulator with a power density of 100 mW cm^{-2} (1-sun illumination). The OPV devices were tested immediately after fabrication by a four-point probe method. The out bias was scanned from -2 Volts to 2 Volts with a 0.4 Volts-increment. The current density of the OPV devices (under 1-sun illumination) was measured, and the J-V curve was obtained by measuring the current signal as a function of the voltage bias. The short-circuit current (J_{SC}), open-circuit voltage (V_{OC}) and fill factor (FF) were calculated by inserting the data into a calculating spreadsheet.

6.3 Results and Discussion

6.3.1 Absorbance

The films were spin-coated on glass from the same chloroform solution as used for solar cell preparations. All UV-Vis absorption spectra are plotted in Figure 6.3. Figure 6.3 shows the absorbance of DHSQ(OH)$_2$:PCBM blends with and without annealing at 137°C and 175°C as a function of wavelength. The peak at 320 nm in the blend ratio films is the absorbance of PC$_{61}$BM, which was chosen because as seen in Figure 6.3 it does not overlap with the squaraine absorbance, as opposed to PC$_{71}$BM, which does. The unannealed blend ratio films are compared to the annealed films to see how the aggregation changes when the films are thermally annealed at different temperatures (137 °C and 175°C). As we already have seen in chapter 4, the PCBM at higher concentration can disrupt the aggregation of SQ. The blend ratios studied are 1:1 (light green for unannealed, dark blue for annealed at 137°C and green for annealed at 175°C) and 1:3 (orange for unannealed, light blue for annealed at 137°C and red for annealed). All these spectra for these samples show two absorbance maxima, aggregate (560 nm) and monomer peak mixed with the intermolecular charge transfer peak (660 nm). The 660 nm peak shifts when there is more monomer present. As said in chapter 3, this is due to the mixing of the ICT peak with the monomer peak. Therefore, the low energy peak shifts are seen when there is a higher concentration of PCBM present as the PCBM will disrupt the aggregation of the SQ molecules.
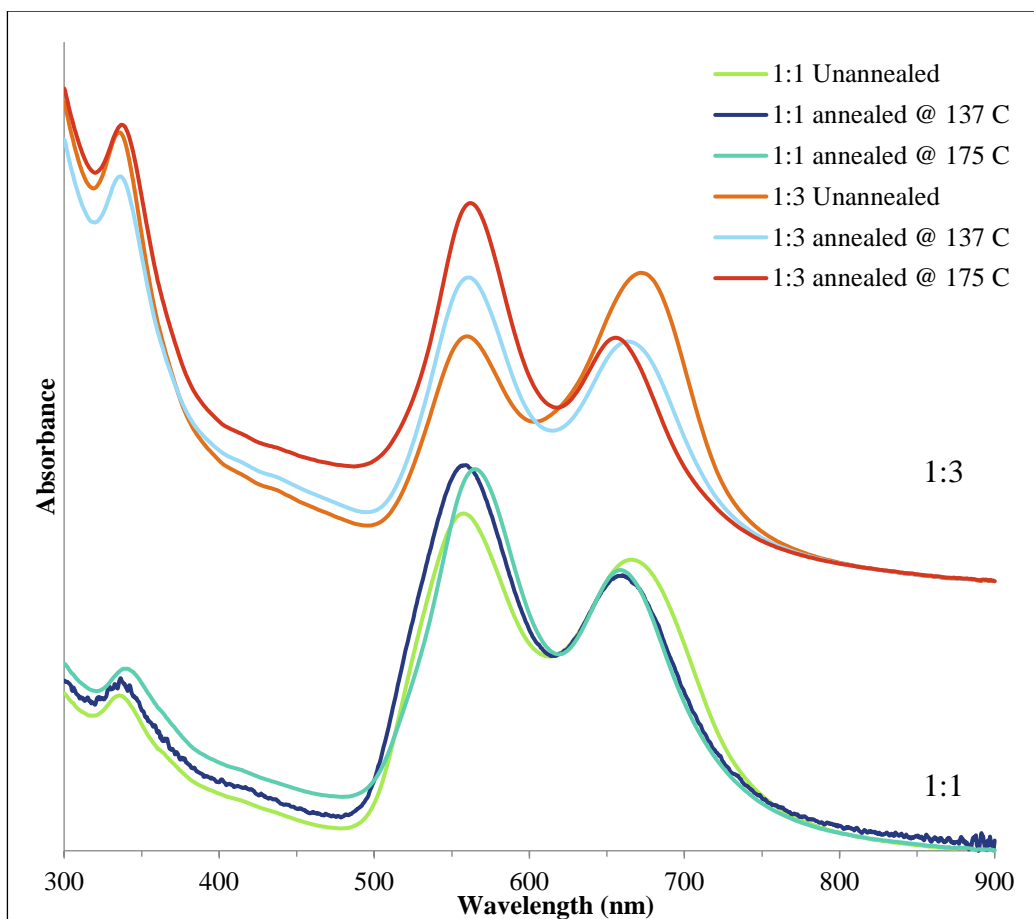
Figure 6.3: Absorbance spectra from spin-coated films of blends of DHSQ(OH)$_2$:PC$_{61}$BM in various mixing ratios as well as annealed at 137°C and 175°C as noted on the graph

When comparing the unannealed and annealed at 137°C and 175°C for each blend (Figure 6.3), it can be seen for the blend ratio 1:1, there is a slight change in the spectra from unannealed and annealed, it is mostly the intensity of the peaks that change, as the high energy peak at 558 nm increases from 0.375 (unannealed) to 0.429 (annealed at 137°C) and the low energy peak at 660 nm decreases from 0.324 (unannealed) to 0.307 (annealed at 137°C). It can be seen that for both spectra there is a higher population of species of the aggregate, but for the unannealed (light green) it can be seen that the low energy monomer peak is slightly broader when compared to the annealed (dark blue and green). The low energy peak is blue shifted when it is

annealed due to the population of H-aggregation increasing. More importantly, note that there isn't much change in the spectra when annealed at different temperature (dark blue for 137°C and green for 175°C). This might indicate that the film is completely aggregated at 137°C. The biggest changes in the spectra are for the blend ratio 1:3. From chapter 4 we know that this blend ratio is optimum for devices. From Figure 6.3, it can be seen that for the unannealed (orange) there is a higher population for the monomer peak (0.643 at 660 nm compared 0.572 at 560 nm); the low energy peak is red shifted (from 672 nm for unannealed to 663.5 nm when annealed 137°C) compared to the annealed spectrum (light blue and red) for this blend. When the films are annealed (light blue and red), it appears as if the population of the aggregate rapidly increases compared to monomer (0.638 at 560 nm and 0.568 at 660 nm).

When comparing the annealed at 137°C (light blue) of the 1:3 ratio with the spectra of the film annealed at 175°C (red), there is a difference in the intensity of the high energy peak. It can be seen from Figure 6.3, that when the film is annealed at 137°C, the film is not completely aggregated. We consider, from the X-ray diffraction data that given an increase in crystallinity there is an increase in aggreration[14, 49]. We wish to confirm our hypothesis that annealing at the temperature below the phase separation exotherm and above the crystallization exotherm, will encourage crystallization with little or no phase separation. This would result in an enhancement in PCE. We need to further look at device results to be able correlated to the absorbance and annealing at a lower temperature influences on the efficiency of our devices. Also, the TEM images need to be analyzed to understand the phase separation and domain size of our pure domains after annealing.

6.3.2 Device Data

Figure 6.4 shows the J-V curve measurements of DHSQ(OH)$_2$:PCBM (1:1 and 1:3 w/w) OPV devices under annealing temperatures at 137°C. The shape of the J-V curve demonstrates a successful device (with an average efficiency of 0.86% for blend ratio 1:1 and an average efficiency of 0.98% for blend ratio 1:3 for as-cast devices). It should be noted that these devices are un-optimized (as there is no electron transporting layer or using PC$_{61}$BM rather than PC$_{71}$BM). The pre-annealing treatment at 137°C was performed on the devices, and the efficiency increased to 0.93% for blend ratio 1:1 and 1.24% for blend ratio 1:3. From Figure 6.4, it can be seen that the low slope at the J$_{SC}$ is likely associated with a low shunt resistance, which means there is current loss due to leakages across the junction. More detailed device parameters are listed in Table 6.1 below.
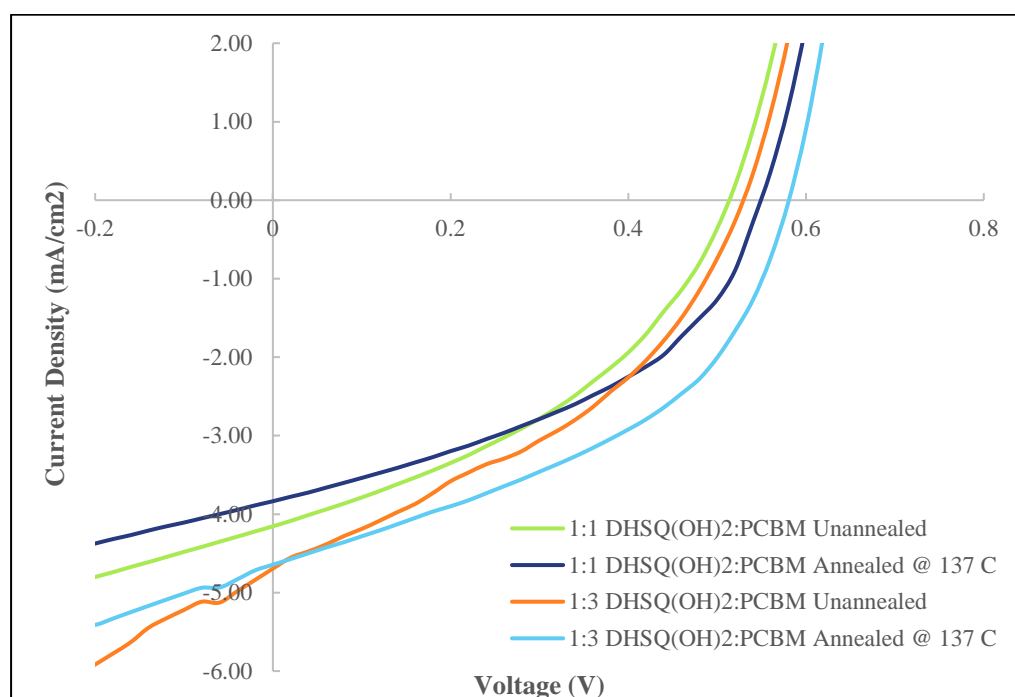
Figure 6.4: Summarized J-V curve measurement for DHSQ(OH)$_2$:PCBM (1:1 and 1:3 w/w) blended devices before and after annealing at 137°C

The solar cell had the layer arrangement of

ITO/PEDOT:PSS/DHSQ(OH)$_2$:PC$_{61}$BM/Al.

Table 6.1: Shows the Device data for the different blend ratio with and without annealing at 137°C and 175°C. Values and error for PCE, V$_{OC}$, J$_{SC}$ and FF reported here are averages and standard deviation obtained by testing a group of 16 devices for each point between batches

DHSQ(OH)$_2$:PCBM	Thermal treatment	Device Parameters			
		J$_{SC}$ (mAcm^{-2})	V$_{OC}$ (V)	FF	PCE
1:1	none	4.15 ± 0.15	0.53 ± 0.05	39.15% ± 3.15%	0.86% ± 0.12%
	137 °C	3.83 ± 0.22	0.56 ± 0.04	43.06% ± 5.15%	0.93% ± 0.18%
	175 °C	0.54 ± 0.04	0.15 ± 0.08	26.03% ± 1.59%	0.02% ± 0.01%[a]
1:3	none	4.69 ± 0.30	0.52 ± 0.06	40.33% ± 5.95%	0.98% ± 0.19%
	137 °C	4.64 ± 0.21	0.59 ± 0.07	44.71% ± 6.11%	1.24% ± 0.26%
	175 °C	1.08 ± 0.33	0.18 ± 0.09	26.39% ± 1.35%	0.06% ± 0.05%[a]

a The devices showed diode behavior and the parameters can hardly be obtained

Table 6.1 shows the device parameters of DHSQ(OH)$_2$:PCBM OPV devices under different blend ratio, with and without annealing at 137°C and 175°C. Again, it is important to remember that these devices are not completely optimized and this efficiency would be improved by the use of an electron transport layer between the active layer and the aluminum, using PC$_{71}$BM rather than PC$_{61}$BM and by using MoO$_3$ as the buffer layer between ITO and the active layer.

As mentioned in the previous chapter, the unannealed devices have the highest average efficiency of 0.98% at a blend ratio 1:3. Also, mentioned in the previous chapter, annealing at 175°C destroys the efficiency of our devices and we think this to

mainly be due to large pure domains being formed. For the devices annealed at 137°C, which is the temperature below the phase separation exotherm but above the crystallization exotherm temperature (Figure 6.1), the efficiency for both the blends increased.

For the unannealed devices we see an increase in all the device parameters, which we think mainly due to the increase in the donor and acceptor phases being well mixed at high concentration of PCBM (increase in heterojunction interface). There is an increase in the J_{SC} as you go from 50% PCBM to 75% PCBM, which we attribute to a higher absorbance intensity in the near IR region of the spectrum (Figure 5.3, Figure 6.3). The Fill factor, tells us about the 'squareness' of the J-V curve. The increase in FF is likely due to the increase in the interface between the SQ and PCMB; the phases are well mixed and therefore would reduce free charges from recombining.

For the annealed devices, we expected an increase in the efficiency of our devices annealed at 137°C compared to those annealed at 175°C. In chapter 5 it was seen that annealing at 175°C gave an increase in crystallinity but also large pure phase domains (Figure 5.5), which is detrimental for our devices. Therefore annealing at a lower temperature (above the crystallinity exotherm but blow the phase separation exotherm), would see an increase in crystallinity and therefore an increase the extent of aggrgation[14] but with small pure phase domains in our devices. This would, lead to better charge mobility, more efficient charge separation and better charge collection. This would help to reduce charge recombination losses and increase the PCE. In this study, annealing at 137°C showed an increase in the PCE. This increase is mainly due to the improvement in fill factor and open circuit voltage. The short circuit current slightly drops after annealing the devices, from 4.15 mAcm^{-2} to 3.83 mAcm^{-2} for 50%

PCBM and from 4.69 mAcm^{-2} to 4.64 mAcm^{-2} for 75% PCBM. This was expected as there is a higher population of aggregate species compared to monomer, and therefore there is a relative loss in absorbance of the higher population of photons absorbed at the near IR region of the spectrum (Figure 1.6). The open circuit voltage shows a slight increase for both 50% PCBM and 75% PCBM. As we already know the V_{OC} is related to the offset of the HOMO of the donor and LUMO of the acceptor at the interface. But by looking at the absorbance spectrum (Figure 6.3), it can be seen that there is an increase in the population of the aggregate species compared to the monomer for both the blend. This suggests there is a slight change in the energetics at the SQ and PCBM interface. But as there is more population of the aggregate species, there should be an increase in the HOMO energy level of the donor as seen in Figure 1.15. This should cause a decrease in the V_{OC}. Therefore, this increase in the V_{OC}, is considered more likely to be due to a there being a decrease in recombination; annealing at the lower temperature does still increase crystallinity while having smaller domain sizes. The decrease in recombination would also lead to a significant increase in fill factor which is observed for these data. This is consistent with an increase in the interface between the SQ and PCMB; as the phases are well mixed' therefore the mobility are balanced[50] and the charges can be collected without recombining[39]. Therefore, to look at phase separation we need to look at the TEM images to understand the morphology change and phase domains sizes due to annealing.

6.3.2 Transmission Electron Microscopy
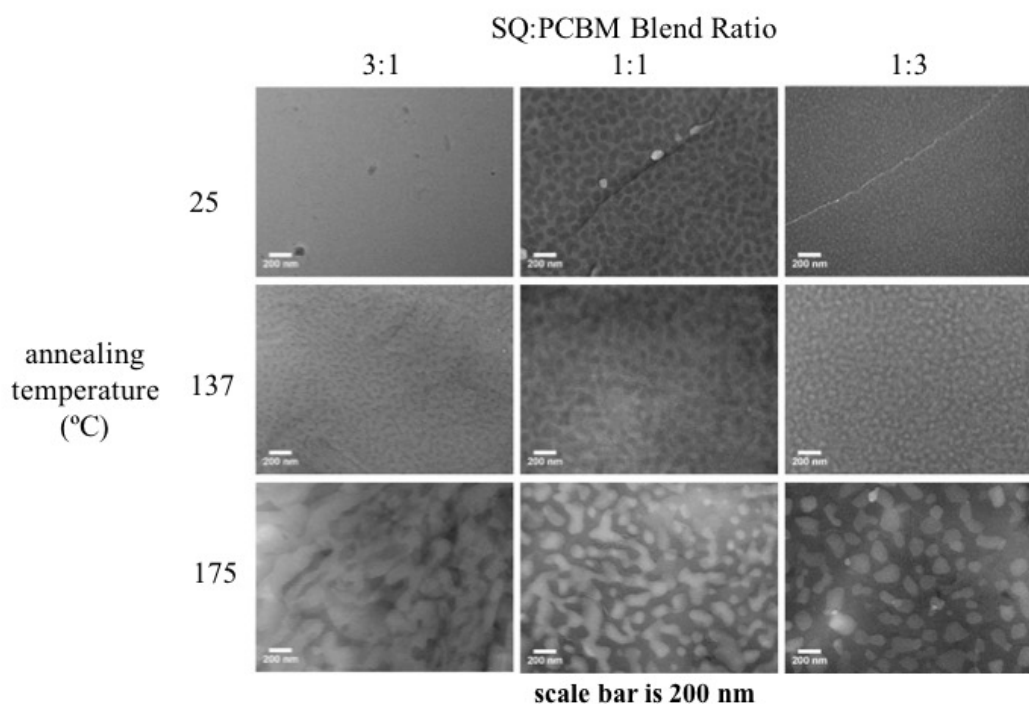
Figure 6.5: Shows TEM images of spin-cast DHSQ(OH)$_2$:PCBM films without treatment (top), annealed at 137 °C (middle) and annealed at 175 °C (bottom). The blend ratios that are studied are: 25 wt%, 50 wt% and 75 wt% of PC$_{61}$BM (left to right). The scale bar at the bottom of each image is 200 nm[14]. The dark regions are the PCBM domains and the lighter region are the SQ domains.

To study the phase separation in our active layer, transmission electron microscopy (TEM) was used (Figure 6.5[14]). Figure 6.5 shows the TEM images DHSQ(OH)$_2$:PCBM film without annealing and with annealing at 137°C and 175°C, for blend ratio 3:1, 1:1 and 1:3 DHSQ(OH)$_2$:PCBM. As seen in the previous chapter, for the unannealed film at blend ratio of 3:1 DHSQ(OH)$_2$:PCBM, this mixture seems to be a homogenous film as the pure phase domains of SQ and PCBM cannot be differentiated. For the blend ratio 1:1 DHSQ(OH)$_2$:PCBM, the pure phase domains can be seen but are larger domains compared to pure domain in the unannealed blend ratio 1:3 DHSQ(OH)$_2$:PCBM. The 1:3 DHSQ(OH)$_2$:PCBM, has much smaller and

finer phases formed. This is in agreement with our absorbance spectra (Figure 5.3 and Figure 6.3), as the content of PCBM is increased, there is a decrease in SQ aggregation compared to monomer but there is still some population of aggregate. Therefore, as seen from TEM data there are crystalline domains formed but they are smaller in size, which means the heterojunction interface increases. Annealing the films at 175°C causes the domains to increase in size dramatically for all the blend ratios. We know this is bad for our device as seen in the previous chapter. Therefore, annealing at the lower temperature at 137°C, it can be seen that the phase separation was there but it is not as drastic as when the films were annealed at 175°C. There was an increase in the aggregate absorption in the UV-vis spectra (Figure 6.3) after annealing at 137°C, and we know there is also an increase in the extent of crystallinity (Figure 6.2). After annealing at 137°C, all of these small morphological features likely lead to a decrease in the recombination of charges, which leads to an increase in device performance. Therefore, we can see that choosing an appropriate annealing temperature is critical to minimize phase separation and optimize the active layer morphology for OPV devices.

6.4 Conclusion

In this chapter, we have further optimized our devices by understanding how thermal annealing affects the morphology of our devices. In this chapter, we saw that annealing temperature is critical for morphology. It was found that annealing at 137°C showed an enhancement in our efficiency from 0.98% to 1.24% for 1:3 DHSQ(OH)$_2$:PCBM blends.

From Figure 6.3, we can see that as we anneal the film at 137°C there is an increase in the population of the aggregate species and a decrease in the monomer

population. Therefore, there is a loss in absorbance, as we are losing the absorption of photon near the near IR region of the spectrum. Due to this loss, there is a slight decrease in the J_{SC} for the devices after annealing at 137°C (Table 6.1). The charge transfer should increase after annealing, as the SQ molecules are mainly aggregated, therefore we note that the charge mobility will increase. There is an improvement in charge collection for after annealing at 137°C, consistent with our TEM images (Figure 6.5) interpretation, where we note that there are smaller pure domains formed and therefore there should be a decrease in recombination and better charge collection. The exciton diffusion and charge separation, are based on the interfacial area between the pure donor domain and pure acceptor domain in the active layer. From the TEM images we can see that there is a slight increase in interfacial area after annealing the film at 137°C with small pure domains formed but not as drastic as after annealing at 175°C. Therefore, there should be an improvement in the efficiency of exciton diffusion and charge separation. As there is an increase in almost all the parameters, the overall efficiency of our devices will increase after annealing, which is seen.

The efficiency of the device for annealing at 137°C was expected to improve the morphology of the active layer and therefore improve the efficiency of our devices. The main reasons the PCE was expected to increase was through an increased extent of crystallinity[14, 48], as seen from Figure 6.2. In this study, it is seen that the efficiency of our devices was improved mainly due to the vast increase in the fill factor and V_{OC}. As we know, crystallinity is important in our film to improve mobility and exciton diffusion. Through thermal annealing, SQ aggregation (Figure 6.3) was enabled. Through the XRD data and TEM images we note that annealing the film at low temperature, we can increase the crystallinity without phase separation.

As seen from this study, the morphology of our devices directly impacts the efficiency of our devices. The optimum morphology in our device is accomplished by 1) high fullerene content to take full advantage of mixing during spin coating and 2) annealing the film at a low temperature to achieve well mixed and small domain size of donor and acceptor phase, so that the charges can be collected more efficiently[39]. This can further be studied by looking at solvent vapor annealing to achieve mixed and small domain size of donor and acceptor phase.

Chapter 7 : Controlling Phase Separation with Solvent Vapor Annealing

7.1 Introduction

As we have seen in the previous chapter, thermal annealing has improved charge transport and charge separation efficiency. Limitations of thermal annealing like large phase separation can be unfavorable for devices. Large PCBM aggregation has been shown to exceed the diffusion length of the exciton leading to charge recombination[48, 51]. Studies have also shown that the high temperature of thermal annealing could damage the material and the flexible substrates in large scale manufacturing[52].

Therefore, in this chapter solvent vapor annealing will be used to control the morphology of the active layer. Solvent vapor annealing is a technique where the device is exposed to solvent vapor (Figure 7.1). This solvent vapor will diffuse into the active layer, and enable arrange the molecules to find a more favorable arrangement. The exposure time and choice of solvent is critical as that's what controls the extent of aggregation[53].

Previous studies on P3HT/PCBM devices have shown that solvent vapor annealing leads to the formation of mesoscopic PCBM crystallites which improves the electron transporting domains[54] and this was also found to increase light absorption and improve photocurrent[54, 55]. Verploegen *et al.* found that solvent vapor annealing leads to smaller phase separation domains compared to thermal annealing at a temp 130°C[56]. It was also observed by Verploegen *et al.* that solvent vapor annealing shows more favorable π–π stacking perpendicular to the substrate, which is more favorable for charge transport than parallel π–π stacking direction, which is seen in thermal annealing for P3HT/PCBM studies[48, 56]. In another study, previously done for a SQ:PC$_{71}$BM (1:6) by Forrest *et al.* it was found that by using a Dichloromethane (DCM) solvent vapor annealing controlled phase separation. An increase in power conversion efficiency is achieved when the exciton diffusion length is equal to domain size. It was seen that the optimum morphology takes advantage of the high

absorption coefficient, with small diffusion length for SQ compounds, which allows devices with SQ at low concentration, to result in high solar cell efficiency[57].

7.2 Experimental

UV-Vis absorbance

For UV-Vis absorbance measurements thin film samples were prepared by spin casting the active layer (1500 rpm for 18 seconds) from blended SQ:PCBM chloroform solutions (the same as for device preparation) onto glass substrates cut from microscope slides. A Shimadzu UV-2401 spectrophotometer was used for absorption characterization. Setting of medium scan speed, 0.5 nm increments and 2 nm slit width were applied when taking the measurements. Absorbance data from these samples were then recorded from a wavelength of 300 nm to 900 nm. A blank glass slide was used to baseline the spectrum to account for scattering and absorption of substrates. Three measurements were taken for each film by changing the film position in the light path to account for any heterogeneity in the films.

Transmission electron microscopy (TEM)

TEM measurements of the SQ:PCBM films were obtained using a JEOL JEM-2010 operating at 200 kV with a 210 LaB6 filament and an AMT image capture system. The average domain size was quantified using ImageJ software. The measured $DHSQ(OH)_2$:$PC_{61}BM$ blend films were prepared using the same method as described in the UV-Vis section. Three films were prepared for each blend ratio; un-annealed, solvent annealed for 5, 10 and 40 minutes respectively. Films were prepared by dipping spin-cast films into water, which separated the film from the substrate. The

films were then placed onto copper TEM grids covered with an amorphous carbon film. The water was allowed to evaporate under ambient conditions.

Device Fabrication

Eight precut Indium-tin-oxide (ITO) coated glass were used. The substrates were cleaned using acetone and IPA under sonication conditions. Then the substrates were rinsed in a hot water bath and sonicated in sodium hydroxide. A strip at the top of each substrate was taped to protect the ITO – anode from deposition of the active layer. The PEDOT:PSS buffer layer was spin-coated at a spin speed of 5000 rpm for 40 seconds before being left in the vacuum oven (150°C) for an hour. The substrates were then transferred into a nitrogen-filled glove box system where the active solar cell layer was spin-coated (1500 rpm for 18 seconds) from chloroform solutions. The solution of fixed concentration of $DHSQ(OH)_2$ to 4 mg/ml and varying concentration of PCBM corresponding to the blend ratio. One half of the substrates were solvent annealed for 5, 10, 20 and 40 minutes respectively and then transferred directly into high vacuum. Then the aluminum electrode was thermally evaporated through a shadow mask giving four solar cells with an area of approximately ~29 mm^2 for every sample.

J-V measurement

The J-V measurements were performed using a Newport solar simulator with a power density of 100 mW cm^{-2} (1-sun illumination). The OPV devices were tested immediately after fabrication by a four-point probe method. The out bias was scanned from -2 Volts to 2 Volts with a 0.4 Volts-increment. The current density of the OPV devices (under 1-sun illumination) was measured, and the J-V curve was obtained by

measuring the current signal as a function of the voltage bias. The short-circuit current (J_{SC}), open-circuit voltage (V_{OC}) and fill factor (FF) were calculated by inserting the data into a calculating spreadsheet.

7.3 Results and Discussion

7.3.1 Absorbance
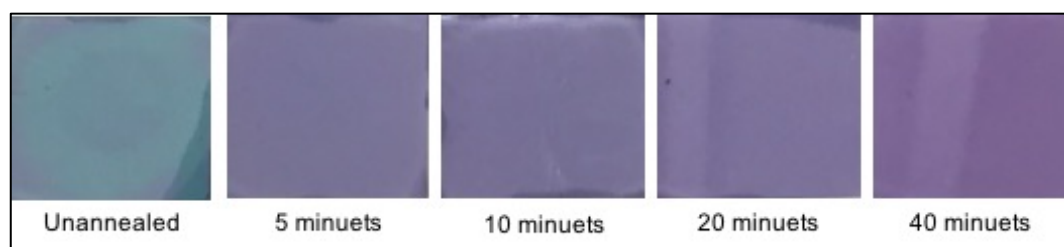
Figure 7.2: Picture of the color change of spin coated films of blended DHSQ(OH)$_2$:PC$_{61}$BM (1:3 w/w) solvent annealed in DCM for various times as noted above

The films were spin-coated on glass from the same chloroform solution as used for solar cell preparations. Figure 7.2 shows the color change of the films solvent annealed in DCM for various times, which is visible by eye. It can be seen that the unannealed film is blue in color and as the solvent annealing treatment was performed for various times the film turned purple. All UV-Vis absorption spectra are plotted in Figure 7.3.
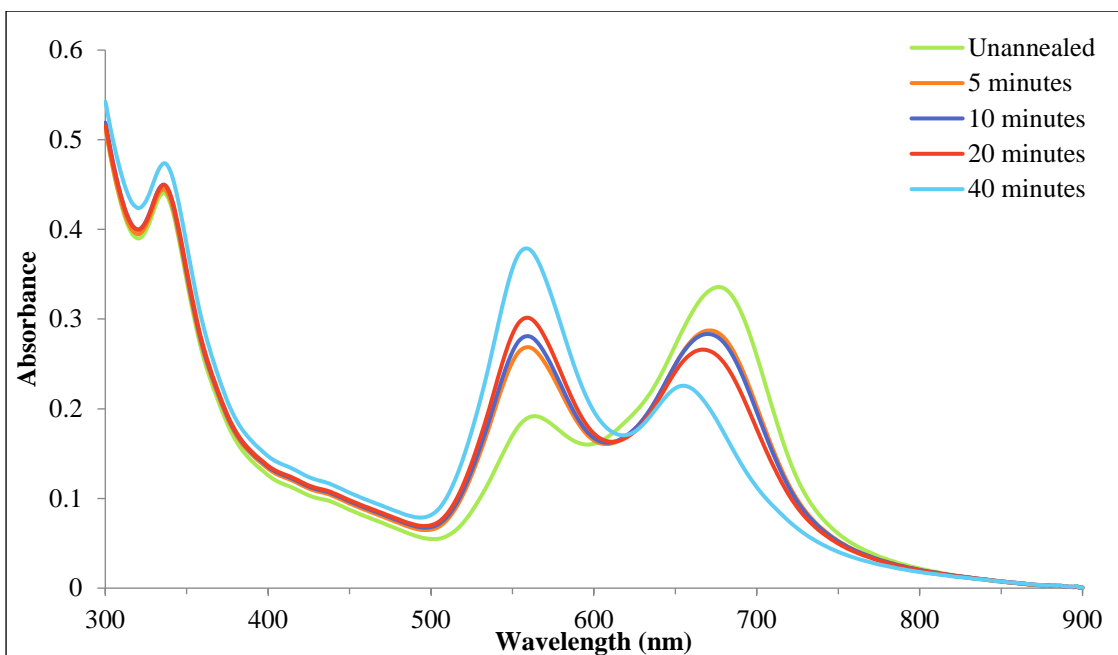
Figure 7.3: Absorbance spectra from spin-coated films of blends of DHSQ(OH)$_2$:PC$_{61}$BM (1:3 w/w) solvent annealed in DCM for various times as noted on the graph

Figure 7.3 shows the absorbance of DHSQ(OH)$_2$:PCBM blends before and after solvent annealing in DCM for various times as a function of wavelength. The peak at 320 nm in the blend ratio films is the absorbance of PC$_{61}$BM. The unannealed blend ratio films are compared to the annealed films to see how the aggregation changes when films are solvent annealed in DCM for various times. In this chapter, the only blend ratio that was studied was DHSQ(OH)$_2$: 75% PCBM, as this is seen to be the optimal blend ratio for this squaraine. For blend ratios 1:3, light green for unannealed, and the annealing times studied were 5 minutes (orange), 10 minutes (dark blue), 20 minutes (red) and 40 minutes (light blue). All these spectra show two absorbance maxima, aggregate (560 nm) and monomer peak mixed with the intermolecular charge transfer peak (660 nm). The 660 nm peak blue shifts as annealing time is increased (Figure 7.4), as said in chapter 3 this is due to the mixing of the ICT peak with the monomer peak.
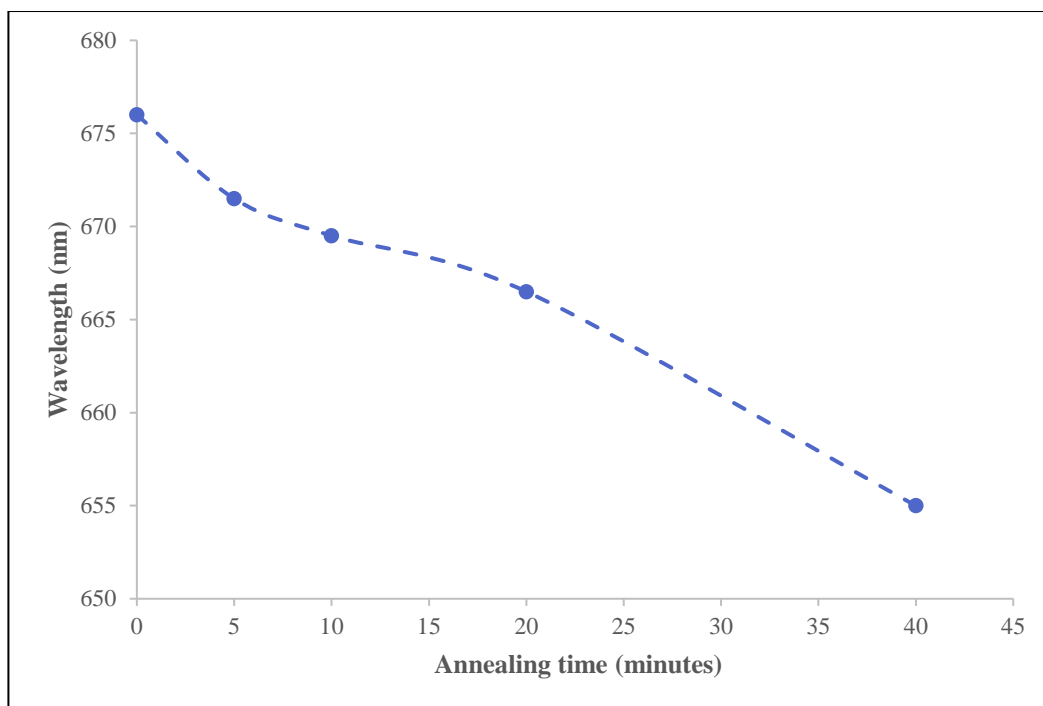
Figure 7.4: Shift in the low energy peak as a function of annealing time

When comparing the unannealed and the solvent annealed for 1:3 blend ratio (Figure 7.3), it can be seen there is a change in the spectra from unannealed and annealing at various times in DCM. It is mostly the intensity of the peaks that changes (Figure 7.5). It can be seen that as the films are annealed for longer, there is an increase in the population of species of the aggregate. This can also be seen by the color change from blue to purple in Figure 7.2.

As seen from the previous chapters and from Figure 7.3, it can be seen that for the unannealed sample (light green), there is a higher population of the monomer as evidenced by a higher monomer peak. The low energy peak is red shifted compare to the annealed spectrum (orange, dark blue, red and light blue) for this blend. When the films are annealed (orange, dark blue, red and light blue), it can be seen that the population of aggregate rapidly increases compared to that of the monomer, with the high energy peak at 560 nm increasing from 0.192 at 0 minutes to 0.379 at 40 minutes. The low energy peak at 660 nm decreases from 0.336 at 0 minutes to 0.226

110

at 40 minutes. When comparing the annealed spectra with each other, annealing for 5 minutes (orange) there is an increase in the intensity of then aggregate peak (from 0.192 to 0.269 respectively) compared to the unannealed (light green) and a decrease in the low energy peak (0.336 to 0.287 respectively). There isn't much difference seen in the spectra for solvent annealing for 5 minutes (orange), solvent annealing for 10 minutes (dark blue), and solvent annealing at 20 minutes (red). Although there is a drastic change in the peak intensities when the films were solvent annealed for 40 minutes (light blue), for the peak at 560 nm there is an increase from 0.302 at 20 minutes of solvent annealing to 0.379 at 40 minutes of solvent annealing and the peak at 660 nm decreases from 0.266 at 20 minutes of solvent annealing to 0.226 at 40 minutes of solvent annealing. From Figure 7.5, it can be seen like a two-step mechanism, where the SQ molecule starts to aggregate and then between 5 minutes to 10 minutes, where we don't see much change in the spectrum, phase separation takes place. Solvent annealing does give us a more controllable technique to affect the ratio of aggregate population: monomer population. As seen from Figure 7.3, there is a gradual increase in the population of aggregate intensity as annealing time is increased and a gradual decrease in the population of monomer as annealing time is increased (Figure 7.5).

We consider that solvent annealing is a more controllable technique than thermal annealing, but to confirm our hypothesis we need to further look at device results. Analysis of TEM images is also needed to understand the phase separation and domain size of our pure domains after annealing.
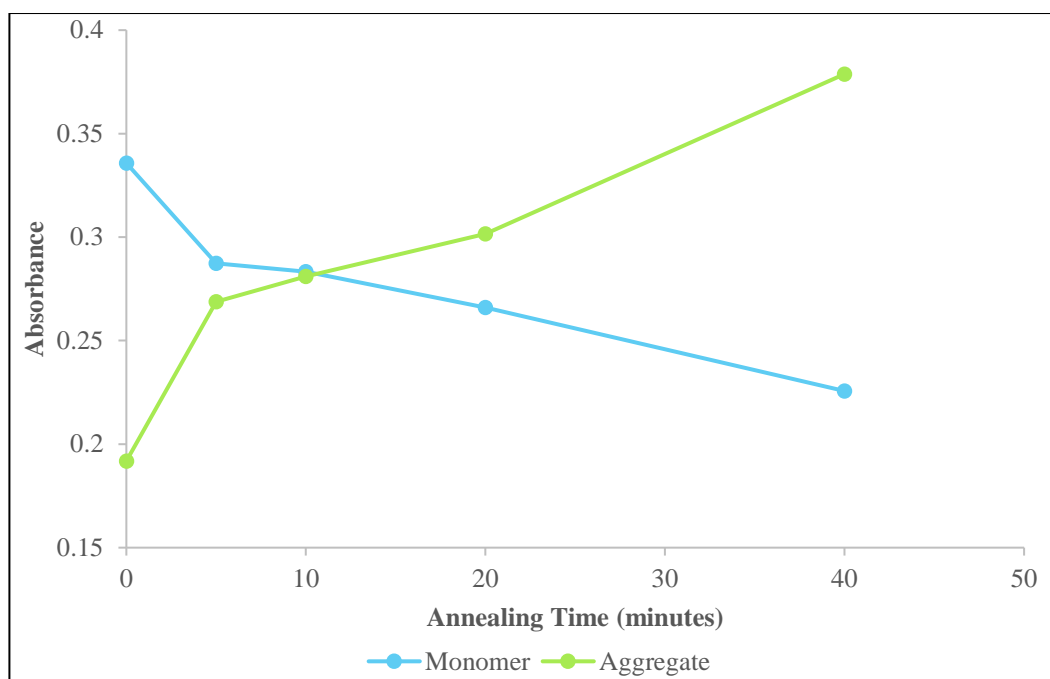
Figure 7.5: Absorbance of the monomer (blue), H- agg peak (green) and as a function of Wavelength (nm)

7.3.2 Device Data

Figure 7.6 shows the J-V curve measurements of DHSQ(OH)$_2$:PCBM (1:3 w/w) OPV devices before and after solvent annealing treatment for various times. The shape of the J-V curve demonstrates a successful device (with an average efficiency of 1.03% for blend ratio 1:3 for as-cast devices). It should be noted that these devices are un-optimized (as there is no electron transporting layer or using PC$_{61}$BM rather than PC$_{71}$BM). The solvent annealing treatment in DCM was performed on the devices, and the efficiency increased to 1.41% for blend ratio 1:3. From Figure 7.6, it can be seen that the low slope at the J$_{SC}$ is likely associated with a low shunt resistance, which means there is current loss due to leakages across the junction. More detailed device parameters are listed in Table 7.1 below.

112

Figure 7.6: Summarized J-V curve measurement for DHSQ(OH)$_2$:PC$_{61}$BM (1:3 w/w) blended devices before and after solvent annealing in DMC for various times

The solar cell had the layer arrangement of

ITO/PEDOT:PSS/DHSQ(OH)$_2$:PC$_{61}$BM/Al.

Table 7.1: Shows the Device data for blend ratio 1:3 with and without solvent annealing in DCM at various times. Values and error for PCE, V_{OC}, J_{SC} and FF reported here are averages obtained by testing a group of 16 devices for each point.

DHSQ(OH)$_2$:PCBM	Solvent Annealing treatment	Device Parameters			
		J_{SC} (mAcm^{-2})	V_{OC} (V)	FF	PCE
1:3	none	3.97 ± 0.39	0.65 ± 0.02	39.27% ± 2.08%	1.03% ± 0.18%
	5 minutes	4.35 ± 0.63	0.67 ± 0.09	39.58% ± 4.19%	1.19% ± 0.35%
	10 minutes	4.42± 0.59	0.71 ± 0.04	38.91% ± 5.34%	1.22% ± 0.24%[a]
	20 minutes	3.74± 0.40	0.75 ± 0.04	45.80% ± 3.80%	1.28% ± 0.11%
	40 minutes	3.88 ± 0.22	0.82 ± 0.02	44.22% ± 3.21%	1.41% ± 0.16%

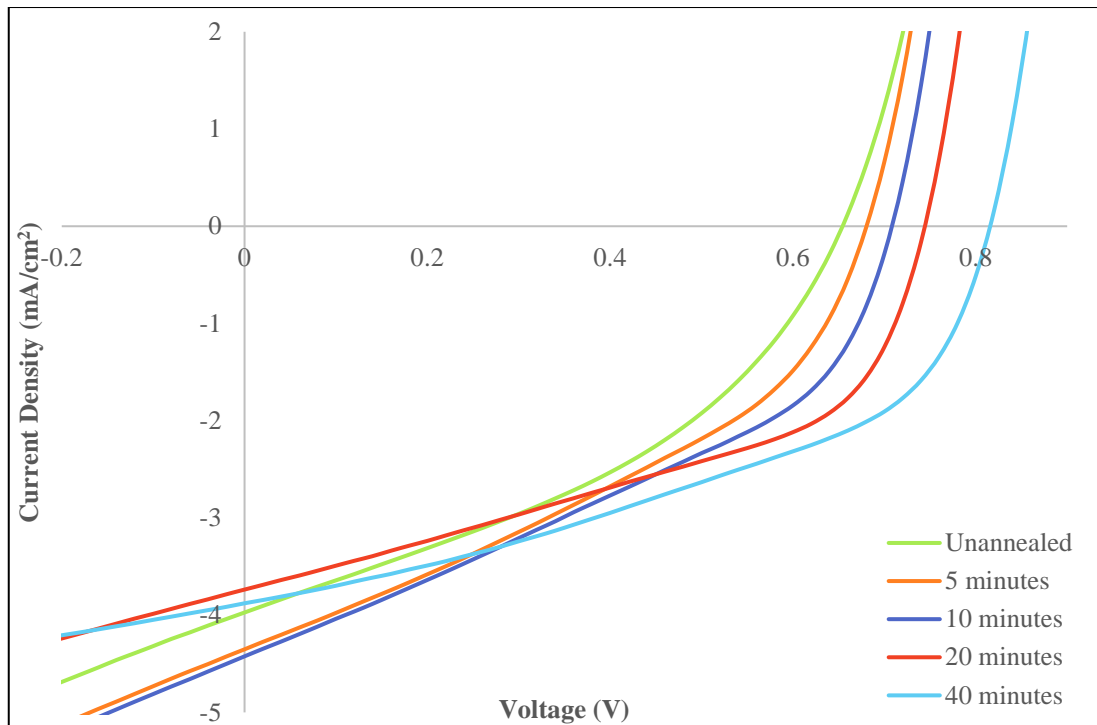Table 7.1 shows the device parameters of DHSQ(OH)$_2$:PCBM (1:3 w/w) with and without solvent annealing in DCM for various times. Again, it is important to remember that these devices are not completely optimized as described in chapter 6.

In this study, it is seen that the longer the devices are solvent annealed, the higher the efficiency; the highest efficiency seen is 1.41% for devices exposed to solvent vapor for 40 minutes. This increase is mainly due to the vast improvement in the open circuit voltage and the fill factor as solvent annealing time is increased. The short circuit current increases from 3.97 mAcm^{-2} with no annealing treatment to 4.42 mAcm^{-2} with 10 minutes of solvent annealing and then decreases to 3.88 mAcm^{-2} with 40 minutes of solvent annealing. When these films are annealed they form highly ordered crystals. This leads to enhanced exciton diffusion rates and in a more efficient charge transfer due to better overlap of frontier orbitals[14]. Hence this improves charge mobility and reduces non-geminate recombination of charges. The open circuit

voltage and fill factor was substantially enhanced as from 0.65 V and 39.27% (as cast) to 0.82 V and 44.22% after 40 minutes exposure to DCM. As we already know that the V_{OC} is related to the offset of the HOMO of the donor and LUMO of the acceptor at the interface. But by looking at the absorbance spectrum (Figure 7.3), it can be seen that there is an increase in the population of the aggregate species compared to the monomer for this blend. Which suggests there is a slight change in the energetics at the SQ and PCBM interface. But as there is more population of the aggregate species, therefore there will be an increase in the HOMO energy level of the donor as seen in Figure 1.15, this should cause a decrease in the V_{OC}. Therefore, this increase in the V_{OC}, is mainly due to a there being a decrease in non-geminate recombination as we expect solvent annealing will increase crystallinity while having smaller domain sizes. The decrease in recombination is the main reason in the significant increase in Fill factor. This is due to the increase in the interface between the SQ and PCBM, as the phases are well mixed therefore the mobility are balanced[50], so the charges can be collected without rcombining[39]. Therefore, to look at phase separation we need to look at the TEM images to understand the morphology change and phase domains sizes due to annealing.

115

7.3.2 Transmission Electron Microscopy
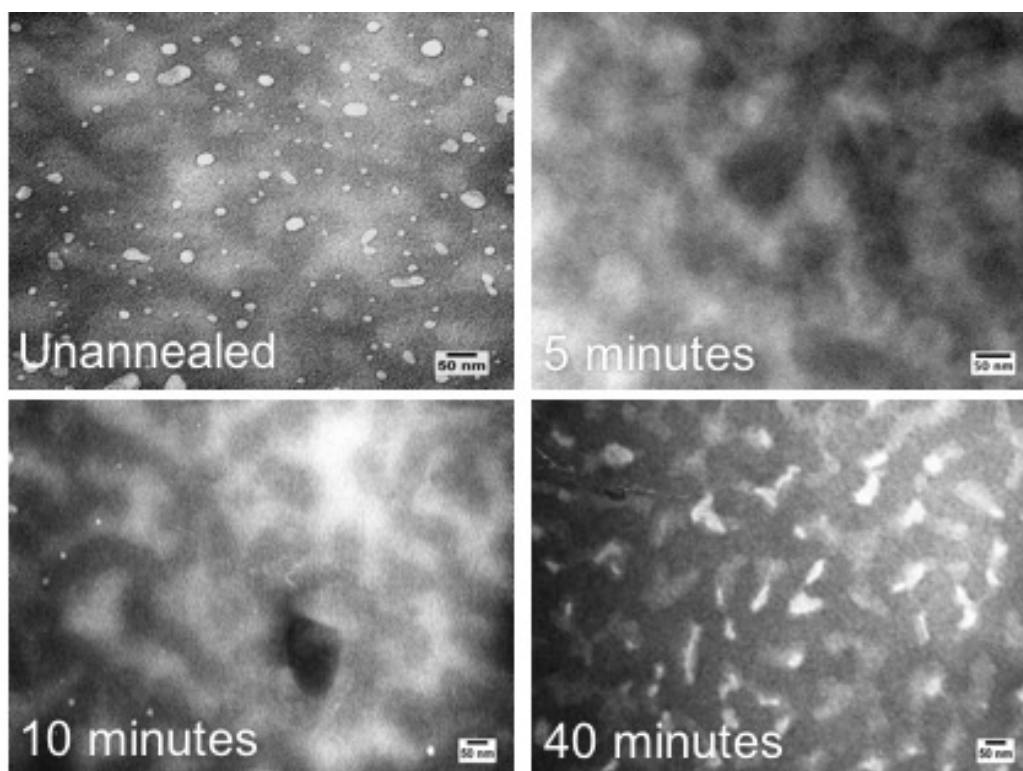
Figure 7.7: Shows TEM images of spin-cast DHSQ(OH)$_2$:PC$_{61}$BM films (1:3 w/w) without treatment (top left), solvent annealed in DCM for 5 minutes (top right), solvent annealed in DCM for 10 minutes (bottom left) and solvent annealed in DCM for 40 minutes (bottom right). The scale bar at the bottom of each image is 50 nm. The dark regions are the PCBM domains and the lighter region are the SQ domains.

To study the phase separation in our active layer, transmission electron microscopy (TEM) was used (Figure 7.7). Figure 7.7 shows the TEM images DHSQ(OH)$_2$:PCBM film without annealing and with solvent annealing in DCM for varying time, for blend ratio 1:3 DHSQ(OH)$_2$:PCBM. The 1:3 DHSQ(OH)$_2$:PCBM, has much small and finer phases formed with an estimated size of 100 nm. This is in agreement with our absorbance spectra (Figure 7.3). As the content of PCBM is increased there is a decrease in the SQ aggregation compared to monomer but there is still some population of aggregate. Therefore, as seen from TEM data there are

crystalline domains formed but they are smaller in size, which means the heterojunction interface increases. From solvent annealing in DCM it can be seen that the phase separation becomes more defined as the annealing time is increased. The estimated domain size increases slightly as annealing time is increased, from 100 to 150 nm at 40 minutes of solvent annealing. There was an increase in the aggregate absorption in the UV-vis spectra (Figure 7.3) after solvent annealing. Therefore, we assume there is also an increase in the extent of crystallinity. All of these small morphological features lead to a decrease in the recombination of charges and exciton diffusion length that is approximately equal to the mean SQ domain size, which leads to an increase in device performance. Therefore, we can see that choosing solvent annealing achieves precise structural control to take advantage of the high absorption coefficient yet small diffusion length characteristic of this squaraine compound, allowing for low concentration SQ in the active layer that leads to higher OPV device results.

7.4 Conclusion

In the last chapter, we saw that thermal annealing is critical for morphology but the phase separation is not easily controllable. In this chapter, we have optimized our devices by understanding how solvent annealing affects the morphology of our devices. It was found that solvent annealing in DCM for 40 minutes showed an enhancement in our efficacy from 1.03% to 1.41% for 1:3 DHSQ(OH)$_2$:PCBM blends.

From Figure 7.3, we can see that as we solvent annealing the film in DCM, there is an increase in the population of the aggregate spices and a decrease in the monomer population. Therefore, there is a loss in absorption, as we are losing the

absorption of photon near the near IR region of the spectrum. Due to this loss, there should be a slight decrease in the J_{SC} for the devices after solvent annealing (Table 7.1). The charge transfer should increase after annealing, as the SQ molecules are mainly aggregated; therefore, we infer that the charge mobility will be increase. There is an improvement in charge collection for these devices after solvent annealing, as if we look at the TEM images (Figure 7.7), we can note that there is smaller pure domain formed, therefore there should be a decrease in non-geminate recombination and we should get efficient charge collection. The exciton diffusion and charge separation are based on the interfacial area between the pure donor domain and pure acceptor domain in the active layer. From the TEM images, we can see that there is a slight increase in interfacial area after solvent annealing with small pure domains formed. Therefore, there should be an improvement in the efficiency of exciton diffusion and charge separation. As there is an increase in all most all the parameter, which should result in an overall increase in efficiency of our devices will after annealing which is seen.

Solvent annealing was expected to improve the morphology of the active layer and therefore improve the efficiency of our devices. The main reasons the PCE was expected to increase due to annealing induces the SQ to orient in a more ordered aggregated packing which results in an increase in the extent of crystallinity[14, 48]. In this study, it is seen that the efficiency of our device was improved mainly due to the vast increase in the fill factor and V_{OC}. As we know crystallinity is important in our film to improve mobility and exciton diffusion. Through Solvent annealing allowed SQ aggregation (Figure 7.3), through the TEM images (Figure 7.7) we note that solvent annealing the film in DCM allows for precise structural control to take

advantage of the high extinction coefficient and still have small diffusion length character that SQ exhibit without let SQ molecule phase separate.

As seen from this study, that morphology of a device directly impacts the efficiency. The optimum morphology in our device is accomplished by 1) high fullerene content to take full advantage of mixing during spin coating and 2) solvent annealing the film to achieve well mixed and small domain size of donor and acceptor phase, so that the charges can be collected more efficiently[39].

Chapter 8 : Conclusion and Further Work

In this work, we have understood how aggregation and crystallinity affects our devices. The presence of aggregates and crystallinity create many ways that charge photo generation is changed. Absorbance may be negatively impacted by aggregates as there is a loss of absorbance in the NIR. Exciton diffusion is not influenced by the formation of aggregate, but is significantly increased with increasing crystallinity of the donor. Exciton dissociation and charge transfer will be enhanced with increased crystallinity as there would be more efficient frontier orbital overlap. Lastly, charge collection is not affected by aggregates, but crystallinity can play a significant difference when compared to amorphous regions due to the fact that charge mobility is increase when there are crystalline domains. As there is an enhancement in almost all these parameters, our device should result in higher PCE. We were also able to enable an interconversion of monomers to aggregates through annealing technique (solvent vapor or thermal annealing). X-ray diffraction analysis of annealed films shows an increase in crystallinity, but often at the cost of larger crystal size as shown in the TEM images. The over-grown crystal domains largely seem detrimental in device performance when the blended SQ:$PC_{61}BM$ films were annealed at high temperature. We were able to better control this phase separation and domain size by solvent annealing, as solvent annealing results in a 40% increase in overall PCE, whereas thermal annealing at 137°C resulted in a 26% increase in PCE. Therefore, it is seen that the optimal device performance is achieved by 1) maintaining high fullerene content to maximize mixing during the spin casting and 2) solvent annealing the film a sufficient amount of time such that crystallinity is increased without initiating phase separation.

In the future, it would be interesting to see how the SQ could be used in a ternary blend study. As seen in chapter 4, SQ result higher PCE, at low concentration, therefore instead of using PCBM to disrupt the aggregation we could use a different SQ. Therefore, it is assumed that when there is a mixture of squaraines, they may not crystallize. But there would still be pure squaraine phase which will phase separate from the pure PCBM phase. There may also be increase in the absorbance leading to an increase in the number of resulting excited states that are converted into dissociated charges are increased, which then subsequently enhance short circuit current (J_{SC}). Which will enhance the efficiency of the OPV devices.

References

1. Darling, S. B.; You, F., The case for organic photovoltaics. *Rsc Advances* **2013,** *3* (39), 17633-17648.
2. Li, C.; Liu, M.; Pschirer, N. G.; Baumgarten, M.; Müllen, K., Polyphenylene-based materials for organic photovoltaics. *Chemical reviews* **2010,** *110* (11), 6817-6855.
3. Chen, G.; Sasabe, H.; Igarashi, T.; Hong, Z.; Kido, J., Squaraine dyes for organic photovoltaic cells. *Journal of Materials Chemistry A* **2015,** *3* (28), 14517-14534.
4. Brabec, C. J.; Heeney, M.; McCulloch, I.; Nelson, J., Influence of blend microstructure on bulk heterojunction organic photovoltaic performance. *Chemical Society Reviews* **2011,** *40* (3), 1185-1199.
5. Steim, R.; Kogler, F. R.; Brabec, C. J., Interface materials for organic solar cells. *Journal of Materials Chemistry* **2010,** *20* (13), 2499-2512.
6. Günes, S.; Neugebauer, H.; Sariciftci, N. S., Conjugated polymer-based organic solar cells. *Chemical reviews* **2007,** *107* (4), 1324-1338.
7. Ayzner, A. L.; Tassone, C. J.; Tolbert, S. H.; Schwartz, B. J., Reappraising the need for bulk heterojunctions in polymer− fullerene photovoltaics: the role of carrier transport in all-solution-processed P3HT/PCBM bilayer solar cells. *The Journal of Physical Chemistry C* **2009,** *113* (46), 20050-20060.
8. Erb, T.; Zhokhavets, U.; Gobsch, G.; Raleva, S.; Stühn, B.; Schilinsky, P.; Waldauf, C.; Brabec, C. J., Correlation between structural and optical properties of composite polymer/fullerene films for organic solar cells. *Advanced Functional Materials* **2005,** *15* (7), 1193-1196.
9. Walker, B.; Tamayo, A. B.; Dang, X.-D.; Zalar, P.; Seo, J. H.; Garcia, A.; Tantiwiwat, M.; Nguyen, T.-Q., Nanoscale Phase Separation and High Photovoltaic Efficiency in Solution-Processed, Small-Molecule Bulk Heterojunction Solar Cells. *Advanced Functional Materials* **2009,** *19* (19), 3063-3069.
10. Spencer, S. D.; Bougher, C.; Heaphy, P. J.; Murcia, V. M.; Gallivan, C. P.; Monfette, A.; Andersen, J. D.; Cody, J. A.; Conrad, B. R.; Collison, C. J., The effect of controllable thin film crystal growth on the aggregation of a novel high panchromaticity squaraine viable for organic solar cells. *Solar Energy Materials and Solar Cells* **2013,** *112*, 202-208.
11. Spencer, S.; Hu, H.; Li, Q.; Ahn, H. Y.; Qaddoura, M.; Yao, S.; Ioannidis, A.; Belfield, K.; Collison, C. J., Controlling J-aggregate formation for increased short-circuit current and power conversion efficiency with a squaraine donor. *Progress in Photovoltaics: Research and Applications* **2014,** *22* (4), 488-493.
12. Spencer, S.; Cody, J.; Misture, S.; Cona, B.; Heaphy, P.; Rumbles, G.; Andersen, J.; Collison, C., Critical Electron Transfer Rates for Exciton Dissociation Governed by Extent of Crystallinity in Small Molecule Organic Photovoltaics. *The Journal of Physical Chemistry C* **2014,** *118* (27), 14840-14847.

13. Zheng, C.; Penmetcha, A. R.; Cona, B.; Spencer, S.; Zhu, B.; Heaphy, P.; Cody, J. A.; Collison, C. J., The contribution of aggregate states and energetic disorder to a squaraine system targeted for organic photovoltaic devices. *Langmuir* **2015**.

14. Zheng, C.; Bleier, D.; Jalan, I.; Pristash, S.; Penmetcha, A. R.; Hestand, N. J.; Spano, F. C.; Pierce, M. S.; Cody, J. A.; Collison, C. J., Phase separation, crystallinity and monomer-aggregate population control in solution processed small molecule solar cells. *Solar Energy Materials and Solar Cells* **2016,** *157*, 366-376.

15. Scharber, M. C.; Mühlbacher, D.; Koppe, M.; Denk, P.; Waldauf, C.; Heeger, A. J.; Brabec, C. J., Design rules for donors in bulk-heterojunction solar cells—Towards 10% energy-conversion efficiency. *Advanced materials* **2006,** *18* (6), 789-794.

16. Li, G.; Shrotriya, V.; Huang, J.; Yao, Y.; Moriarty, T.; Emery, K.; Yang, Y., High-efficiency solution processable polymer photovoltaic cells by self-organization of polymer blends. *Nature materials* **2005,** *4* (11), 864-868.

17. Dennler, G.; Scharber, M. C.; Brabec, C. J., Polymer-Fullerene bulk-heterojunction solar cells. *Advanced Materials* **2009,** *21* (13), 1323-1338.

18. Kaur, N.; Singh, M.; Pathak, D.; Wagner, T.; Nunzi, J., Organic materials for photovoltaic applications: Review and mechanism. *Synthetic Metals* **2014,** *190*, 20-26.

19. Heeger, A. J., 25th anniversary article: bulk heterojunction solar cells: understanding the mechanism of operation. *Advanced Materials* **2014,** *26* (1), 10-28.

20. Forrest, S. R., The limits to organic photovoltaic cell efficiency. *MRS bulletin* **2005,** *30* (01), 28-32.

21. Siddiki, M. K.; Li, J.; Galipeau, D.; Qiao, Q., A review of polymer multijunction solar cells. *Energy & Environmental Science* **2010,** *3* (7), 867-883.

22. Robertson, N., Organic Photovoltaics. Mechanisms, Materials and Devices. Edited by Sam-Shajing Sun and Niyazi Serdar Sariciftci. *Angewandte Chemie International Edition* **2006,** *45* (44), 7321-7321.

23. Servaites, J. D.; Yeganeh, S.; Marks, T. J.; Ratner, M. A., Efficiency enhancement in organic photovoltaic cells: consequences of optimizing series resistance. *Advanced Functional Materials* **2010,** *20* (1), 97-104.

24. Tress, W.; SpringerLink (Online service), Organic Solar Cells Theory, Experiment, and Device Simulation. In *Springer Series in Materials Science,* [Online]; pp. XX, 464 p. 208 illus., 182 illus. in color. Springer Electronic Books https://ezproxy.rit.edu/login?url=http://dx.doi.org/10.1007/978-3-319-10097-5.

25. Zekry, Z.; Eldallal, G., Effect of MS contact on the electrical behaviour of solar cells. *Solid-state electronics* **1988,** *31* (1), 91-97.

26. Servaites, J. D.; Ratner, M. A.; Marks, T. J., Organic solar cells: a new look at traditional models. *Energy & Environmental Science* **2011,** *4* (11), 4410-4422.

27. Credgington, D.; Jamieson, F. C.; Walker, B.; Nguyen, T. Q.; Durrant, J. R., Quantification of Geminate and Non-Geminate Recombination Losses within a

Solution-Processed Small-Molecule Bulk Heterojunction Solar Cell. *Advanced Materials* **2012,** *24* (16), 2135-2141.

28. Street, R.; Schoendorf, M.; Roy, A.; Lee, J., Interface state recombination in organic solar cells. *Physical Review B* **2010,** *81* (20), 205307.

29. Gilbert, A.; Baggott, J. E., *Essentials of molecular photochemistry*. CRC: 1991.

30. Beverina, L.; Salice, P., Squaraine compounds: Tailored design and synthesis towards a variety of material science applications. *European journal of organic chemistry* **2010,** *2010* (7), 1207-1225.

31. Zhou, J.; Zuo, Y.; Wan, X.; Long, G.; Zhang, Q.; Ni, W.; Liu, Y.; Li, Z.; He, G.; Li, C., Solution-processed and high-performance organic solar cells using small molecules with a benzodithiophene unit. *Journal of the American Chemical Society* **2013,** *135* (23), 8484-8487.

32. Ajayaghosh, A., Chemistry of squaraine-derived materials: near-IR dyes, low band gap systems, and cation sensors. *Accounts of Chemical Research* **2005,** *38* (6), 449-459.

33. Padinger, F.; Rittberger, R. S.; Sariciftci, N. S., Effects of postproduction treatment on plastic solar cells. *Advanced Functional Materials* **2003,** *13* (1), 85-88.

34. Paek, S.; Choi, H.; Kim, C.; Cho, N.; So, S.; Song, K.; Nazeeruddin, M. K.; Ko, J., Efficient and stable panchromatic squaraine dyes for dye-sensitized solar cells. *Chemical Communications* **2011,** *47* (10), 2874-2876.

35. Mazzio, K. A.; Luscombe, C. K., The future of organic photovoltaics. *Chemical Society Reviews* **2015,** *44* (1), 78-90.

36. Walker, B.; Kim, C.; Nguyen, T.-Q., Small molecule solution-processed bulk heterojunction solar cells†. *Chemistry of Materials* **2010,** *23* (3), 470-482.

37. Sinka, J., Collison Group Communication (Unpublished data).

38. Kasha, M.; Rawls, H.; Ashraf El-Bayoumi, M., The exciton model in molecular spectroscopy. *Pure and Applied Chemistry* **1965,** *11* (3-4), 371-392.

39. Mukherjee, S.; Proctor, C. M.; Tumbleston, J. R.; Bazan, G. C.; Nguyen, T. Q.; Ade, H., Importance of Domain Purity and Molecular Packing in Efficient Solution-Processed Small-Molecule Solar Cells. *Advanced Materials* **2015,** *27* (6), 1105-1111.

40. Lin, Y.; Li, Y.; Zhan, X., Small molecule semiconductors for high-efficiency organic photovoltaics. *Chemical Society Reviews* **2012,** *41* (11), 4245-4272.

41. Brück, S.; Krause, C.; Turrisi, R.; Beverina, L.; Wilken, S.; Saak, W.; Lützen, A.; Borchert, H.; Schiek, M.; Parisi, J., Structure–property relationship of anilino-squaraines in organic solar cells. *Physical Chemistry Chemical Physics* **2014,** *16* (3), 1067-1077.

42. Hestand, N. J.; Zheng, C.; Penmetcha, A. R.; Cona, B.; Cody, J. A.; Spano, F. C.; Collison, C. J., Confirmation of the Origins of Panchromatic Spectra in Squaraine Thin Films Targeted for Organic Photovoltaic Devices. *The Journal of Physical Chemistry C* **2015,** *119* (33), 18964-18974.

43. Rand, B. P.; Richter, H., *Organic Solar Cells: fundamentals, devices, and upscaling*. Pan Stanford Publishing: 2014.

44. Reiter, G., Dewetting of thin polymer films. *Physical Review Letters* **1992,** *68* (1), 75.

45. Wei, G.; Xiao, X.; Wang, S.; Sun, K.; Bergemann, K. J.; Thompson, M. E.; Forrest, S. R., Functionalized squaraine donors for nanocrystalline organic photovoltaics. *ACS nano* **2011,** *6* (1), 972-978.

46. Madigan, C.; Bulović, V., Modeling of exciton diffusion in amorphous organic thin films. *Physical review letters* **2006,** *96* (4), 046404.

47. Bansal, N.; Reynolds, L. X.; MacLachlan, A.; Lutz, T.; Ashraf, R. S.; Zhang, W.; Nielsen, C. B.; McCulloch, I.; Rebois, D. G.; Kirchartz, T., Influence of crystallinity and energetics on charge separation in polymer–inorganic nanocomposite films for solar cells. *Scientific reports* **2013,** *3*, 1531.

48. Yu, J.; Zheng, Y.; Huang, J., Towards High Performance Organic Photovoltaic Cells: A Review of Recent Development in Organic Photovoltaics. *Polymers* **2014,** *6* (9), 2473.

49. Wang, J.-L.; Liu, K.-K.; Yan, J.; Wu, Z.; Liu, F.; Xiao, F.; Chang, Z.-F.; Wu, H.-B.; Cao, Y.; Russell, T. P., A Series of Multifluorine Substituted Oligomers for Organic Solar Cells with Efficiency over 9% and Fill Factor of 0.77 by Combination Thermal and Solvent Vapor Annealing. *Journal of the American Chemical Society* **2016**.

50. Müller, C.; Ferenczi, T. A.; Campoy-Quiles, M.; Frost, J. M.; Bradley, D. D.; Smith, P.; Stingelin-Stutzmann, N.; Nelson, J., Binary organic photovoltaic blends: a simple rationale for optimum compositions. *Advanced Materials* **2008,** *20* (18), 3510-3515.

51. Hoppe, H.; Sariciftci, N. S., Morphology of polymer/fullerene bulk heterojunction solar cells. *Journal of Materials Chemistry* **2006,** *16* (1), 45-61.

52. Tang, H.; Lu, G.; Li, L.; Li, J.; Wang, Y.; Yang, X., Precise construction of PCBM aggregates for polymer solar cells via multi-step controlled solvent vapor annealing. *Journal of Materials Chemistry* **2010,** *20* (4), 683-688.

53. Miller, S.; Fanchini, G.; Lin, Y.-Y.; Li, C.; Chen, C.-W.; Su, W.-F.; Chhowalla, M., Investigation of nanoscale morphological changes in organic photovoltaics during solvent vapor annealing. *Journal of materials chemistry* **2008,** *18* (3), 306-312.

54. Bull, T. A.; Pingree, L. S.; Jenekhe, S. A.; Ginger, D. S.; Luscombe, C. K., The role of mesoscopic PCBM crystallites in solvent vapor annealed copolymer solar cells. *ACS nano* **2009,** *3* (3), 627-636.

55. Nam, S.; Jang, J.; Cha, H.; Hwang, J.; An, T. K.; Park, S.; Park, C. E., Effects of direct solvent exposure on the nanoscale morphologies and electrical characteristics of PCBM-based transistors and photovoltaics. *Journal of Materials Chemistry* **2012,** *22* (12), 5543-5549.

56. Verploegen, E.; Miller, C. E.; Schmidt, K.; Bao, Z.; Toney, M. F., Manipulating the morphology of P3HT–PCBM bulk heterojunction blends with solvent vapor annealing. *Chemistry of Materials* **2012,** *24* (20), 3923-3931.

57. Wei, G.; Wang, S.; Sun, K.; Thompson, M. E.; Forrest, S. R., Solvent-Annealed crystalline squaraine: PC70BM (1: 6) solar Cells. *Advanced Energy Materials* **2011,** *1* (2), 184-187.

Appendix A: Standard Operation Procedures

Standard Operation Procedure for Cyclic Voltammetry by James Sinka

There are 4 important factors when considering an electrochemical cell for cyclic voltammetric analysis.

1) A proper reference material is essential for performing any useful CV. Take a material whose HOMO/LUMO levels or oxidation/reduction potentials are known and analyze it with your CV set-up. This allows you to know what currents are correlated to which electrochemical states of your material, base-lining your system. Ferrocene is a well-studied reference material for use in an organic system, and ferrocyanide is also a well-studied reference material used in aqueous systems.

2) The correct electrodes for the system, including the reference, counter, and working electrode, are required to perform CV. The electrodes are doing the electrochemical measurements, so using fully functioning electrodes is essential. Ag/AgCl is a commonly used reference electrode, and Pt wire is frequently used as a counter electrode. Selection of the working electrodes is based on the electrochemical window provided; however, for this application a glassy carbon electrode will suffice.

3) The solvent choice is important and depends on the composition of the analyte. For an aqueous analyte, water is almost always the solvent of choice; however, there are different solvents to pick from in an organic system. The organic solvent must obviously dissolve the analyte, but most organics can be used to

solvate the system. The solvent must be degassed to remove any oxygen present in the system. Oxygen will modify the voltage at which the analyte is oxidized or reduced, so the system must be kept under positive gas flow while measurements are being performed. Be sure that the solvent isn't too volatile, or the incoming gas will dry off all of the solvent.

4) The transfer of electrons in solution is necessary, so an additive to promote the conductivity is essential. An electrolyte is key to performing CV as it provides ions to the system for oxidation and reduction to occur. When searching for electrolytes, it is important to keep in mind purity, as impurities in the electrolyte solution will disrupt the accuracy of the measurements. I have used other publish papers (see references 3-5) to find what electrolyte to best pair with the solvent I used (acetonitrile), and then have selected the one with a high purity grade and low cost. In the case of my system I used tetrabutylammonium hexafluorophosphate (TAHP), due to its efficient cost and documented use for CV in PAPER.
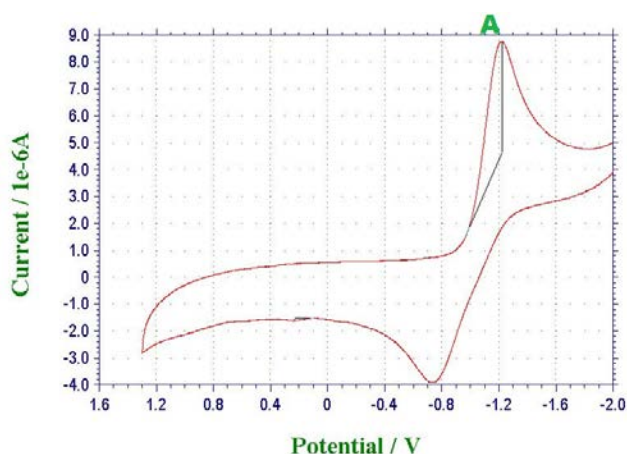

Figure A. 1: Shows a cyclic voltammagram of P3HT, an electron donating conjugated polymer. The oxidation peak of P3HT to P3HT⁻ is denoted with the letter A, at -1.22 volts.

Preparing the Solvent

Removing all impurities, such as oxygen and water, is very important when performing CV because they can negatively impact the results. Trace amounts of water can be removed by adding a solid drying agent, such as sodium sulfate; however, it should not be added to the electrolyte solution. As mentioned earlier, degassing the solvent using an inert gas such as argon or nitrogen is important so that the oxygen in solution is bubbled out. When working with argon, degassing simply involves connecting the argon line to the solution chamber and letting the gas bubble into the solution for 1 minute. At this point the gas must be removed from the solution, but there should still be positive pressure in the vessel such that no new oxygen can reenter. However, it is crucial to run the gas through a desiccator to remove trace water found in nitrogen gas. It is important to note that the system should be undisturbed, such that only the natural diffusion of charge through from the electrodes to the analyte is taking place. Movement of particles induced otherwise, for example through stirring, will alter the diffusion rate and change the reading of the system.

Setting-up the Experiment

Purity has been stressed throughout this guide, so be sure to thoroughly clean the vessel that will hold your electrochemical solution. Prepare a 0.2 molar solution of the electrolyte in the solvent of choice. Then degas the system for 1 minute, and leave a positive flow of gas for the duration of the experimentation. Add the electrodes to the system, and make sure they are wired properly or the analysis will fail. It is a good habit to perform a blank run of the electrolyte and solvent to make sure the system doesn't show any strange intense peaks, which would indicate the presence of an impurity.

A typical sweep range is from 2 to -2 volts, with a scan speed of 0.1V/s and a sample interval of 0.001V. The sensitivity of the system is very dependent on the concentration of the analyte, so tuning the sensitivity to your current set up is the most important part of getting a good reading with CV. A sensitivity of $1x10^{-7}$V/A is a good starting place, and you should modify it accordingly to highlight the peaks in the graphs. Changing the starting and ending voltages can also modify the sharpness of the peaks seen, so there will be some trial and error until the optimal configuration is found for the solution at hand.

Once the blank run(s) have been performed, your analyte can be added to the system. The added concentration of the analyte should never exceed 1/100 times that of the electrolyte. Run the potentiostat again, and remember that your sensitivity will likely need to be modified so the signals produced are detected. Be sure to record all the data, especially the peak position of the analyte as seen in Figure A. 1 above. It is a good idea to run the experiment three or more times and average the values, as they will increase the accuracy of the measurements. Now you are ready to add the internal standard material at a concentration of at least that of the analyte if not more. I personally add it at double the concentration to ensure I can see a spectral response upon addition. The reason the reference is added afterwards is because it could overlap with the peaks seen for your analyte, essentially downing them out. By adding it second, the data for the peak positions of the analyte have already been recorded and there is no chance for the standard to mask or alter the peak created. Once again, it is important to modify the experimental parameters such that a clear and optimized peak are observed for the internal standard. Be sure to take multiple readings that will be averaged to increase the accuracy of the results.

After all experimentation has been completed be sure to turn off the gas, properly dispose of the used materials, thoroughly clean the electrolytic solution vessel, and record all relevant data.

Data and Sample Calculation

The use of cyclic voltammetry in this paper is to calculate the HOMO/LUMO energy levels of organic materials used in OPV. A negative potential is applied by the working electrode to the point where an electron can transfer from the electrode to the LUMO orbital of the analyte. This transition is the first reduction potential peak as denoted by the letter A in Figure A. 1. Once the potential at which the Ferrocene/Ferrocyanide reference and the analyte are reduced, the HOMO/LUMO level can simply be calculated using the Equation A. 1;

$$\text{HOMO/LUMO} = [\ -E_{ox/red} - (4.8)]\ eV$$

<p align="center">Equation A. 1</p>

where $-E_{ox/red}$ is the reduction/oxidation potential of the analyte relative to ferrocene and 4.8 is the known HOMO value of ferrocene. We are essentially measuring the potential relative to ferrocene, and using it as our baseline because its HOMO level is well known. If the material is reduced at a potential that is greater than that of ferrocene, then the LUMO level will be higher than -4.8eV. Figure 2 below shows a sample calculation performed using Ferrocene and P3HT.
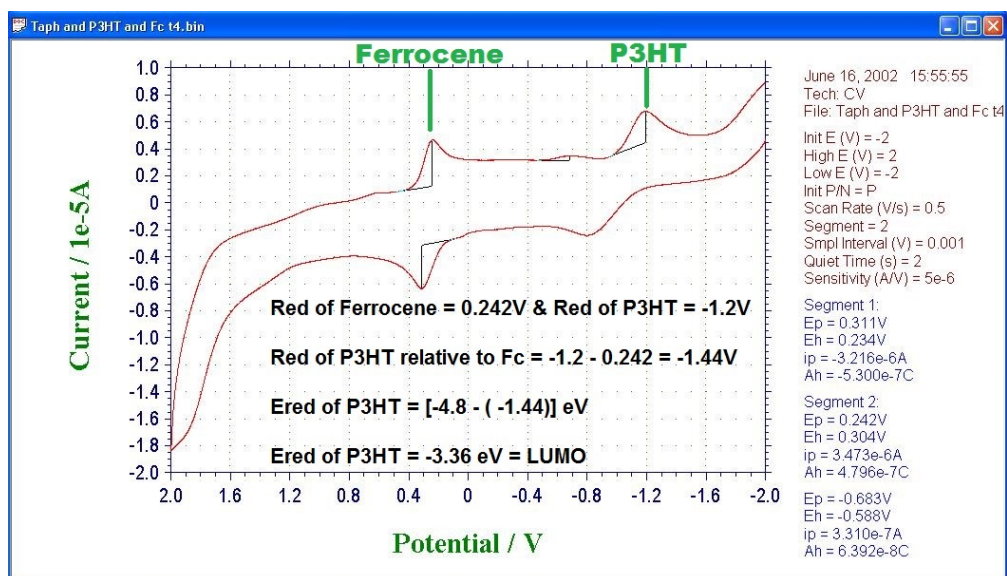
Figure A. 2: Shows a voltammagram of P3HT and Ferrocene, performed in acetonitrile with tetrabutylammonium hexafluorophosphate as the supporting electrolyte. Glassy carbon, Ag/AgCl, and a Pt wire were used as the working, reference, and counter electrodes respectively. Included is a sample calculation performed using the formula provided above

Appendix B: Theoretical J$_{SC}$ Calculations

For the theoretical J$_{SC}$ Calculation we used the ASTM G173-03 Reference spectra Derived from SMARTS v. 2.9.2. Which provides use values for the wavelength, Extraterrestrial Radiation (ETR), Direct + Circumsolar and Global tilt. These values are downloaded through the NREL website (http://rredc.nrel.gov/solar/spectra/am1.5/astmg173/astmg173.html). Figure B. 1 shows that spectra of the solar radiation of ETR, Direct + Circumsolar and Global tilt as a function of wavelength.

Extraterrestrial Radiation is the solar spectrum at mean Earth-Sun distance (at top of atmosphere). Direct Normal Irradiance is nearly parallel (0.5 deg divergent cone) radiation on surface with surface normal tracking the sun, excluding scattered sky and reflected ground radiation. Circumsolar is the Spectral irradiance within +/- 2.5 degree (5 degree diameter) field of view centered on the 0.5 deg diameter solar disk, but excluding the radiation from the disk and Global Tilt is the spectral radiation from solar disk plus sky diffuse and diffuse reflected from ground on south facing surface tilted 37 deg from horizontal.
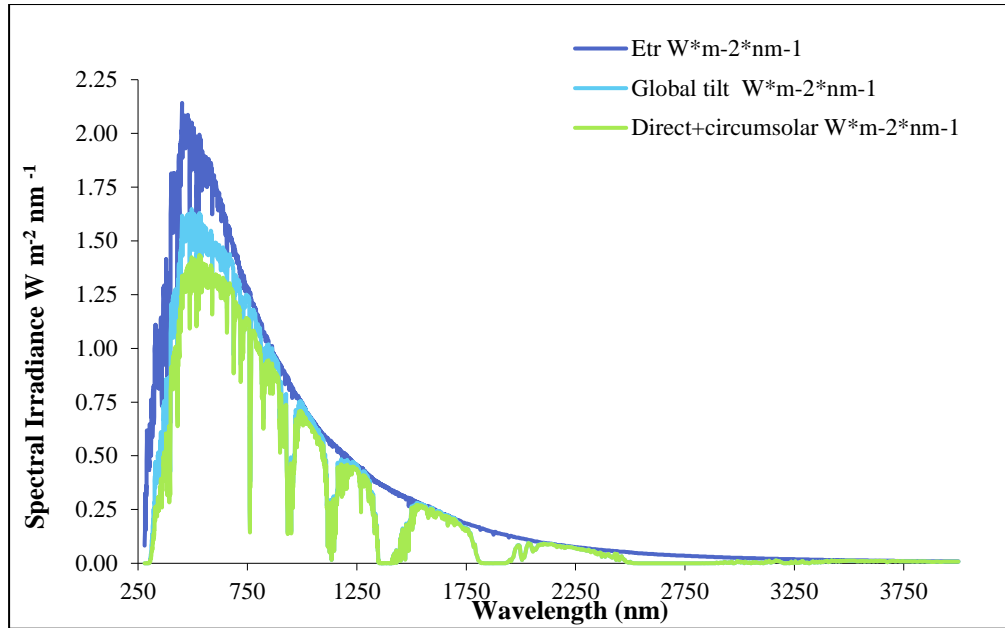
Figure B. 1: shows that spectra of the solar radiation of ETR, Direct + Circumsolar and Global tilt as a function of wavelength

Then for each wavelength the energy per photon (J) is calculated by Equation B.1

$$E = \frac{hc}{\lambda} = \frac{6.626070040 \times 10^{-34} Js \times 299792458 \; m/s}{(nm \times 0.000000001)m}$$

Equation B.1

where E is the energy per photon in J, h is the plank constant, which is

$6.626070040 \times 10^{-34}$ Js, c is the speed of light, which is also a constant (299792458

m/s) and λ is the wavelength in m.

Then we calculated the photons per m^2 per nm by Equation B.2

$$Photons \; per \; second \; per \; m^2 \; per \; nm = \frac{Global \; tilt \; (Wm^{-2}nm^{-1})}{Energy \; per \; photon \; (J)}$$

Equation B.2

Then the total photons per increment per m^2 was calculated by Equation B.3

134

$$Total\ photons\ per\ increment\ per\ m^2\ per\ s$$

$$= Photons\ per\ s\ per\ m^2\ per\ nm\ \times\ increment$$

As we need the transmittance (T), we will need to convert our absorption (A) data to transmittance (T). Therefore, we know that Absorption and Transmittance is related by Equation B.4

$$A = -logT$$

Therefore, the transmittance and be calculated by Equation B.5

$$T = 10^{-A}$$

Therefore, to calculate the % of light that is absorbed by the material (A') by Equation B.6

$$A' = 1 - T$$

Now we need to calculate the total electrons generated per m^2 per s, this is done by Equation B.7

$$Total\ electron\ generated\ per\ m^2\ per\ s$$

$$= total\ photons\ per\ increment\ per\ m^2\ per\ s\ \times\ IPCE\ \times\ A'$$

where the IPCE is the Incident photon to current efficiency, this is assumed to be one as it is assumed that all the photons absorbed are converted into current. A' is the % of that is absorbed by the material, which was calculated by Equation B.6 and total photons per increment per m^2 was calculated by Equation B.3.

Therefore, the current per m² (Amp/m²) can be calculated by Equation B.8. Where the total electrons generated per m² per s is calculated by Equation B.7 and the charge of an electron is a constant, which is 1.60218×10^{-19}C.

$$Current\ per\ m^2\ (Amp/m^2)$$

$$= Total\ electron\ generated\ per\ m^2\ per\ s$$

$$\times\ charge\ of\ an\ electron\ (C)$$

Equation B.8

So, the total current is the sum of all the current generated at each wavelength (Equation B.9)

$$Total\ current\ (Amp/m^2) = \sum current\ per\ m^2(Amp/m^2)$$

Equation B.9

Appendix C: Annealing Absorbance Study

Below is the absorbance spectra of DHSQ(OH)$_2$:PCBM at various blend ratio. For this study, the total solute concentration was kept constant to 16 mg/mL.
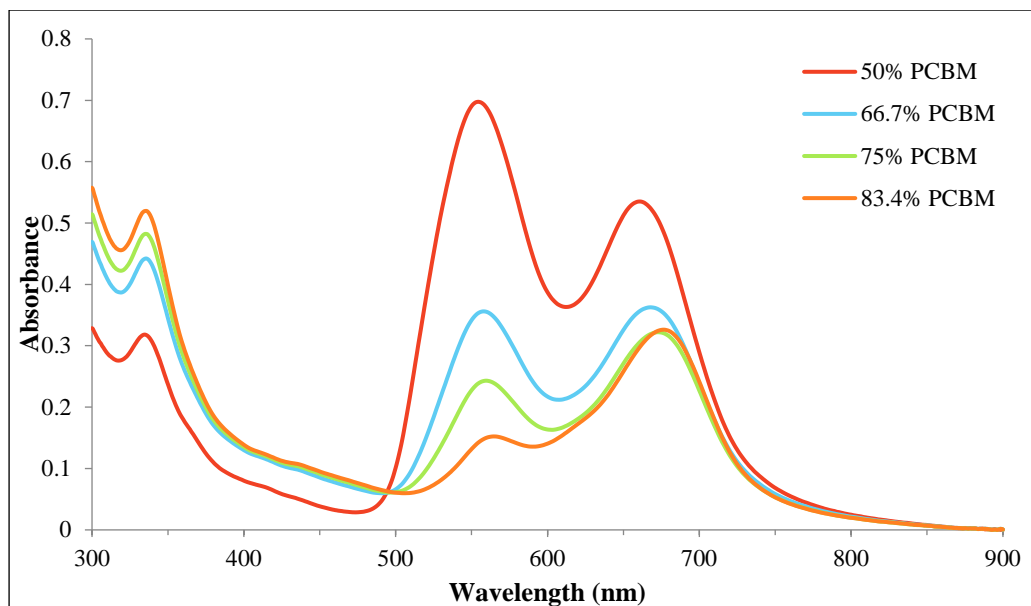

Figure C. 1: Absorbance spectra from spin-coated films of blends of DHSQ(OH)$_2$:PC$_{61}$BM in various mixing ratios as noted on the graph

Thermal Annealing

All films were thermally annealed at 110 °C for various times to see how the absorbance spectra changed.
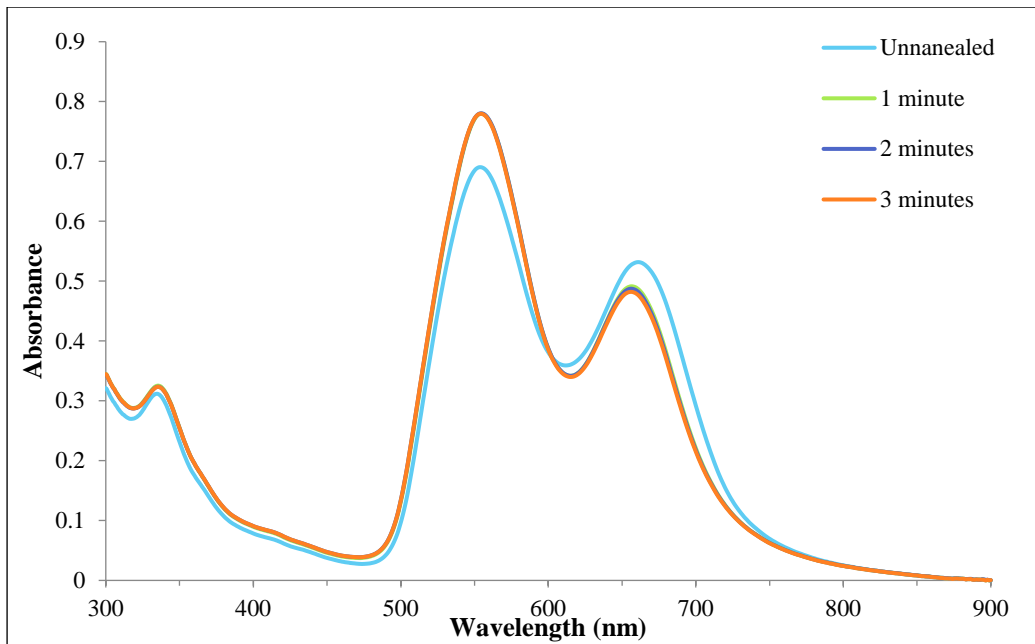
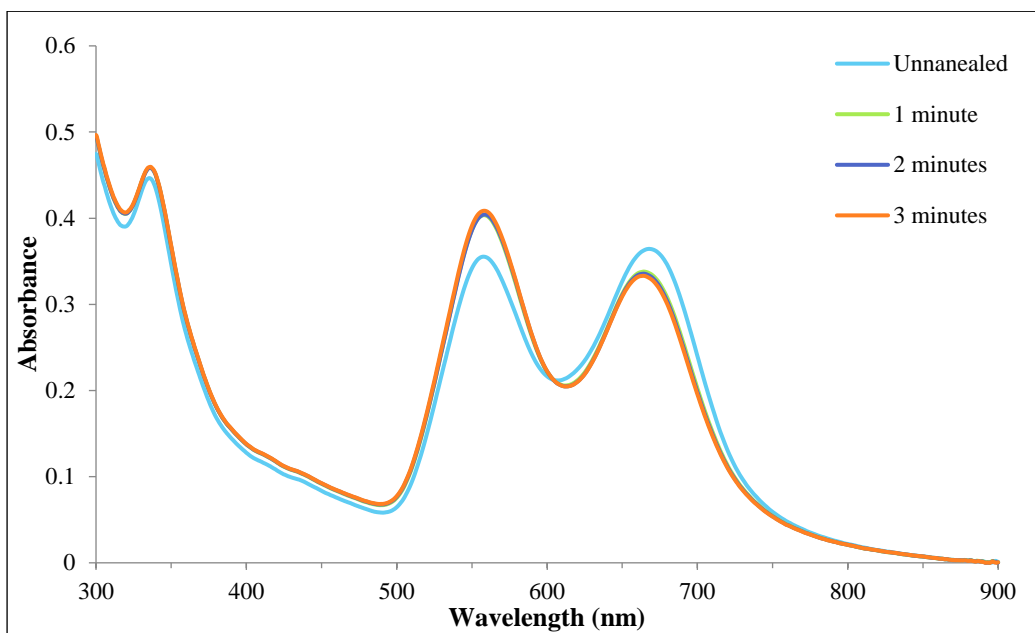**Figure C. 2: Absorption spectra of 50% DHSQ(OH)₂: 50% PCBM thermal annealed at 110 °C with a range of annealing times**

Figure C. 3: Absorption spectra of 33.33% DHSQ(OH)₂: 66.67% PCBM thermal annealed at 110 °C with a range of annealing times
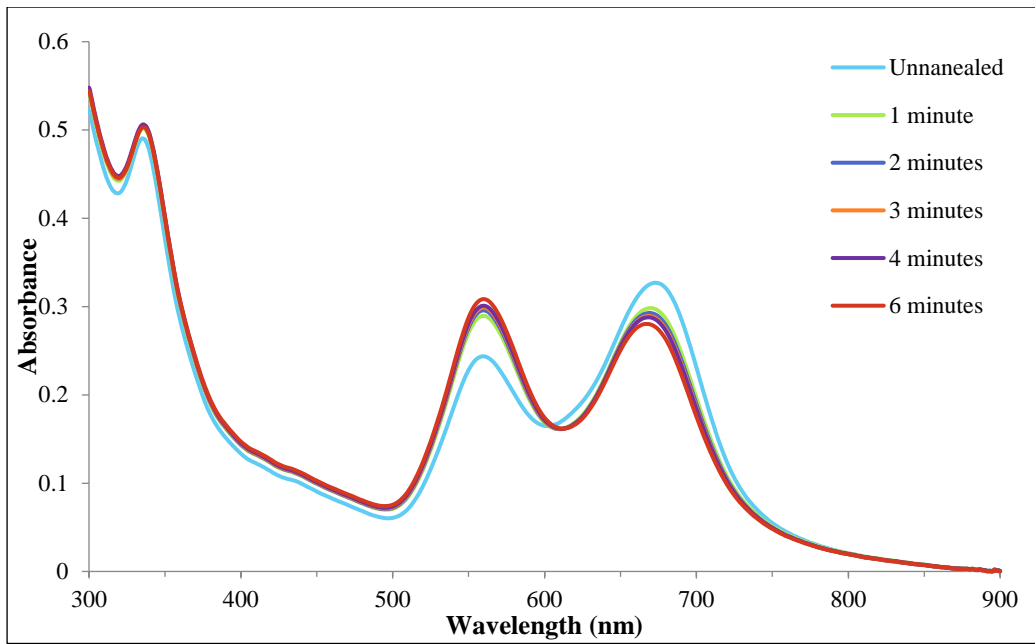
Figure C. 4: Absorption spectra of 25% DHSQ(OH)$_2$: 75% PCBM thermal annealed at 110 °C with a range of annealing times
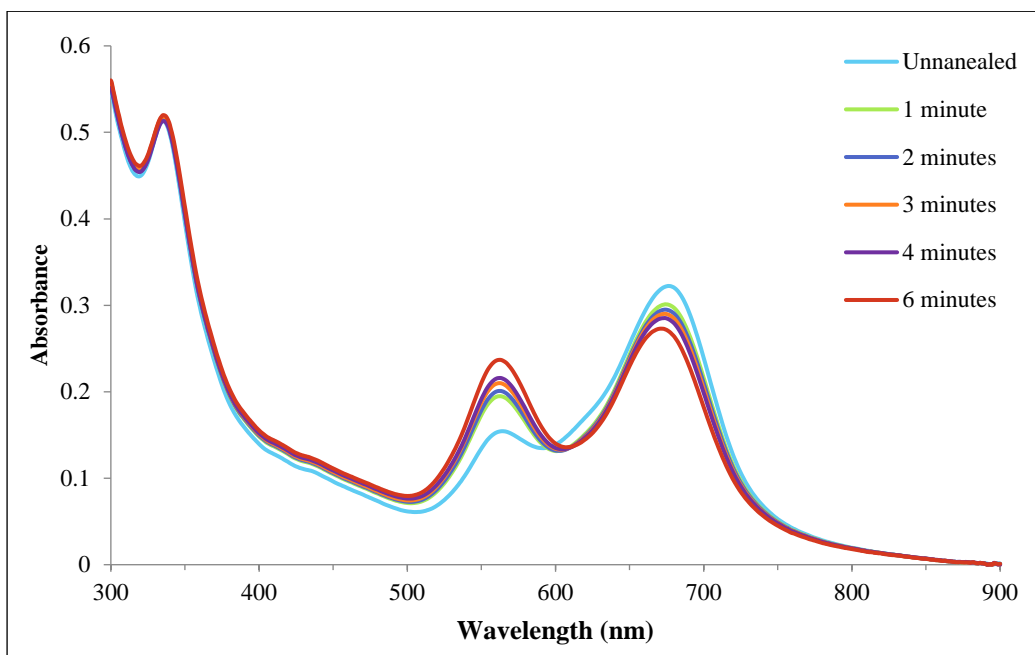

Figure C. 5 : Absorption spectra of 16.67% DHSQ(OH)$_2$: 83.33% PCBM thermal annealed at 110 °C with a range of annealing times

Table C. 1: Summary of the Thermal Annealing Absorption data

% PCBM	Annealing Time (minutes)	Monomer	Aggregate	A/M
50%	0	0.5318	0.6904	1.2983
	1	0.4914	0.7796	1.5867
	2	0.4873	0.7804	1.6014
	3	0.4821	0.7797	1.6173
66.67%	0	0.3644	0.3554	0.9752
	1	0.3380	0.4035	1.1937
	2	0.3356	0.4042	1.2045
	3	0.3331	0.4086	1.2267
75%	0	0.3270	0.2437	0.7454
	1	0.2983	0.2894	0.9704
	2	0.2928	0.2957	1.0100
	3	0.2894	0.2990	1.0333
	4	0.2878	0.3009	1.0455
	6	0.2803	0.3085	1.1005
83.33%	0	0.3224	0.1544	0.4790
	1	0.3012	0.1949	0.6470
	2	0.2950	0.2010	0.6812
	3	0.2901	0.2100	0.7238
	4	0.2853	0.2160	0.7571
	6	0.2730	0.2369	0.8679

Solvent Vapor Annealing

All films were thermally annealed in DCM for various times to see how the absorbance spectra changed
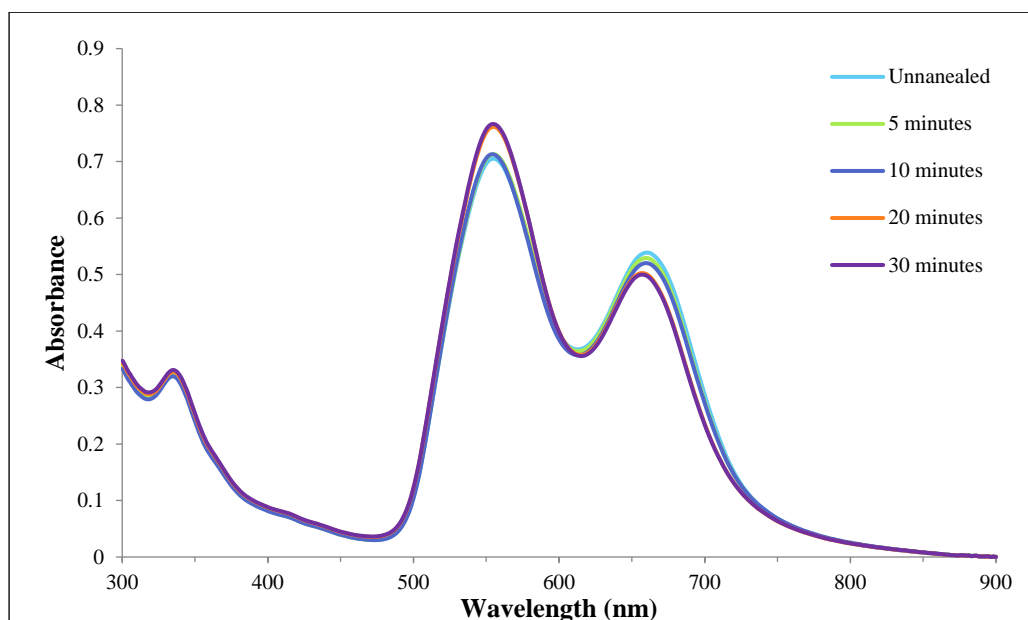

Figure C. 6: Absorption spectra of 50% DHSQ(OH)$_2$: 50% PCBM Solvent annealed in DCM with a range of annealing times
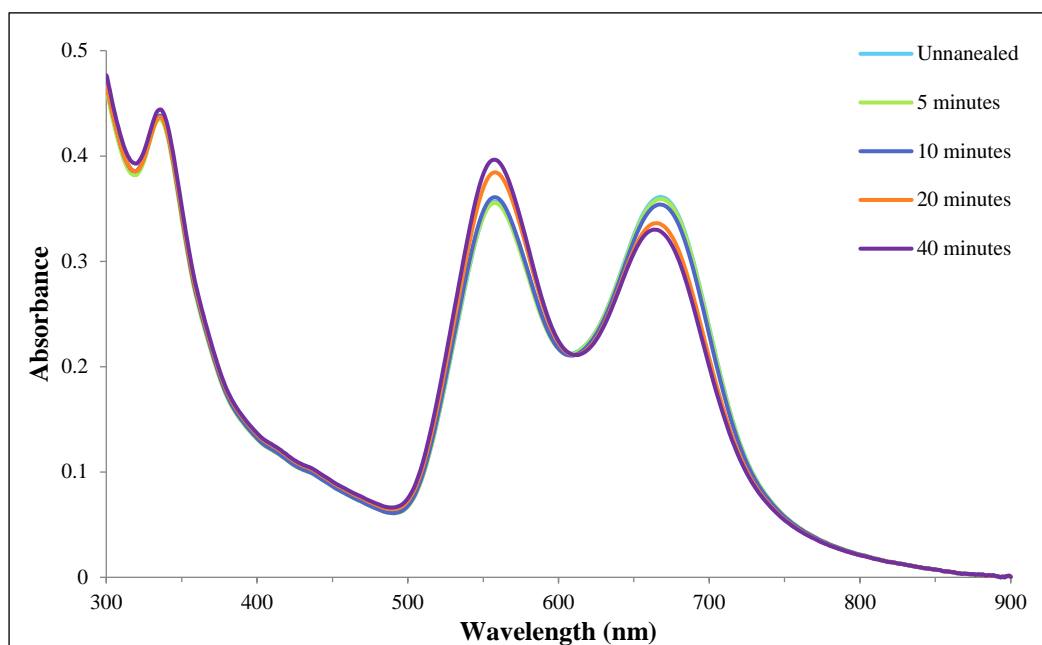

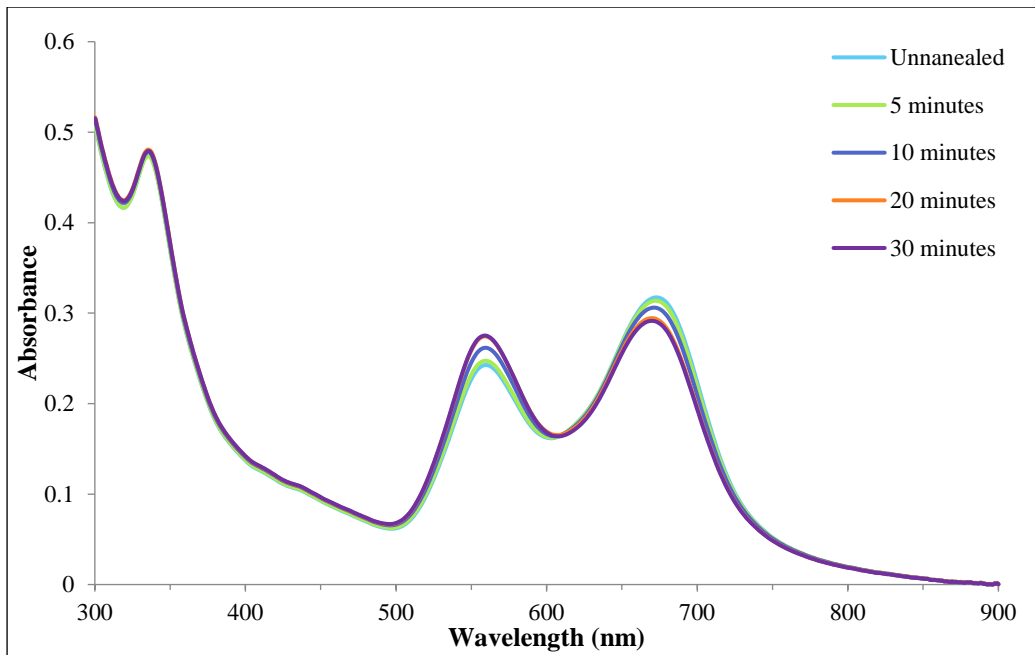**Figure C. 7: Absorption spectra of 33.33% DHSQ(OH)$_2$: 66.67% PCBM Solvent annealed in DCM with a range of annealing times**

Figure C. 8: Absorption spectra of 25% DHSQ(OH)$_2$: 75% PCBM Solvent annealed in DCM with a range of annealing times
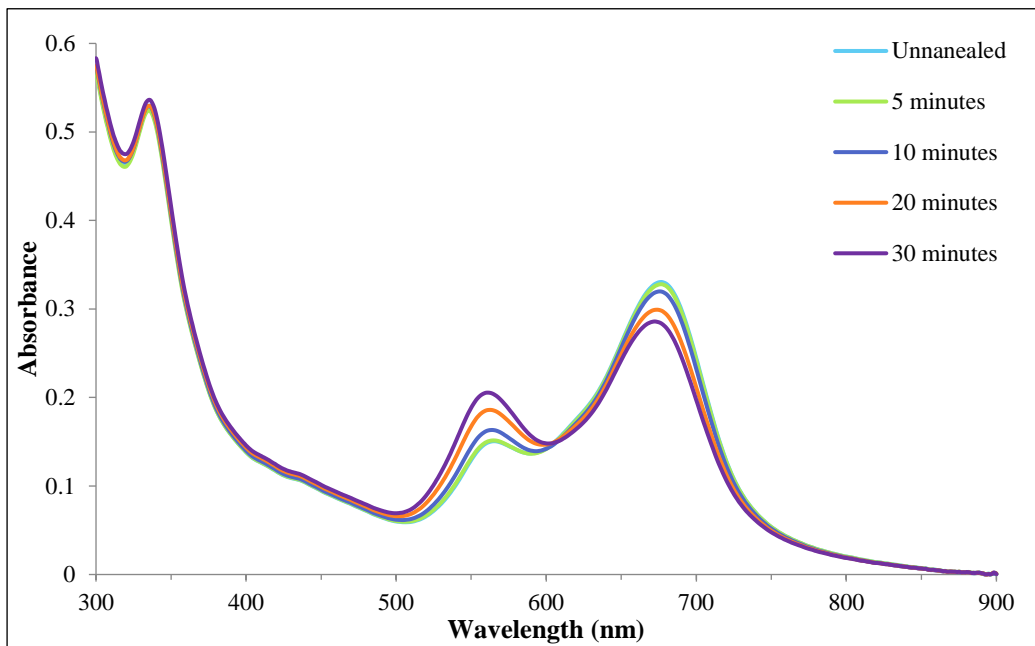

Figure C. 9: Absorption spectra of 16.67% DHSQ(OH)$_2$: 83.33% PCBM Solvent annealed in DCM with a range of annealing times

Table C. 2: Summary of the Solvent Vapor Annealing Absorption data

% PCBM	Annealing Time (minutes)	Monomer	Aggregate	A/M
50%	0	0.5388	0.7051	1.3087
	5	0.5293	0.7131	1.3473
	10	0.5203	0.7129	1.3702
	20	0.5027	0.7615	1.5150
	30	0.4999	0.7665	1.5333
66.70%	0	0.3611	0.3568	0.9883
	5	0.3591	0.3554	0.9896
	10	0.3540	0.3609	1.0194
	20	0.3362	0.3844	1.1435
	40	0.3301	0.3964	1.2010
75%	0	0.3174	0.2427	0.7644
	5	0.3137	0.2473	0.7885
	10	0.3061	0.2617	0.8550
	20	0.2945	0.2743	0.9315
	30	0.2915	0.2752	0.9443
83.40%	0	0.3305	0.1506	0.4557
	5	0.3280	0.1515	0.4620
	10	0.3198	0.1633	0.5106
	20	0.2992	0.1860	0.6217
	30	0.2859	0.2055	0.7188